



Construction of a near-source broadband earthquake ground motion dataset from 3D physics-based numerical simulations

Work Package#3 “Ground motion”



AUTHORS		REVIEW		APPROVAL	
Name	Date	Name	Date	Name	Date
<i>Paolucci R., Smerzini C., Vanini M.</i> 	2020/05/15	<i>John Douglas Hiroshi Kawase</i>	2020/07/06	Philippe Renault  Public-access <input checked="" type="radio"/> SIGMA-2 restricted <input type="radio"/>	2020/02/23

Document history

DATE	VERSION	COMMENTS
2020/05/15	0	
2020/07/06	1	<i>Revised after reviewers' remarks</i>

Table of Contents

Document history.....	2
1. Introduction and Scope	4
2. Overview of SPEED and broadband processing	10
2.1 Workflow for optimized post-processing of SPEED results	10
2.2 ANN2BB approach for the generation of broadband ground motions	20
3. Overview of processed numerical simulations	24
4. Organization of a flatfile for the BB-SPEEDset_V0.....	29
5. Towards a near-source ground motion model from PBS.....	33
5.1 Effect of different source-to-site distance metrics	33
5.2 A preliminary near-source ground motion model	40
5.3 Directionality: FN/FP	44
5.4 Vertical-to-Horizontal Ratios.....	47
5.5 Pulse periods	50
6. Conclusions and future developments	55
References	59
Appendix A	63
Appendix B	73
Appendix C	75

1. Introduction and Scope

This report provides an overview of the research activities carried out at Politecnico di Milano during the second and third year of the 2017-2022 project “Development of advanced physics-based numerical approaches for earthquake ground motion prediction”, under the cooperation between Politecnico di Milano and swissnuclear¹, within the SIGMA2 research program.

More specifically, this report refers to the Task C of the research, about the characterization of near-source earthquake ground motion from the results of physics-based numerical simulations (see technical overview of the first phase of the project in Figure 1.1).

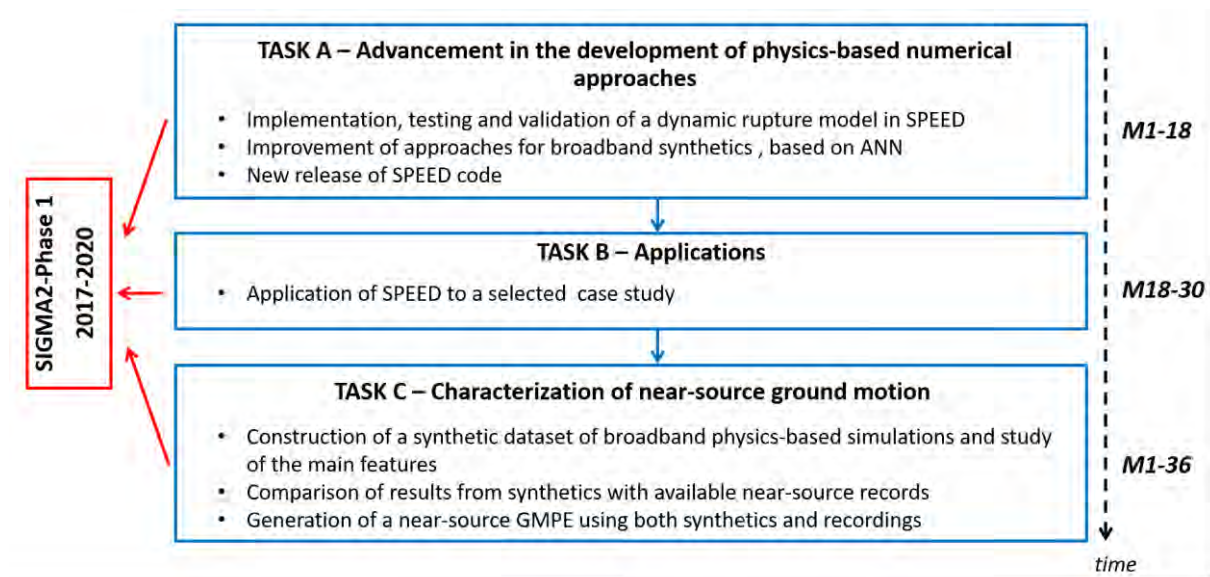


Figure 1.1 Project technical overview: main tasks and corresponding time schedule

This research is in continuity with the work carried out at the Istituto Nazionale di Geofisica e Vulcanologia (INGV), Milano, who recently constructed the NESS dataset (<http://ness.mi.ingv.it/>, Pacor et al., 2018), a worldwide collection of strong motion records in near-source conditions.

As a matter of fact, in spite of the careful search, selection and compilation of metadata, that probably makes NESS the richest near-source dataset publicly available, Figure 1.2(a) clearly illustrates the paucity of records for very small values of the Joyner-Boore (R_{JB}) distance. The concept itself of near-source is subject to a degree of arbitrary judgement. Based on seismological scaling relationships, in the NESS the near-source threshold distance (R_{ns}) is defined as:

$$\log_{10}(R_{ns}) = \log_{10} k + \frac{1}{2} M_w - \frac{1}{3} \log_{10} \Delta\sigma + 3.134 \quad (1.1)$$

where R_{ns} is given in m and $\Delta\sigma$ is the static stress drop in Pa, while k is the parameter used to quantify how many fault lengths the sites should be away from the fault, to be considered within the near-source region. The scaling of R_{ns} as a function of M_w and stress drop according to Eq. (1.1) is shown in Figure 1.2(a) for $k=1$, that is within one fault length. In Figure 1.2(b) the corresponding R_{ns} values, for the case of $\Delta\sigma = 10$ bars (that is the average stress drop for moderate and strong earthquakes) are shown²,

¹ Contract n. FGK-V-17.059 – SIGMA 2 between swissnuclear and Politecnico di Milano

² In Pacor et al. (2018), the near-source criterion $R_{JB} < R_{ns}$ is selected. One may argue whether considering different distance metrics to be compared to R_{ns} may change significantly the classification of near source records. For example, according to Scherbaum et al. (2004), the average difference $R_{rup} - R_{JB}$ for $M=7$ when $R_{JB}=43$ km is only 1.5 km. R. Paolucci et al. - Construction of a near-source broadband earthquake ground motion dataset from 3D physics-based numerical simulations - SIGMA2-2020-D3-051

together with the average subsurface fault length (RLD) according to Wells and Coppersmith (1994) for general faulting style and the fault rupture length according (L) to Leonard (2010) for dip-slip earthquakes.

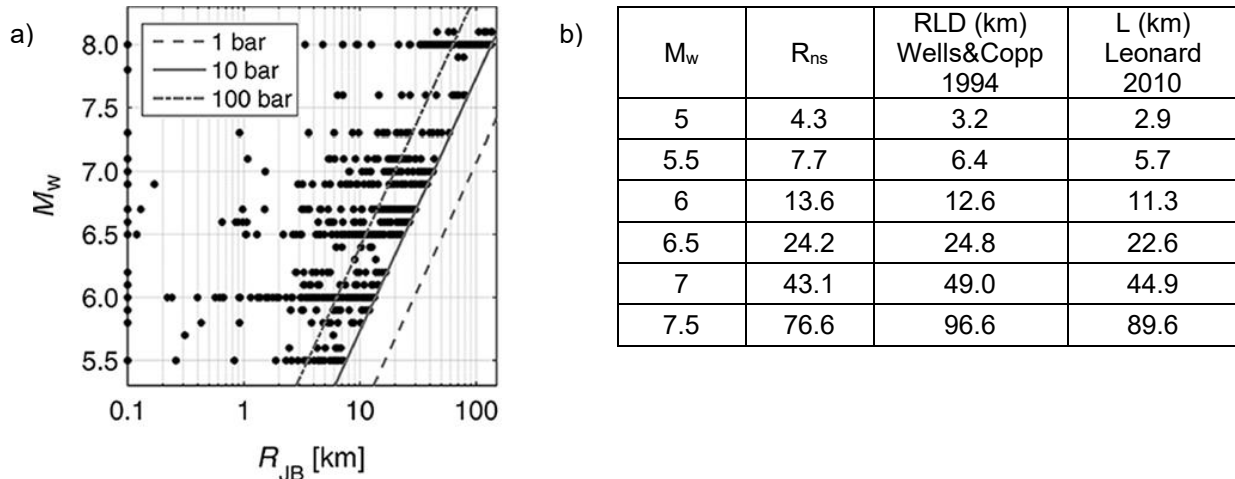


Figure 1.2 (a) Data distribution of NESS Database in terms of magnitude M_w versus Joyner–Boore distance, R_{JB} ; lines represent the scaling of the near-source distance, R_{ns} , as a function of M_w and stress drop according to Eq. (1.1), for $k = 1$. (b) R_{ns} values as a function M_w (for $\Delta\sigma = 10$ bar and $k=1$) together with the average subsurface fault length (RLD) according to Wells and Coppersmith (1994) and the fault rupture length (for dip-slip earthquakes) according to Leonard (2010).

The aim of this research is to provide a complementary approach to characterize earthquake ground motion in near-source conditions, by constructing a broadband ground motion dataset from realistic scenarios obtained by 3D physics-based numerical simulations (PBS). In the ideal situation in which PBS were a numerical laboratory suitable to provide realistic region- and site-specific realizations of future earthquake broadband ground motions in a limited computer time, the advantage of such a numerical approach would be evident. As a matter of fact, it would be possible to investigate systematically those features of near-source ground motion, such as dependence on the fault radiation pattern, directivity, impulsive characteristics, vertical components, interaction with surface geology, spatial correlation, etc, that are hard to be explored from records because of their limited number.

However, the construction of such an ideal laboratory platform is still in progress, the main difficulty being that numerical codes for PBS have limited capacity to provide accurate results in a broad frequency range in a reasonably short amount of computer time and that validation case studies against sets of records from real earthquakes were carried out only in relatively few cases with little attention to near-source conditions.

In this framework, the activity of the research group of Politecnico di Milano within the SIGMA2 project were initially directed towards improving the performance of SPEED (<http://speed.mox.polimi.it>, Mazzieri al. 2013), the spectral element code for PBS developed at Politecnico and already used in several case

about 2 km. Therefore using as near source criterion either $R_{JB} < R_{ns}$ or $R_{RUP} < R_{ns}$ is almost indifferent. However, for small magnitude earthquakes, the distance metrics to define the near-source condition becomes more critical. For example, according to Scherbaum et al. (2004), the average value for $R_{rup}-R_{JB}$ is about 4.5 km when $M=5.5$ and $R_{JB}=7.7$ km. Therefore, some of the near-source records classified according to the criterion $R_{JB} < R_{ns}$ may not be classified as near-source according to the criterion $R_{rup} < R_{ns}$.

studies both for verification within international benchmarks, for validation with recorded near-source ground motion or for generation of future earthquake ground motion scenarios. The list of SPEED applications is provided in Table 1.1.

Table 1.1 List of PBSs computed by SPEED between 2010-2020 in different phases of developments of the code. PBS included in the first version of the database are highlighted in orange.

Case Study	Mw	Model size (km ³)	$V_{s,min}$ (m/s)	f_{max} (Hz)	Validation (Y/N)	References
Grenoble, France	6.0	41x50x8	300	3	Benchmark Exp.	Stupazzini et al. (2009)
Gubbio Plain, Umbria, Central Italy	6.0	85x62x10	250	3	Y: 26 Sept 1997	Smerzini et al. (2011)
Tagliamento plain, Friuli, Northern Italy	6.1	57x53x12	300	2.5	Y: 15 Sept 1976	Smerzini et al. (2010)
L'Aquila, Central Italy	6.2	58x58x20	300	2.0	Y: 6 Apr 2009	Evangelista et al. (2017)
Sulmona, Central Italy	6.4	49x42x13	500	2.5	N	Villani et al. (2014)
Christchurch, New Zealand	6.3	60x60x20	300	2.0	Y: 22 Feb 2011	Guidotti et al. (2011)-revised
Po Plain, Northern Italy	6.0	74x51x20	300	1.5	Y: 29 May 2012	Paolucci et al. (2015)
Fucino Plain, Marsica, Central Italy	6.7	56x46x20	100	2.0	Y: 13 Jan 1915	Paolucci et al. (2016)
Thessaloniki, Northern Greece	6.5	82x64x31	300	1.5	Y: 20 Jun 1978	Smerzini et al. (2017)
Norcia, Central Italy	5.5-6.5	50x40x21	280	1.5	Y: 30 Oct 2016	Ozcebe et al. (2019)
Wellington, New Zealand	6.0-7.0	80x50x45	300	2.0	N: future scenarios	Paolucci et al. (2014)
Santiago, Chile	6.0-6.7	97x77x19	400	2.0	Y: 1 Apr 2010	Pilzt et al. (2011)
Istanbul, Turkey	7.0-7.4	165x100x30	250	1.5	Y:26 Sept 2019	Infantino et al. (2020) Stupazzini et al. (2020)
Beijing, China	6.5-7.3	70x70x30	200	1.5	N: future scenarios	Antonietti et al. (2020)
Groningen, the Netherlands	3.4	20x20x5	150	10	Y: 08 Jan 2018	Paolucci et al. (2020)

Particularly, an innovative post-processing procedure was developed and tested during the first year of the Project. The procedure, based on Artificial Neural Networks trained on strong ground motion recordings, is devised in order to predict short period response spectral ordinates based on the long period ones, resulting from PBS. The approach was found to produce not only realistic broadband synthetics but also a proper spatial correlation structure, as verified by comparison with the dense temporary network that recorded in near-source the May 29 2012, M_w 6.0 Po Plain, Northern Italy earthquake (Paolucci et al., 2018).

In parallel, SPEED was equipped with tools for automatic generation of realistic kinematic fault slip distributions consistent with results from dynamic fault rupture modelling (Herrero and Bernard, 1994; Schmedes et al., 2012), allowing the production of earthquake ground motion scenarios from the same fault with the proper event-to-event variability, as verified for the Istanbul ground motion scenarios (Infantino et al., 2020; Stupazzini et al., 2020).

The stage of development of SPEED, as well as of the performance of its pre- and post-processing tools, were also tested within the second year of the SIGMA2 Project considering as a validation case study the 2016 M_w 6.5 Central Italy (Norcia) earthquake case.

Making reference to the SIGMA2 2nd year progress report³ for a comprehensive introduction to the PBS of the Norcia earthquake and of its validations, we limit ourselves here to showing in Figure 1.3 a comparison between (i) acceleration and displacement response spectra of a set of recordings from the NESS dataset (details in Table 1.2), (ii) of the PBS results obtained by SPEED at the corresponding stations, and (iii) the estimates from Ground Motion Prediction Equations (GMPE), of Lanzano et al. (2019) and Cauzzi et al. (2015), referred to as ITA18 and CZ15 respectively. Records have been selected according to comparable distances (i.e. R_{JB} between 0 and 3 km and R_{rup} between 0 and 10 km) and ground type conditions (rock).

There is an overall agreement between spectral values predicted according to the SPEED time histories and the considered GMPEs. At short periods, SPEED and GMPEs are in good agreement, while both tend to underestimate the recorded values. Note that at short periods, as will be explained in a later section, SPEED results are not the direct outcome of the simulation, but they are obtained through an Artificial Neural Network trained on a strong-motion dataset. Instead, at longer periods, while the GMPEs tend to underestimate the observations, SPEED results have the opposite tendency.

What is to be remarked as a lesson from the Norcia validation, as well as from the other ones listed in Table 1.1, is that SPEED, equipped with the related pre- and post-processing tools, is capable of producing realistic broadband ground motions with a realistic spatial variability.

In this concern, it must be pointed out that a “measure” of the predictive capability of a PBS scenario in a wider sense is essential, in order for it to be “confused” with one of the infinite possible realizations of a future earthquake along a given fault. This in principle requires a variety of steps, that can be summarized as follows:

- ✓ proof that PBSs results approach records from past earthquakes, where available;
- ✓ proof that PBSs provide realistic spatial variability features, in terms of both spatial correlation and coherency;
- ✓ proof that PBSs provide similar results as GMPEs, if in the same domain where GMPEs are well constrained;
- ✓ proof that PBSs provide realistic components of ground motion variability;
- ✓ proof that local site response is properly reproduced by PBSs.

Examples of such proofs for selected case studies among the ones listed in Table 1.1 is given in the Appendix A of this report.

Therefore, we considered that its stage of development is mature enough to take advantage of the earthquake ground motion scenarios produced so far and to construct a dataset of synthetic broad-band waveforms to be used as a support for characterization and modelling of near-source earthquake ground motions, that is the main objective of this report.

For this purpose, the research activity documented in this report is organized in the following tasks:

- ✓ to implement an effective workflow, suitable to process (or re-process) in a homogeneous way the simulations results obtained during the years in different phases of developments of SPEED and of the related processing tools;
- ✓ to prepare for each simulated scenario “ID cards” containing all relevant information regarding input data (fault parameters, geological data, soil models) and representative outputs (broadband ground shaking maps);

³ Paolucci R., Smerzini C., Mazzieri I., Özcebe A.G., Infantino M. Development of advanced physics-based numerical approaches for earthquake ground motion prediction. 2nd year Progress Report of the POLIMI – swissnuclear contract, within Project Sigma-2.

- ✓ to transfer such information into flatfiles containing the relevant site response proxies ($V_{s,30}$, H_{800} , etc) for each selected receiver;
- ✓ to complete such flatfiles with the relevant parameters of processed simulated broadband ground motions (Peak Ground Acceleration and Velocity, spectral ordinates, duration, pulse period, etc);
- ✓ to analyze the preliminary results from the complete processing of 5 scenarios (see selection in Table 1.1) to provide hints in view of the formulation of a near-source ground motion model based on PBS.

The Deliverable is organized as follows. In Section 2 the optimized workflow to process SPEED results and generate broadband ground motion time histories at an arbitrary set of receiver points is illustrated. Section 3 provides an overview of the processed 5 scenarios included in the first version of the synthetic broadband ground motion database, referred to as BB-SPEEDset (Version 0). Then, in Section 4 the general structure of the BB-SPEEDset_V0 flatfiles is described in detail. Finally, Section 5 focuses on preliminary analyses regarding: (i) the choice of optimum distance metrics in near-source conditions; (ii) the attenuation of near-source ground motions with distance; (iii) ground motion directionality and vertical-to-horizontal spectral ratios; and (iv) features of pulse-like ground motions.

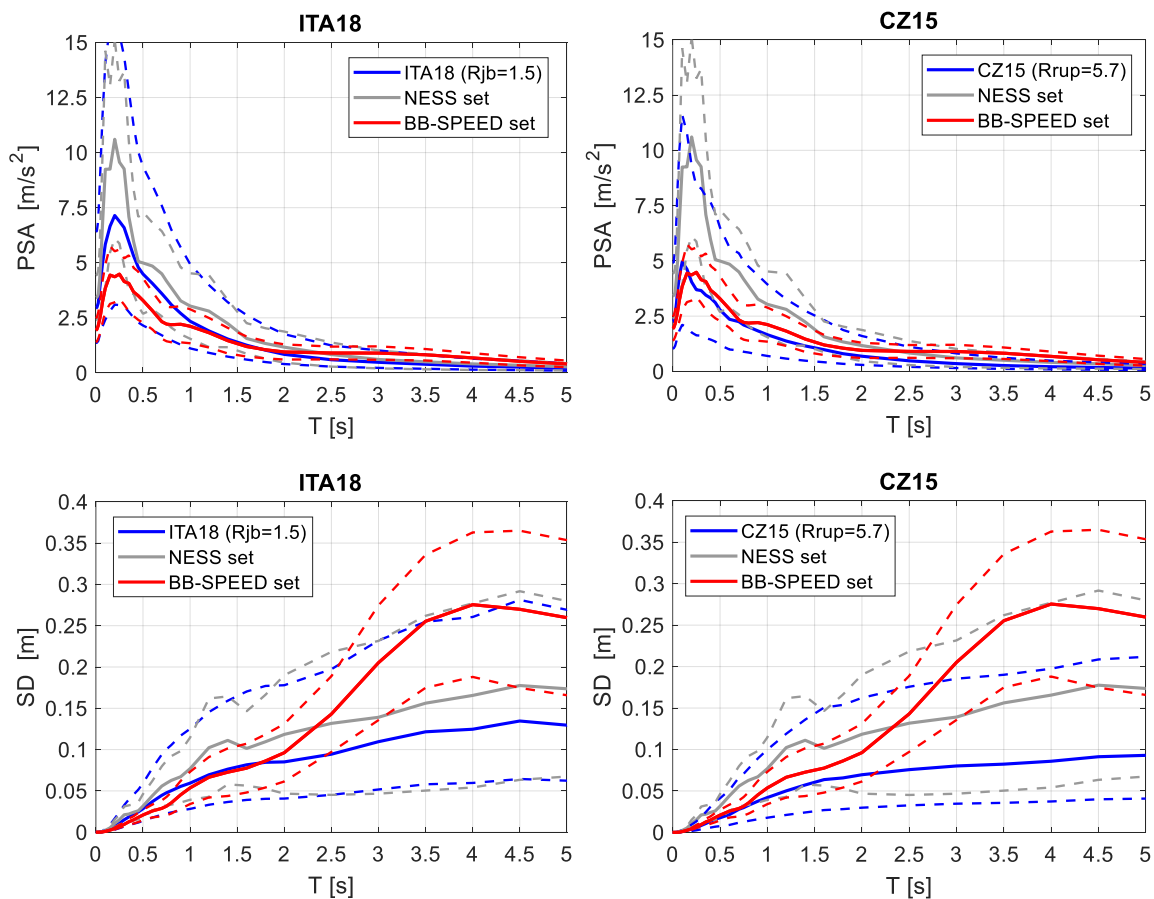


Figure 1.3 Acceleration and displacement response spectra from recordings (NESS dataset), synthetics (BB-SPEEDset) and GMPE predictions, with reference to comparable distances and ground type conditions, for the 2016 M_w 6.5 Central Italy (Norcia) earthquake.

Table 1.2 Records from NESS dataset used in Figure 1.3 for validation purposes. Station code, ground types and distances, according to different metrics, are shown.

Station Code	EC8 Code	R_{epi} (km)	R_{JB} (km)	R_{RUP} (km)
MZ102	-	17.4	1.1	5.62

ACC	A*	18.6	2.2	5.73
PRE	B*	8.2	2.6	8.95
T1214	B*	11.4	0.0	4.54
T1216	B*	9.9	3.1	9.25
T1244	B*	17.4	0.0	0.0

2. Overview of SPEED and broadband processing

A fundamental step for the construction of a synthetic database of PBS is the definition of a workflow for the optimized post-processing of results of SPEED simulations in a standard and repeatable format (see Section 2.1). As a preparatory step to this workflow, it was necessary to collect and store in a homogeneous format the PBS developed in different phases of the code development, according to a common format of input data.

The core of the post-processing workflow is the generation of broadband ground motions starting from low-frequency results of PBS in a semi-automated fashion. To this end, an innovative procedure (ANN2BB), based on Artificial Neural Networks trained on strong ground motion recordings, is devised in order to predict short period response spectral ordinates based on the long period ones, resulting from PBS (Paolucci et al., 2018). In the context of an optimized workflow for broadband processing, further refinements were made to the procedure to improve the quality of generated waveforms and streamline the batch post-processing of larger ground motion sets, as reported in Section 2.2.

2.1 Workflow for optimized post-processing of SPEED results

The main SPEED code is supplemented by a set of Matlab routine packages that allow post-processing the raw SPEED results (typically, displacement time histories at receiver points) and generate outputs in a standard format. Note that the same package is equipped with routines specifically developed for pre-processing, i.e. to generate realistic kinematic rupture scenarios, consistently with results from dynamic fault rupture modelling (Herrero and Bernard, 1994; Schmedes et al., 2012), and produce the corresponding input files for SPEED simulations.

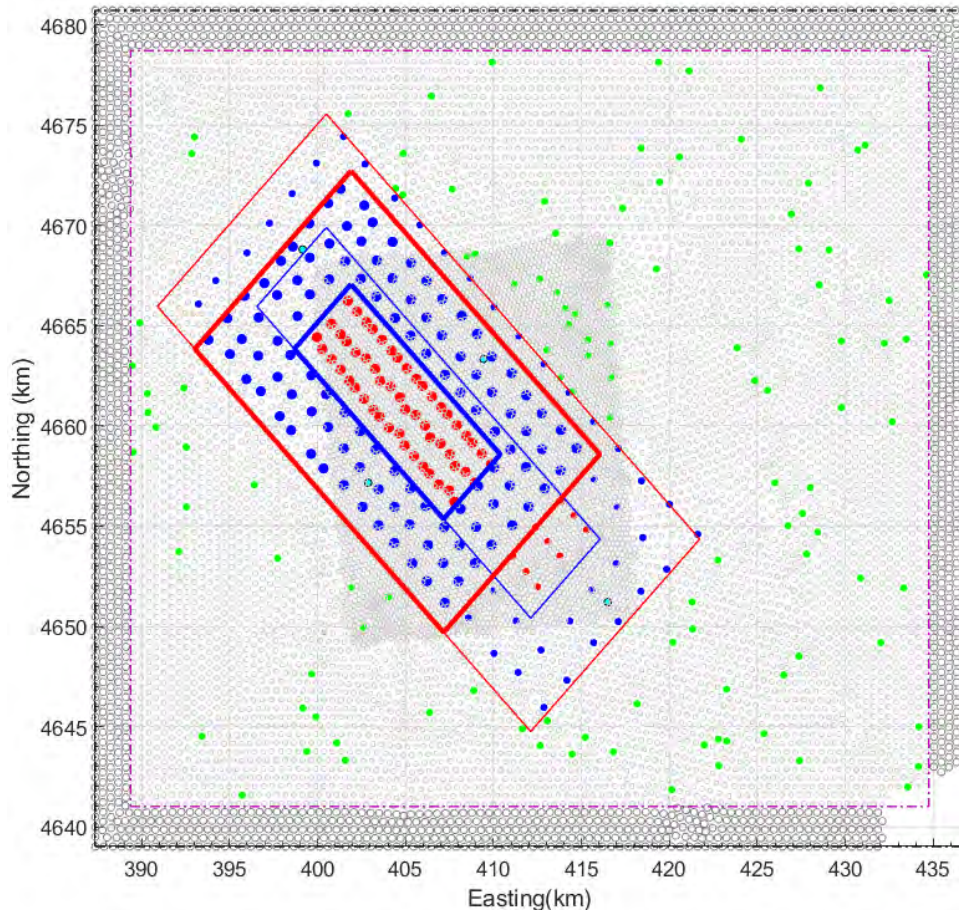
An overview of the post processing workflow is given in Figure 2.1 and it can be classified in three main groups.

(1) MAIN POST-PROCESSING STREAM.

The first class collects the codes needed for the first main post-processing consisting of:

- *3PTOOL* code extracts and organizes the original raw SPEED displacement seismograms in a Matlab (.mat) file to ease the subsequent analysis. The .mat file contains: receiver coordinates, raw displacement time histories, low frequency Peak Ground Maps (directly from SPEED), broadband Peak Ground Maps (from ANN2BB approach). See Figure 2.2.
- *SITE RESPONSE PROXIES* code computes for each numerical model the following site response proxies: H_{bedrock} - depth of the geological bedrock of the simulation model (i.e. alluvial-bedrock interface corresponding to the lowest resonance frequency), H_{800} - depth at which the shear-wave velocity V_s is equal or higher than 800 m/s, $V_{S;30}$ - time averaged shear-wave velocity from the surface to a depth of 30 meters, $V_{S;eq}$ - time averaged shear-wave velocity from the surface to H_{800} (if $H_{800} \leq 30$ m; if $H_{800} > 30$ m, then $H_{800}=30$ m), see definition in the Italian Building Code (NTC 2018), $V_{S;H_{\text{bedrock}}}$ - time averaged shear-wave velocity from the surface to H_{bedrock} , $V_{S;800}$ - time averaged shear-wave velocity from the surface to H_{800} ; topography slope. See Figure 2.3.
- *EFFECTIVE FAULT* code computes the effective dimensions of the rupture fault area according to the procedure originally proposed by Mai and Beroza (2000), and extended by Thingbaijam and Mai (2016). Effective source dimensions are based on the definition of autocorrelation width (Bracewell, 1986) of slip distributions, calculated in along-strike and down-dip directions. These slip functions are computed summing up the slip in columns (or rows) on the rectangular rupture plane. An iterative, trimming, process determines the largest dimensions that fit the autocorrelation width, according to the subfault size. See Figure 2.4.

- *SELECT RECEIVERS* code extracts subsets of receiver points according to prescribed sampling techniques. Since the simulated seismograms are generally obtained at tens of thousands of receivers, it is useful to define a smart strategy to select subsets of receiver points to be used for analysis that would require a very high computational effort and time (such as computation of RotD50 and RotD100 that require the rotation of time histories from 0° to 180°) if evaluated on the entire set of receivers. See



- Figure 2.5.
- *BROADBAND GENERATION* code. As previously mentioned, the SPEED outputs are limited in frequency depending on the resolution of the numerical model. A technique to enrich the signal at high frequencies has been devised and described in Section 2.2. It is worth noting that with 3PTOOL code the broadband peak values (i.e. spectral ordinates) are computed using the trained ANN, while, at this stage, broadband waveforms are computed. Since the high-frequency enrichment of the entire signal is computational demanding, it is generally limited to those receivers selected by the *SELECT RECEIVERS* procedure. See Figure 2.6.
- *SPEED IDCards* code generates a .pdf summarizing the main features of the numerical model and simulated results. See Figure 2.7
- *FLAT-FILE GENERATION* code. A flat-file is created in a format agreed with INGV (Istituto Nazionale di Geofisica e Vulcanologia) and consistent with the NESS database (Pacor et al, 2018, see Introduction of this report). The flatfile includes an exhaustive list of metadata (such as source metadata, site response proxies) and ground motion Intensity Measures for each chosen receiver (selected according to *SELECT RECEIVERS* procedure). See Figure 2.8.

Besides this “main stream” package of tools there is a “secondary” one including a couple of codes used for specific purposes.

(2) SECONDARY POST-PROCESSING STREAM

The secondary post-processing stream focuses on two main aspects particularly relevant for earthquake engineering applications: inelastic earthquake response and spatial correlation of ground motion intensity measures.

- *INELASTIC ENGINEERING DEMAND* code evaluates the time response of inelastic single-degree-of-freedom (SDOF) systems for given period and yield strength together with the inelastic response spectrum (e.g. constant ductility response spectrum) of a prescribed physics-based broadband accelerogram. See Figure **2.9**.
- *SPATIAL CORRELATION* code computes the semi-variograms and the spatial correlation parameters (i.e. range and sill) of each simulation (or a set of them). See Figure **2.10**.

(3) SUPPORTING POST-PROCESSING STREAM

Finally, as a supporting tool (not directly needed for the post-processing) there is the ANN TRAINING code, used for the development of the broadband tool to be applied to the low frequency SPEED results. This code trains Artificial Neural Networks (ANNs) on a strong ground motion database, such as the SIMBAD database (Smerzini et al. 2014) or the NGA-West2 (Ancheta et al. 2013). Generally, once an ANN is trained, it can be directly applied to whatever simulation, unless a new training is needed for specific reasons (e.g. because a wider strong motion database is needed or a different corner period has to be selected).

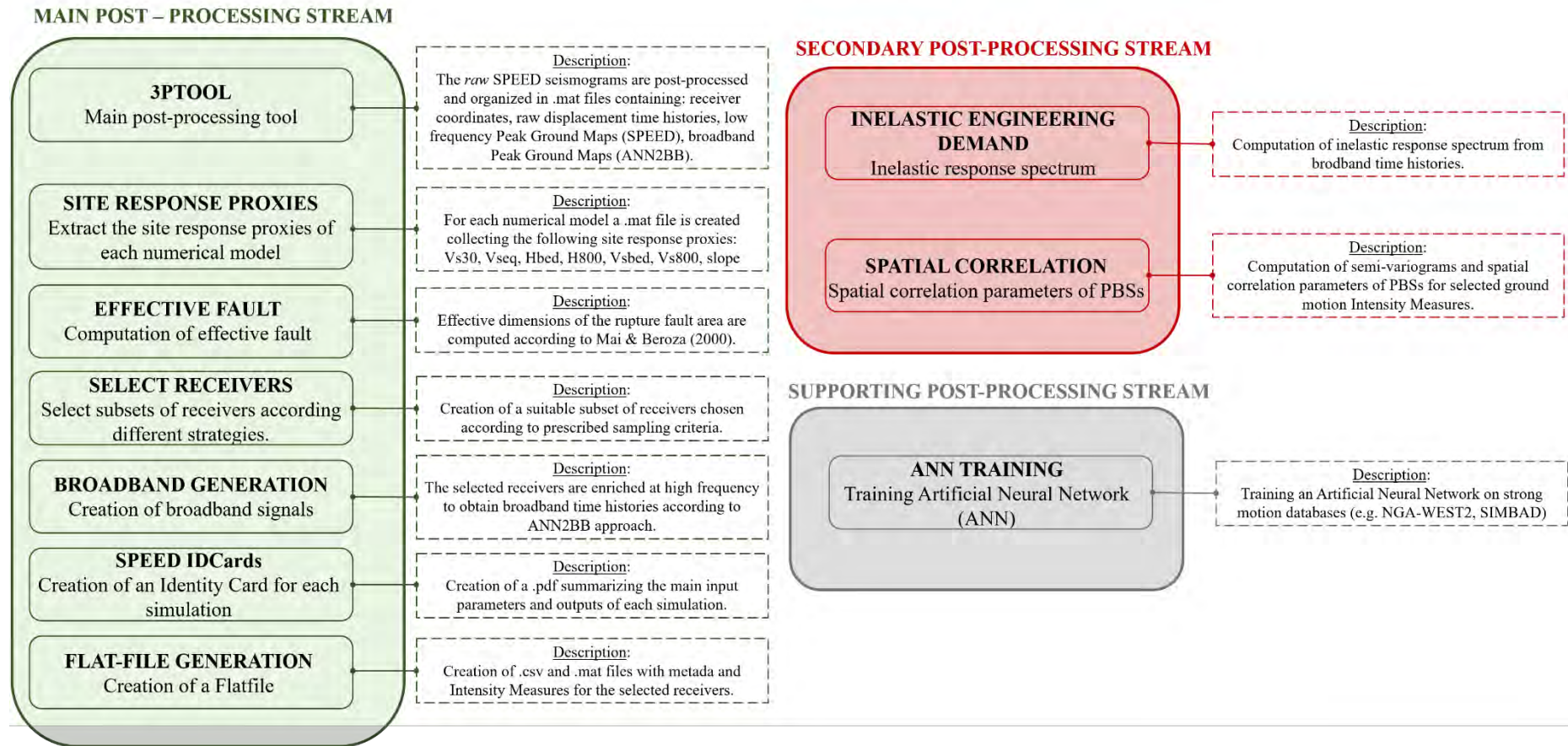


Figure 2.1 Workflow for post-processing of SPEED results.

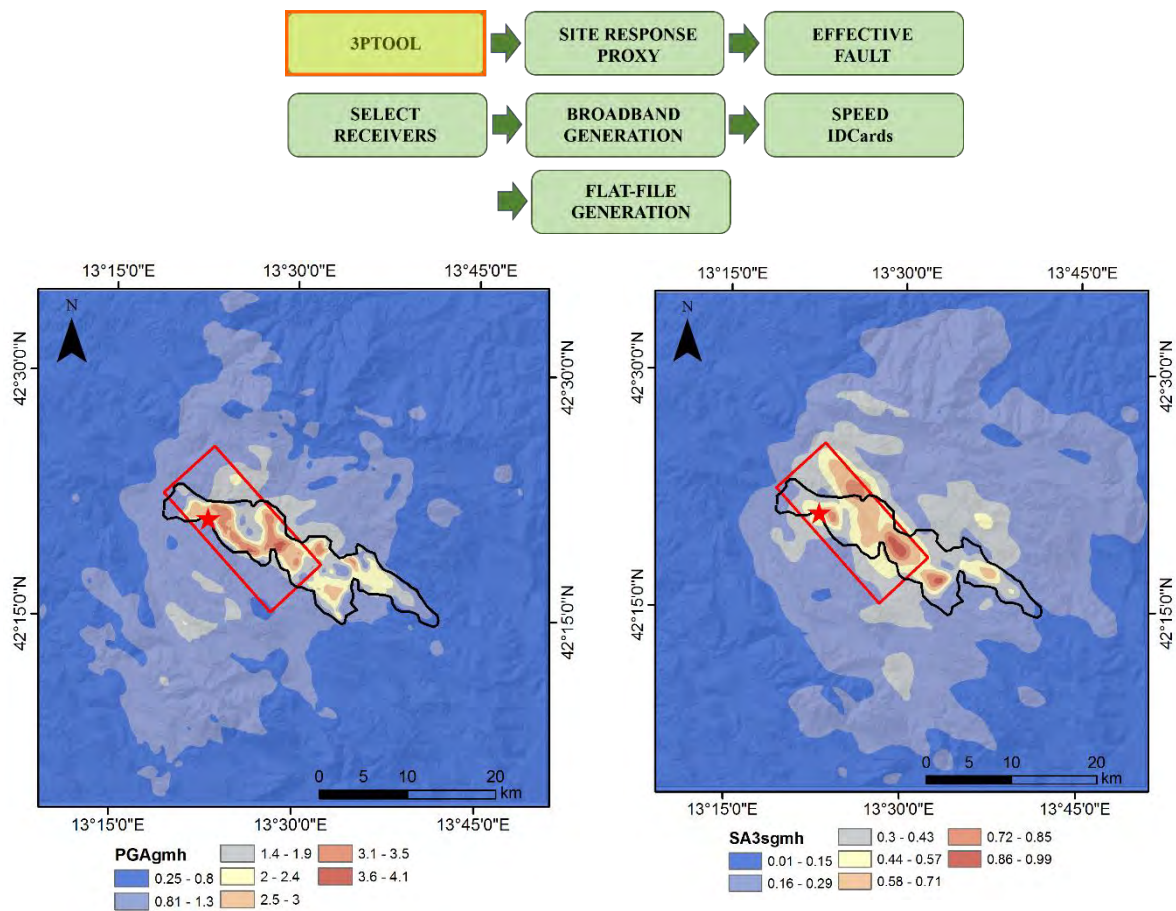


Figure 2.2 3PTOOL: generation of ANN2BB ground motion maps in terms of PGA for horizontal geometric mean, HGM, (left) and SA(3s) (right).

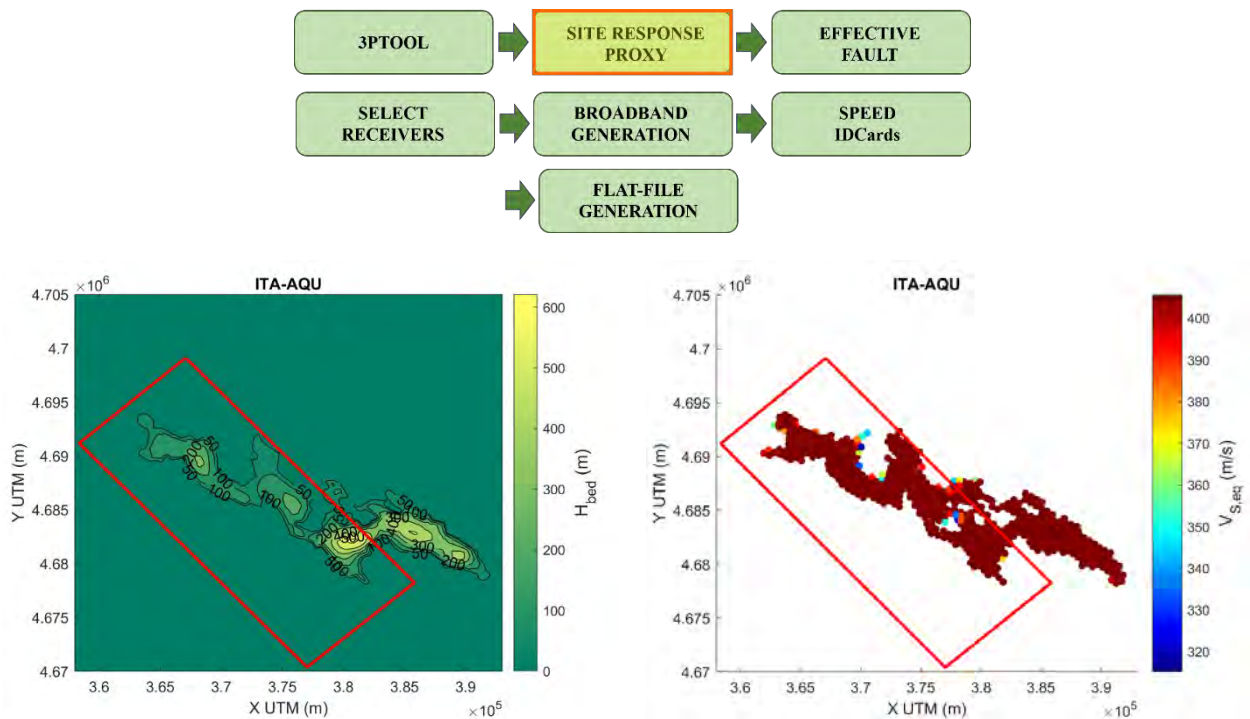


Figure 2.3 SITE RESPONSE PROXIES: H_{bedrock} (left) and V_{s,eq} (right) maps.

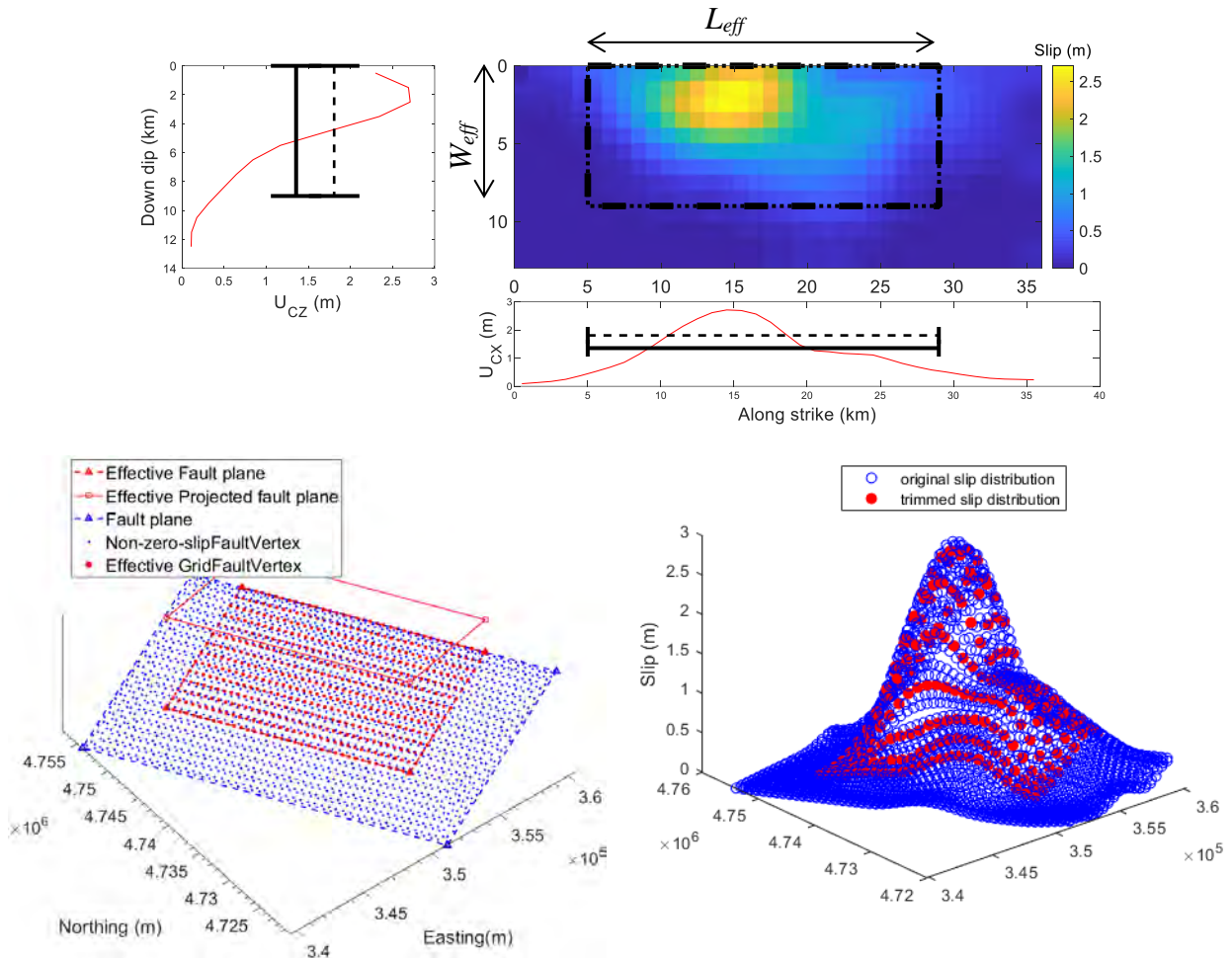
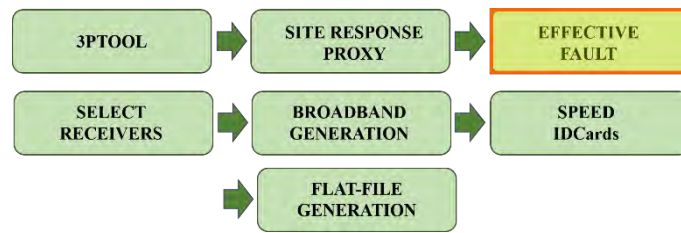


Figure 2.4 *EFFECTIVE FAULT*: plan (top) and 3D (bottom) views of the effective dimensions of the rupture area and the trimmed slip distribution on the fault plane.

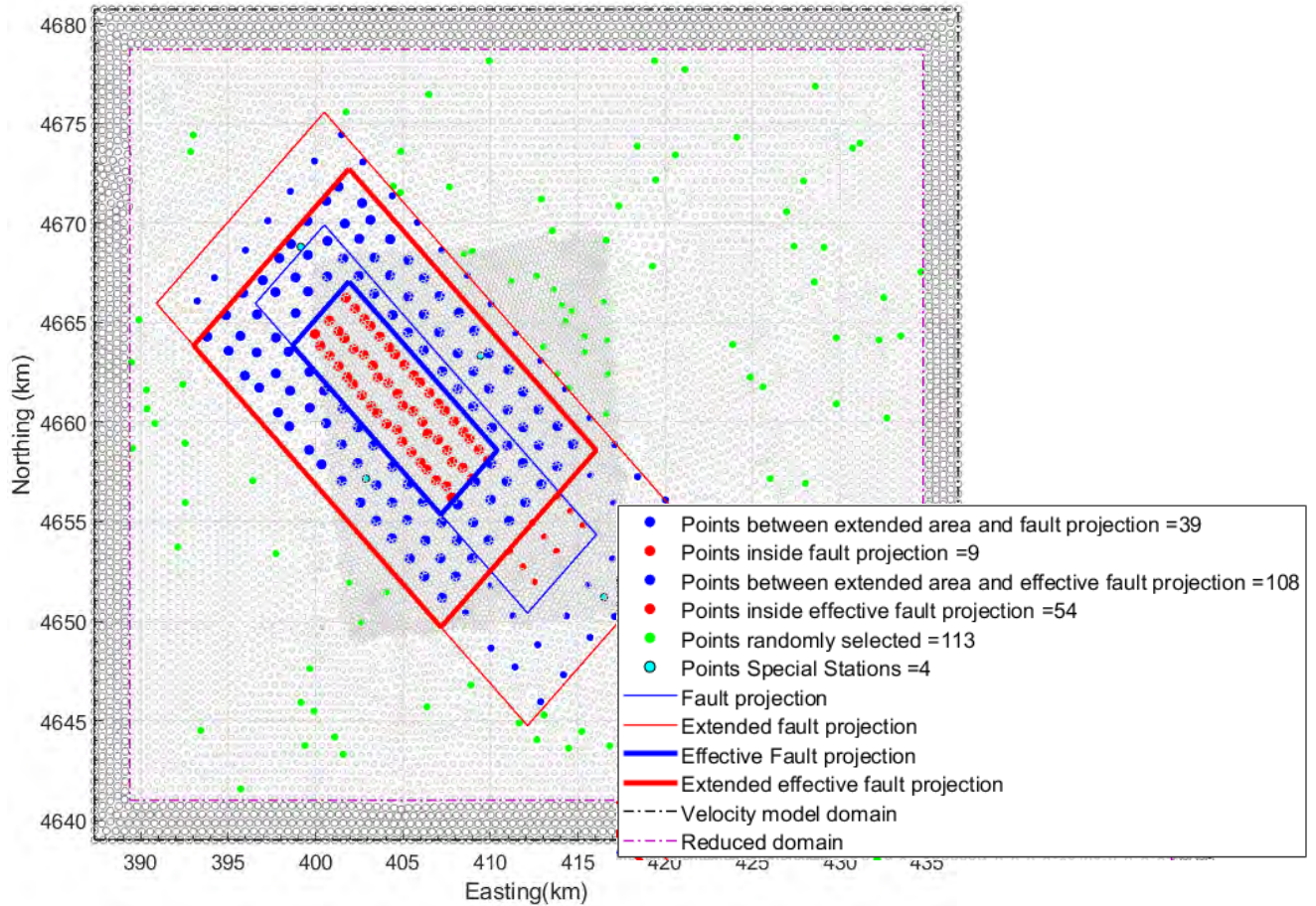
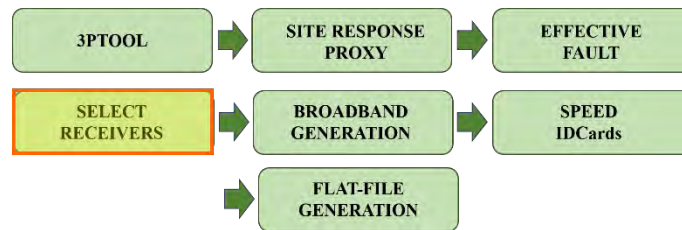


Figure 2.5 *SELECT RECEIVERS*: selection of a subset of **SPEED receivers**, with variable sampling depending on the proximity to the fault, for subsequent generation of broadband time histories.

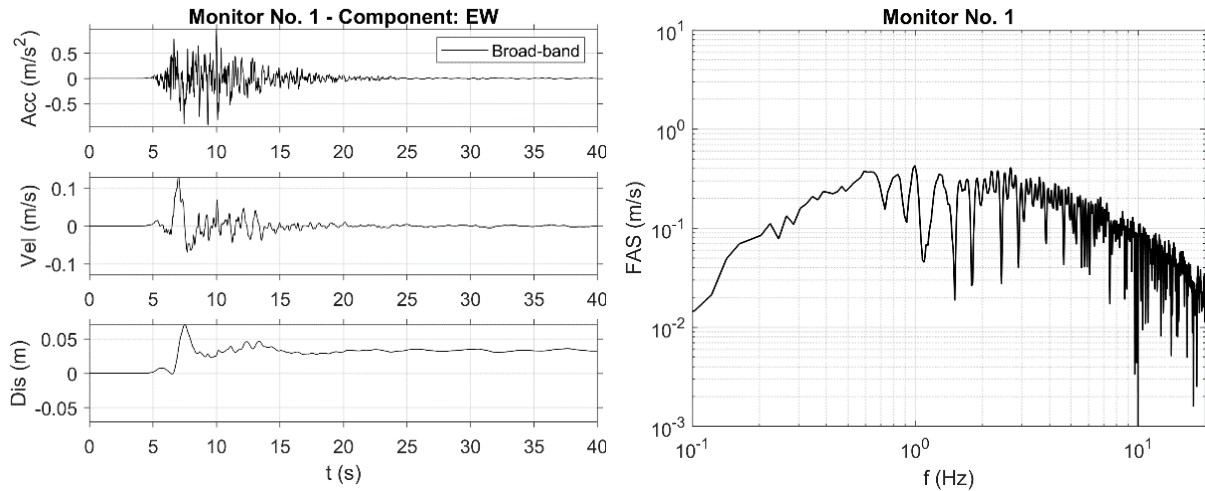
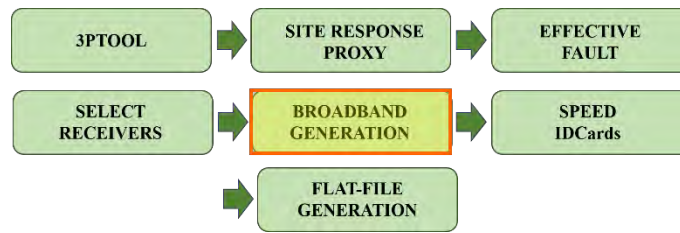
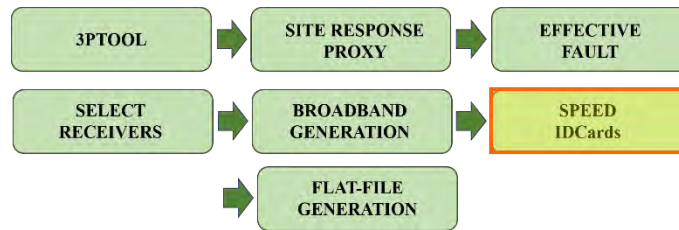


Figure 2.6 **BROADBAND GENERATION**: generation of broadband time histories starting from SPEED results according to the revised ANN2BB approach. Acceleration, velocity and displacement waveform (left) and corresponding Fourier Amplitude Spectra FAS (right) of ANN2BB time history.



ITA_2009.04.06_03.32It_Mw6.3

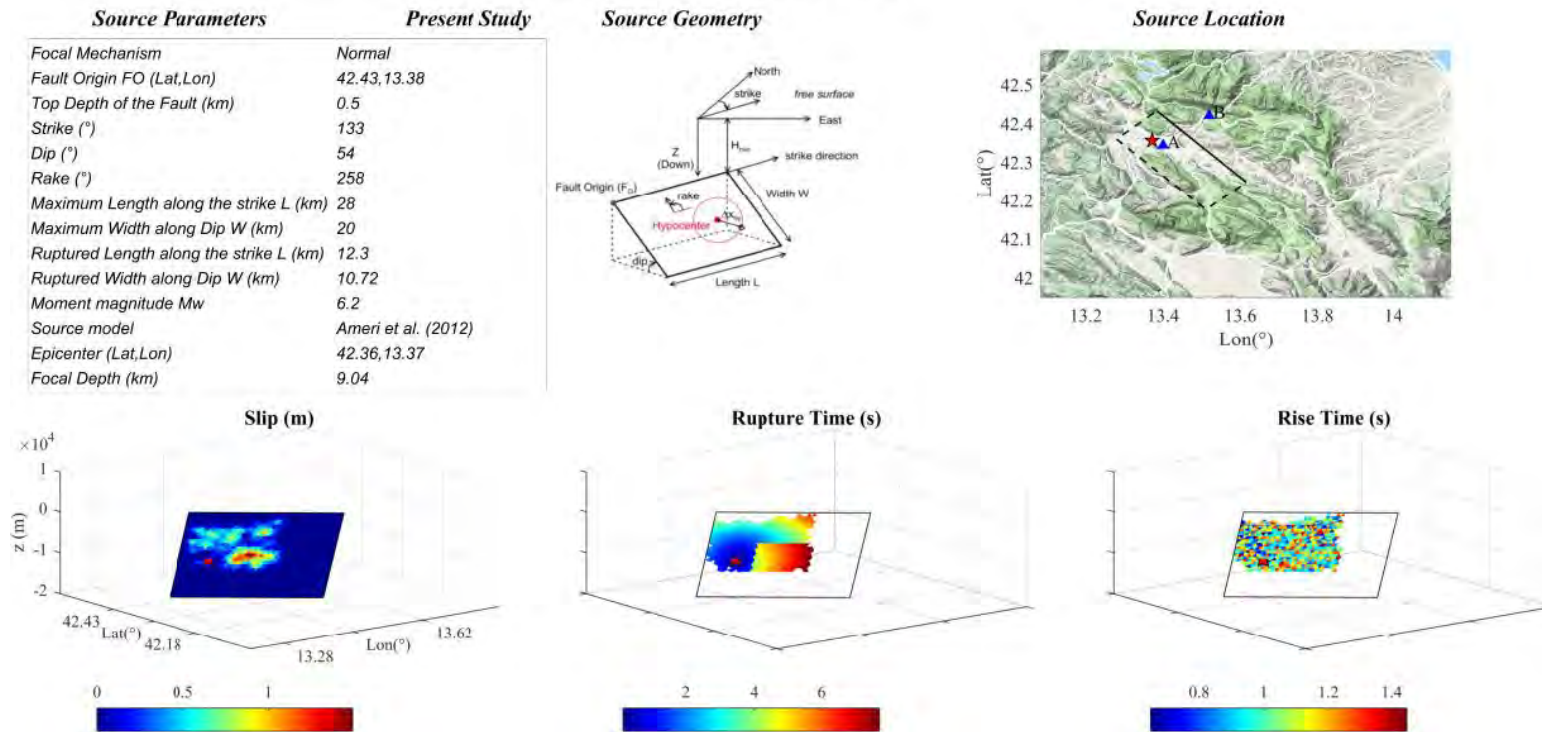
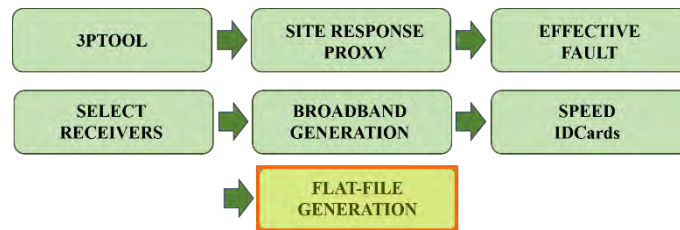


Figure 2.7 *SPEED IDCards*: extract of summary sheet with model parameters (source geometry and rupture properties).



Source Metadata	Receiver Metadata	Site Response Proxies	Source-to-Site Distances (**)	Intensity Measures (***)
<ul style="list-style-type: none"> • Scenario ID • Event ID • Scenario ID card • Event_Time • Event Nation Code • Hypocenter Lat/Lon/Depth • Mw • Mo • Average slip • No. segments • Strike • Dip • Rake • Fault mechanism • Rupture top • Fault Vertices (*) • Length (*) • Width (*) • References • ANN_database • Transition period • ANN2BB_procedure 	<ul style="list-style-type: none"> • Monitor ID • Monitor East/North coordinates • Monitor elevation 	<ul style="list-style-type: none"> • $V_{s,30}$ • Depth to geological bedrock • time-averaged V_s to bedrock • Depth corresponding to $V_s=800$ m/s • time-averaged V_s to depth corresponding to $v_s=800$ m/s • V_s equivalent (NTC2018) 	<ul style="list-style-type: none"> • Epicentral distance • Hypocentral distance • R_{line} • R_x • Joyner and Boore distance, R_{jb} • R_{rup} 	<ul style="list-style-type: none"> • PGA • PGV • PGD • PSA(T) for T from 0.01 to 10 s • Permanent displacement • Pulse-like flag • Pulse period • Ds595, Ds575 • Housner Intensity • Arias Intensity • Cumulative Absolute Velocity • Mean period

Figure 2.8 FLATFILE GENERATION : flatfile general structure. See Table 4.1 and Appendix B for a through explanation of all terms.

SECONDARY POST-PROCESSING STREAM

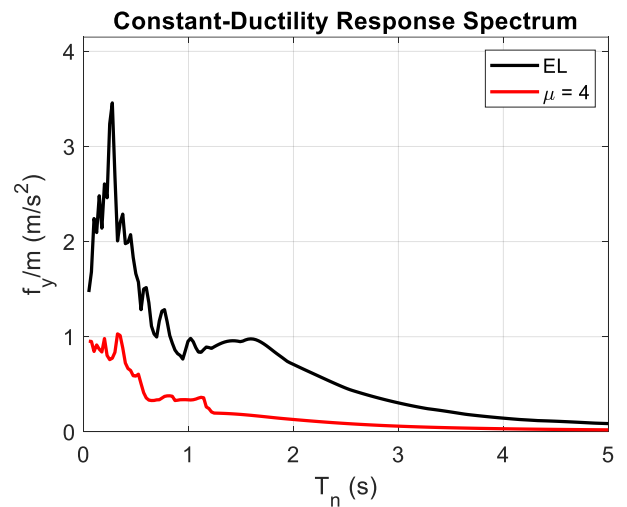
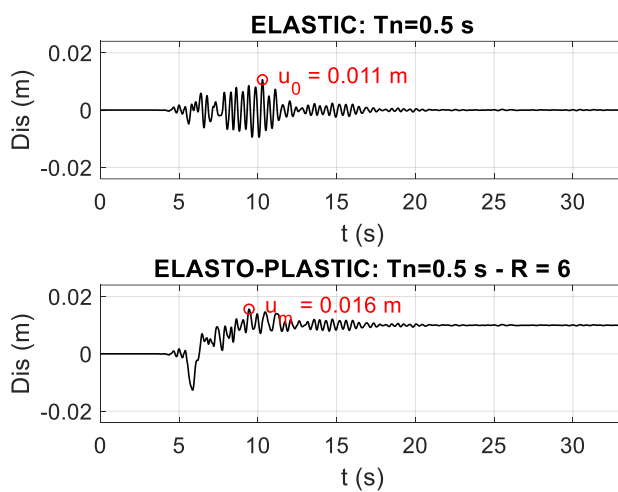
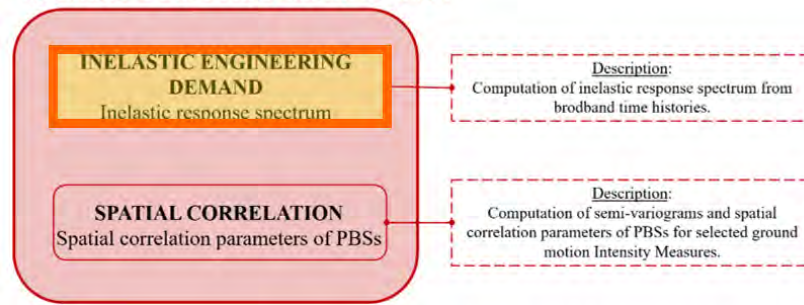


Figure 2.9 *INELASTIC ENGINEERING DEMAND*: computation of elastic Vs elastoplastic response of a SDOF system subject to the broadband motion of Figure 2.6. Left: time history response for vibration period $T=0.5$ s and yield strength reduction factor $R=6$; right: constant-ductility ($\mu=4$) response spectrum for yield strength.

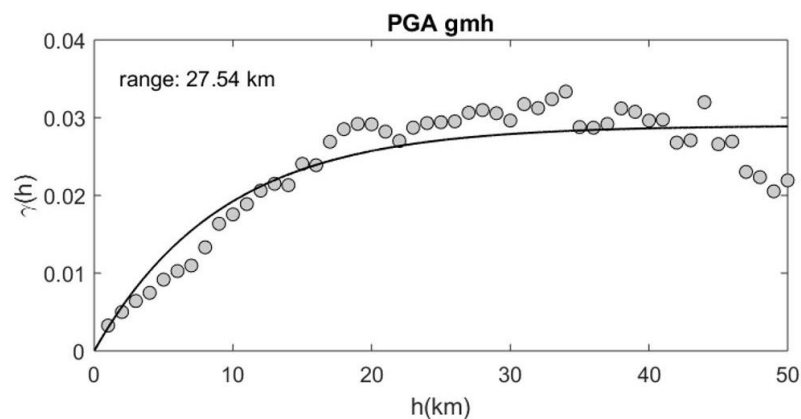
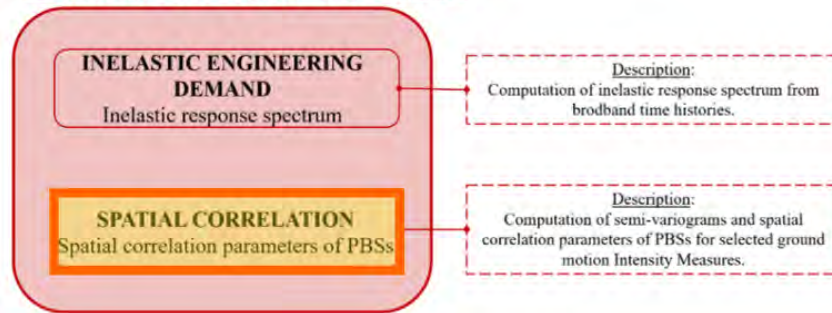
SECONDARY POST-PROCESSING STREAM


Figure 2.10 SPATIAL CORRELATION: computation of semi-variogram γ as a function of inter-station distance h and fitting with an exponential model.

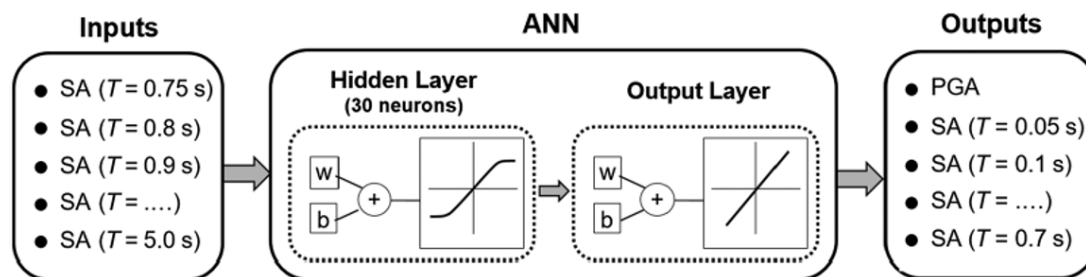


Figure 2.11 ANN TRAINING: training of an ANN for a set of inputs (left) and outputs (right) and based on a given architecture (hidden layers, output layers).

2.2 ANN2BB approach for the generation of broadband ground motions

Physics-based numerical simulations (PBS) rely on the rigorous numerical solution of the seismic wave propagation problem, based on 3D models both of the seismic source (either kinematic or dynamic) and of the source-to-site propagation path. However, the accuracy of the PBS is limited to the long period range $T \geq T^*$, with T^* being typically in the range of 0.5 - 1 s (see maximum frequency in Table 1.1), mainly due to the lack of knowledge about the Earth crust and earthquake rupture process at short-wavelength and partially due to the computational cost of large and fine grids.

For this reason, a fundamental step of SPEED processing concerns the generation of broad-band ground motions, where the low-frequency simulated waveforms are enriched in the high-frequency

range to produce time histories with a realistically broad frequency content. This is an essential step for the purpose of seismic analyses of engineered systems as well as seismic risk evaluations when simulated ground motions are used to characterize the seismic input.

The actual procedure used to generate broad band time histories, is the one summarized in Figure 2.12, its main steps are given in the following.

- (1) An ANN is trained based on a dataset of strong motion records to predict short period spectral ordinates ($T < T^*$) based on long period ones ($T \geq T^*$), being T^* the minimum period of the numerical model. The recording dataset may be selected by the user among the ones available in the literature, such as SIMBAD (Smerzini et al. 2014) or NGA-West 2 (Ancheta et al. 2013). ANNs are trained separately on the geometric mean of the horizontal components and on the vertical components to allow the prediction of three-component ground motions.
- (2) For each simulated waveform, a target ANN2BB response spectrum is computed, the spectral ordinates of which, for $T \geq T^*$, coincide with the simulated ones, while, for $T < T^*$, they are obtained from the ANN (separately for horizontal and vertical components). The target at low periods is built on the median value calculated over 20 ANN realizations.
- (3) The high-frequency contribution for the simulated waveforms is computed using the Sabetta and Pugliese (1996) approach. Namely, 20 stochastic realizations are generated for each waveform, according to the simulated scenario (M_w) and receiver (distance, site conditions). Out of these, the stochastic signal with the minimum misfit with respect to the target is selected and scaled to generate the HF ground motion.
- (4) The scaled stochastic waveforms and the PBS, filtered in the high and low frequency range respectively, are combined in the time domain. Phase matching between HF and LF is achieved by alignment of the two time histories according to the instant at 5% of normalized Arias intensity.

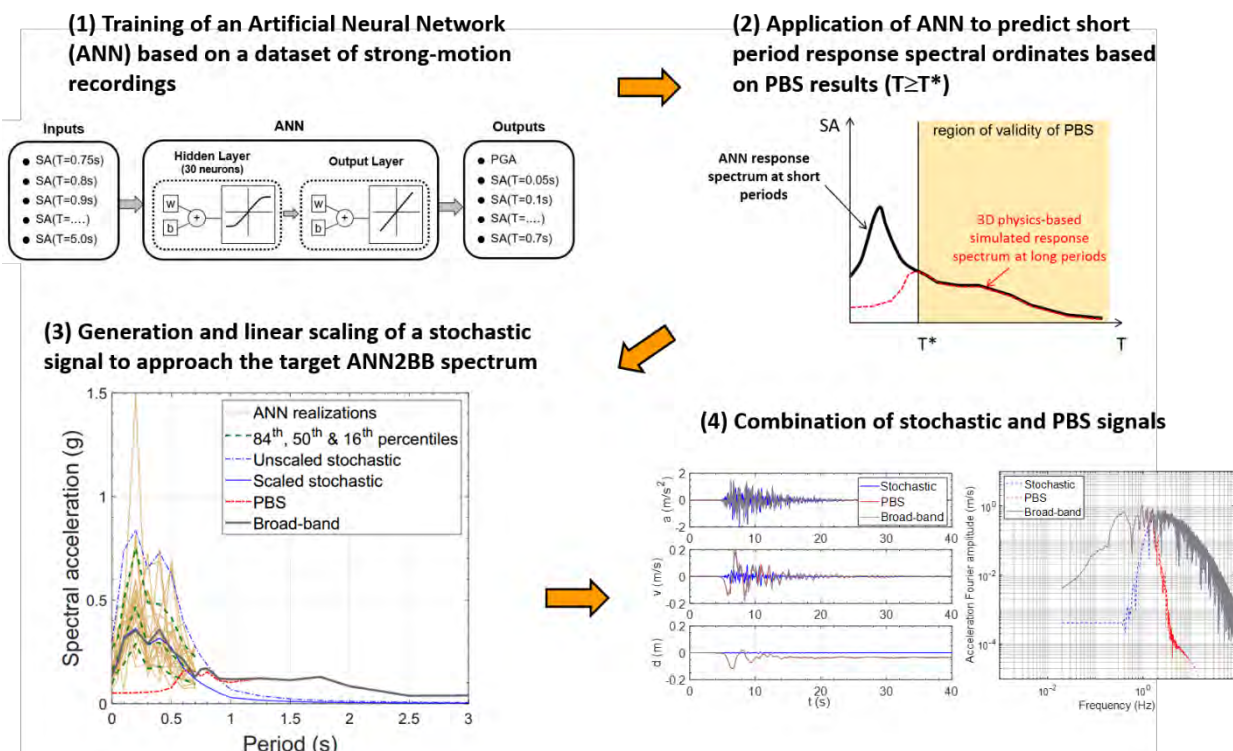


Figure 2.12 Flowchart of the ANN2BB approach for the massive processing of PBS for broadband computation.

This procedure has been set up starting from the one published in Paolucci et al. (2018). The revision of the original procedure was made necessary to make the ANN2BB approach suitable for massive processing of PBSs in a semi-automatic way. The main difference with respect to Paolucci et al. (2018) (to which we refer to for a detailed description of the prerequisites of the approach and its validation against real case studies) are the following:

- 1) for each receiver, the target ANN2BB in the high frequency range is computed as the median of 20 different ANN realizations rather than the output of a single ANN⁴;
- 2) the stochastic ground motion is linearly scaled in the response spectrum domain to fit the target ANN2BB spectrum at short periods and, then, combined with the PBS. In this way, the iterative scaling in the frequency domain of the original procedure is not performed any more.

The fit to the target ANN2BB spectrum is controlled by a weight vector. The fit is actually performed only on the HF range, and for this reason the weight vector takes a value of 0 at periods larger than the merging one (LF range), and a value of 1 at lower periods (HF range). At the merging period a value of 2 is recommended. These values were selected after appropriate sensitivity analyses and they ensure that at the end of the procedure, the final spectrum is 'as close as possible' to the PBS one in the LF range, including the merging period.

We point out that the scaling and selection of the stochastic waveforms is based on a two-step procedure of minimization of the residuals with respect to the target spectrum; these residuals are analytically computed using Equation 2.1. For each realization, a scaling factor SF that minimizes the residuals with respect to target ANN is calculated, and then among the $nsim$ different stochastic realizations, the stochastic signal with the minimum misfit is selected.

$$\min_{nsim} r^{nsim} = \min_{nsim} \left(\min_{SF} \sum_{i=1}^{N_{periods}} w_i \left(\frac{\ln ANN_{median,i} - \ln(SF * STOCH_i^{nsim})}{\sigma_{\ln ANN,i}} \right)^2 \right) \quad (2.1)$$

In the equation above, SF is the scaling factor, $N_{periods}$ are the vibration periods of the target spectrum, w_i is the weight-vector and $STOCH^{nsim}$ is the $nsim^{th}$ stochastic realization. The median and standard deviation of the 20 ANN are used to calculate the misfit. In our procedure, we use $nsim = 20$ in order to achieve a satisfying final spectrum.

In addition to efficiency reasons, the revised ANN2BB approach overcomes issues related to unrealistic frequency content at both intermediate and high frequency ranges numerically introduced by previous manipulation of Fourier spectra for specific cases. A comparison of results between the original and revised ANN2BB procedures is shown in Figure 2.13, in both time and frequency domain. Note the troughs at intermediate frequencies and the unrealistic high content at higher frequencies.

These improvements made the broadband generation tool of SPEED post-processing workflow capable of conducting broadband ground motion generation for a large number of receiver points with no manual interventions, facilitating time-efficient yet reliable outputs.

⁴ The choice to compute the target ANN2BB spectrum as the median of 20 ANN realizations (for varying initial weights and dataset subsets) was based on sensitivity tests to achieve a greater stability of results and minimize overfitting issues.

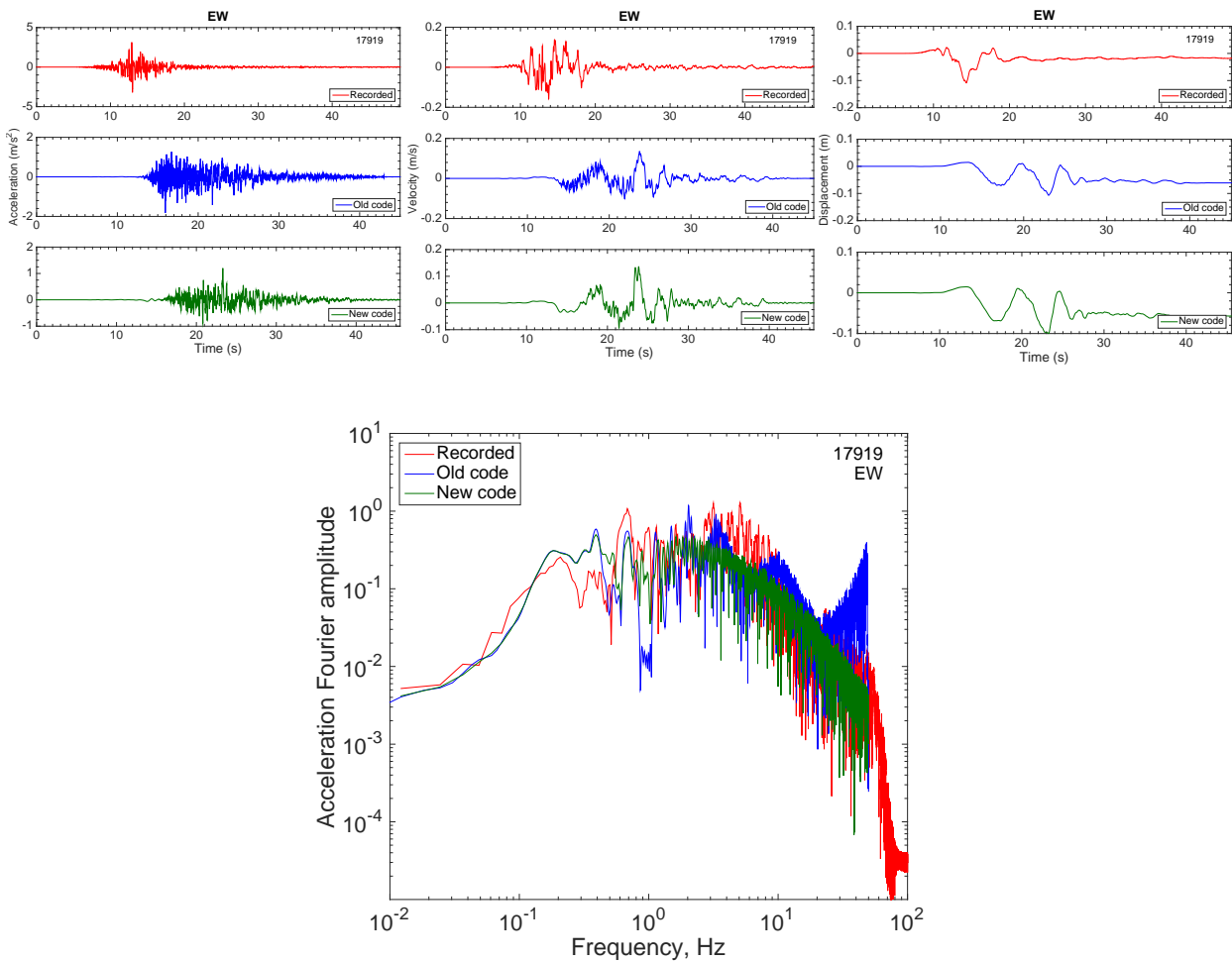


Figure 2.13 Comparison between broad band signals computed following the original (*old*, in blue) and adopted (*new*, in green) ANN2BB procedure. Recorded signal is shown as well. (From Norcia simulations).

3. Overview of processed numerical simulations

An overview of the PBSs computed through SPEED in different research programs (2009-2020) is given in Table 1.1. In all these applications, a 3D representation of geomorphologic structure of the target area has been included. Further details and information can be found on SPEED website (<http://speed.mox.polimi.it/>). In this table, the numerical scenarios included in the first (prototype) version of the synthetic database presented in this report (BB-SPEEDset_V0) are highlighted in orange.

The PBSs included in BB-SPEEDset_V0 are listed in Table 3.1 and involve mainly (but not only) the numerical simulation of significant Italian earthquakes, namely: (1) the January 13 1915 Marsica earthquake, Central Italy; (2) the April 6 2009 L'Aquila earthquake, Central Italy; (3) the May 29 2012 Po Plain earthquake, Northern Italy, (4) the October 30 2016 Norcia earthquake, Central Italy and (5) the February 22 2011 Christchurch earthquake, New Zealand. It is worth underlining that for each scenario included in BB-SPEEDset (V0) a series of investigations related to the specificity of the earthquake and geological area under consideration was carried out and a detailed discussion on the validation against observations⁵ (including comparison of waveforms, Fourier/response spectra and quantitative Goodness-Of-Fit scores) was published. The reader is referred to the relevant publications, as listed in the last column of Table 1.1, for a thorough presentation of the scientific results concerning these simulations and their verification/validation. For this reason, preference has been given to the Italian earthquakes, for which Politecnico di Milano was involved in projects of national relevance, but further scenarios, not limited to the Italian context, will be included in the next version of the database.

For each PBS included in BB-SPEEDset_V0, fact-sheets with input data (mesh, kinematic seismic source and site response proxies) and output results are provided in Appendix C. Output results include:

- peak ground shaking maps of Peak Ground Acceleration (PGA), Peak Ground Velocity (PGV) and Spectral Acceleration (SA) at 3s, for the Fault Normal (FN), Fault Parallel (FP), Horizontal Geometric Mean (HGM), Up-Down (UD) components, as well as for the FN/FP and UD/HGM ratios;
- graphs showing the attenuation with distance (namely, R_{line} , see definition in Section 5.1) of PGA, PGV and SA(3s), for the components and ratios listed above.

It is worth underlining that the construction of BB-SPEEDset_V0 has implied the processing of 2844 three-component waveforms. As a set of illustrative results, Figure 3.2 to Figure 3.3 show, for the L'Aquila case study (Aqu_Mw6.2), the broadband three-component (EW, NS and UD) acceleration, velocity and displacement time histories at selected receiver points, superimposed on the corresponding Peak Ground Acceleration (PGA), Peak Ground Velocity (PGV) and Peak Ground Displacement (PGD) maps. Although a detailed analysis is not reported here, it is noted that synthetic time histories have realistic features in terms of duration, amplitudes and frequency content, with displacement waveforms showing permanent displacements related to the fault offset. Furthermore, spatial distribution of peak ground motion values at high frequency (PGA) turns out to be well correlated with the geological features of the basin, proving once again the goodness of the ANN2BB approach in establishing a correlation between long and short period ordinates and, thus, reproducing at short periods physics-based features which are simulated only at long periods.

Concerning Christchurch simulation, included in the current version of the dataset, the authors are aware of simulation issues related to the lack of an appropriate description of non-linear soil behavior and to super-shear effects due to the kinematic source representation inside the basin. A revision of the model is planned and the new results will be included in the next version of the dataset.

⁵ Note that, for the 1915 earthquake, simulations were validated against geodetic measurements made before and after the occurrence of the event. Simulated and observed permanent displacements were in reasonable agreement with each other.

Table 3.1 PBSs included in the BB-SPEEDset_V0.

Case Study	Name	Scenario_ID	Mw
Fucino Plain, Marsica, Central Italy	Mar_Mw6.7	ITA_1915.01.13_06.52It_Mw6.7	6.7
L'Aquila, Central Italy	Aqu_Mw6.2	ITA_2009.04.06_03.32It_Mw6.2	6.2
Po Plain, Northern Italy	PP_Mw6.0	ITA_2012.05.29_09.00It_Mw6.0	6.0
Norcia, Central Italy	Nor_Mw6.5	ITA_2016.10.30_07.40It_Mw6.5	6.5
Christchurch, New Zealand	Chc_Mw6.3	NZL_2011.02.22_12.51It_Mw6.3	6.3

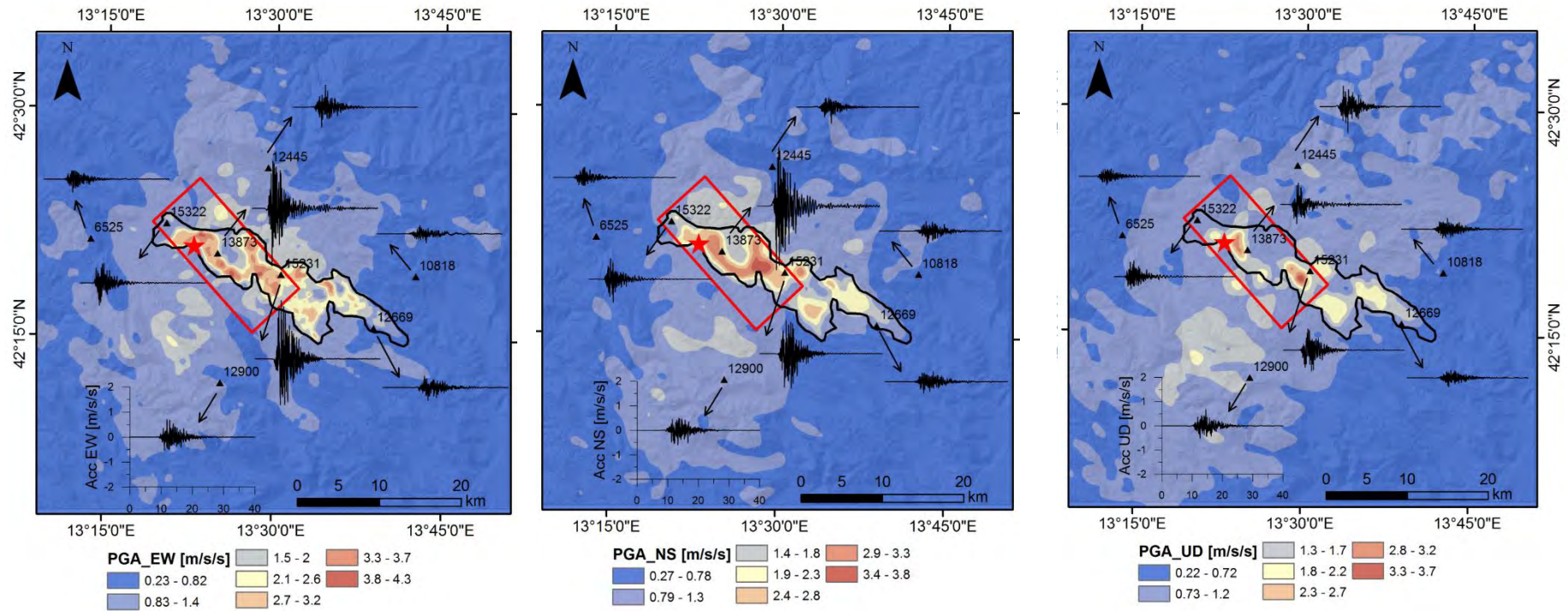
Aqu_Mw6.2


Figure 3.1 Aqu_Mw6.2: PGA maps and broadband acceleration time histories at selected receivers (left: EW; center: NS; right: UD).

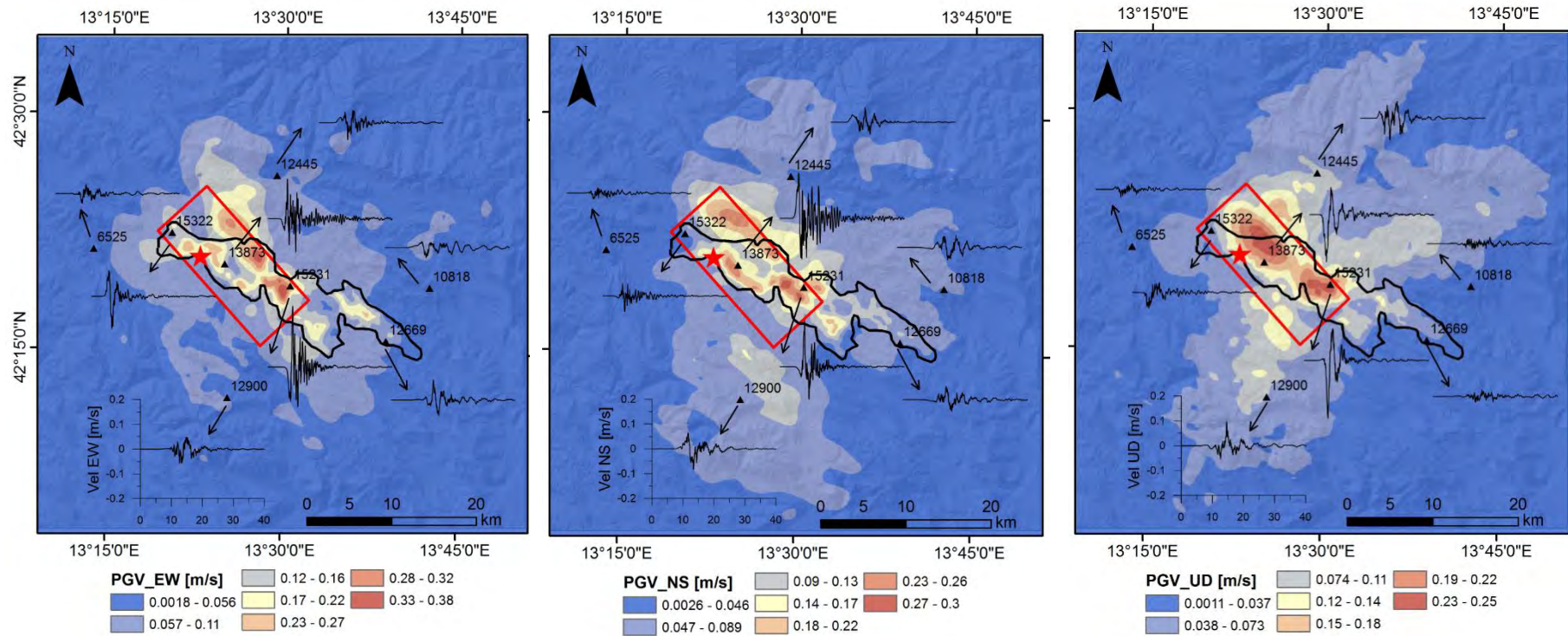
Aqu_Mw6.2


Figure 3.2 Aqu_Mw6.2: PGV maps and broadband velocity time histories at selected receivers (left: EW; center: NS; right: UD).

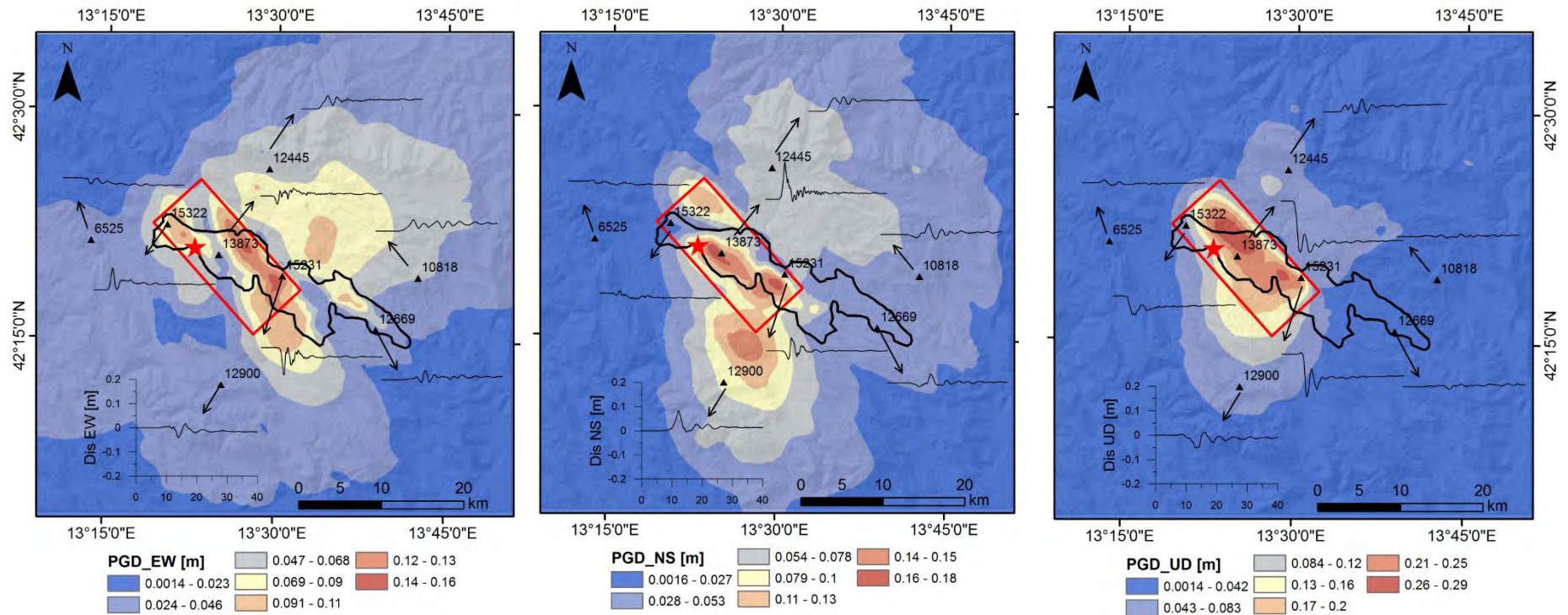
Aqu_M_w6.2


Figure 3.3 Aqu_Mw6.2: PGD maps and broadband displacement time histories at selected receivers (left: EW; center: NS; right: UD).

4. Organization of a flatfile for the BB-SPEEDset_V0

Flatfiles are provided in a .csv and .mat format, respectively for Excel and Matlab post-processing. For each scenario and each selected receiver, a list of source metadata, post-processing metadata, receiver metadata, site response proxies, source to site distances and intensity measures (IM) are computed and provided (see Table 4.1 for all details regarding the metadata and IMs actually stored). Note that “Source Metadata” are stored separately from the other data, as they are common to all receivers of a given scenario simulation. When considering a synthetic database, it is relevant to store information regarding the type of post-processing accomplished, such as ANN training database, ANN transition period, broadband procedure (stored in “Source Metadata”). Figure 4.1 and Figure 4.2 show parts of flatfile structures for scenario and receiver information respectively. The fields of the flat file are consistent with the Engineering Strong-Motion (ESM) flat file (Lanzano et al., 2018) and the INGV NESS flatfile (Pacor et al., 2018). A complete description of each field of the flatfile is provided in Appendix B.

Table 4.1. Structure of the flatfile for BB-SPEEDset_V0. A detailed description of the different field names is given in Appendix B.

Source Metadata	Receiver Metadata	Site Response Proxies	Source-to-Site Distances (**)	Intensity Measures (***)
<ul style="list-style-type: none"> • Scenario ID • Event ID • Scenario ID card • Event_Time • Event Nation Code • Hypocenter Lat/Lon/Depth • Mw • Mo • Average slip • No. segments • Strike • Dip • Rake • Fault mechanism • Rupture top • Fault Vertices (*) • Length (*) • Width (*) • References • ANN_database • Transition period • ANN2BB_procedure 	<ul style="list-style-type: none"> • Receiver ID • Receiver East/North coordinates • Receiver elevation 	<ul style="list-style-type: none"> • $V_{s,30}$ • Depth to geological bedrock • time-averaged V_s to bedrock • Depth corresponding to $V_s=800$ m/s • time-averaged V_s to depth corresponding to $v_s=800$ m/s • V_s_equivalent (NTC2018) 	<ul style="list-style-type: none"> • Epicentral distance • Hypocentral distance • R_{line} • R_x • Joyner and Boore distance, R_{jb} • R_{rup} 	<ul style="list-style-type: none"> • PGA • PGV • PGD • PSA(T) for T from 0.01 to 10 s • Permanent displacement • Pulse-like flag • Pulse period • D_{s595}, D_{s575} • Housner Intensity • Arias Intensity • Cumulative Absolute Velocity • Mean period

(*) Fault dimensions are given with respect to ‘numerical fault’ and ‘effective fault’

(**) distances from the fault are computed with respect to its “effective” dimensions

(***) Except pulse features, Intensity Measures are defined for the following directions: NS, EW = horizontal; UD = vertical; HGM= horizontal geometrical mean; FN=Fault Normal; FP=Fault Parallel; RotD50 = median value of the IM distribution obtained from rotated waveforms; RotD100 = maximum value of the IM distribution obtained from rotated waveforms. (Rotation angles are given as well.)

scenario_id	event_id	scenario_ID_card	event_time	nation_code	hypo_latitude	hypo_lo
SPEED_ITA_1915.01.13_06.52lt_Mw6.7	--	https://bit.ly/ITA_MAR_13_01_1915	13-01-15 06:52	IT		41.97

Figure 4.1 Part of the flatfile table with the information listed and stored for each processed scenario (“Source Metadata”).

monitorID	easting	northing	elevation	vs30	H_bedrock	vs_bedrock	H_800	vs_H800	vs_eq	R_epi	R_
7898	632062.64	5170624.7	324.65	303.38331	919.0369	870.91779	233	1209.3066	303.38331	7301.4803	997
8034	631822.21	5171059.4	252.34	303.38331	974.10328	887.45567	233	1209.3066	303.38331	7217.4072	986
8047	632321.91	5171052.2	292.05	303.38331	955.04646	881.78304	233	1209.3066	303.38331	6828.1466	961
8158	631581.54	5171493.9	170.17	303.38331	968.30395	885.725	233	1209.3066	303.38331	7167.1684	977
8159	632080.71	5171487.4	219.33	303.38331	882.32646	859.71107	233	1209.3066	303.38331	6756.815	950
8278	631839.49	5171922.2	151.08	303.38331	1051.3503	910.27406	233	1209.3066	303.38331	6721.8791	943

Figure 4.2 Part of the flatfile table with the information listed and stored for each processed receiver.

Since directional effects may be significant in the near source region, different IMs on the horizontal plane have been calculated. These include: the fault normal (FN) and fault parallel (FP) components, calculated rotating the horizontal waveforms orthogonal and parallel to strike of the fault, respectively; the horizontal geometric mean (HGM) computed using the two horizontal EW and NS components; the maximum (RotD100) and the median (RotD50) values of IMs over all orientations (Boore, 2010).

The distribution of BB-SPEEDset_V0 data (including the 5 scenarios of Table 3.1) with respect to magnitude, distance, site conditions and style of faulting is given in Figure 4.3. The flatfile dataset covers distances of up to 40 km when measured in terms of R_{JB} , with magnitudes from 6.0 to 6.7. In the same figure, the distribution of the NESS dataset is shown for comparison (a); as evident, the use of simulations allows a better distribution of data at short distances, for any magnitude, with respect to recording stations. Normal, and thrust focal mechanisms are actually included in the dataset, with a dominance of normal events.

Average shear-wave velocity in the uppermost 30 m ($V_{s,30}$) was assigned to all receiver points; $V_{s,30}$ for soft soil condition are mainly characterized by a 300 m/s velocity, while outcropping bedrock conditions are mainly characterized by velocities higher than 900 m/s⁶.

Figure 4.4 shows the cumulative distribution function of RotD100 for PGA and RotD100 PGV of all receiver points within the processed scenarios of the flatfile dataset. Following previous studies (Pacor et al., 2011), we defined as “extreme waveforms”, those having PGA, or PGV, exceeding a peak ground value with a probability of exceedance less than 5% in the related distribution (as highlighted in Figure 4.4). With this criterion, a set of receivers has been identified within each scenario and plotted in Figure 4.4, on the right, as a function of rupture distance and magnitude. No clear dependence on distance is observed at the moment. Figure 4.5 shows the distribution of the previously defined ‘extreme’ values,

⁶ In the Norcia and L’Aquila simulations large $V_{s,30}$ values for the outcropping bedrock were considered ($V_s=1700$ m/s), for the results to be used as input for site-specific 1D response analyses to account for specific features of alteration and scattering from surficial rock materials. Eventually, this choice implied in general lower amplitude of ground motion than with a standard outcropping bedrock with V_s in the range of 800-1000 m/s.

with respect to distance and magnitude, calculated for the entire NESS dataset (from DPC - RELUIS 2016 report); it is to be noted that the range of amplitudes of PGA and PGV of the synthetic and recorded near-source datasets is in rather good agreement, within the same ranges of M_w and distances.

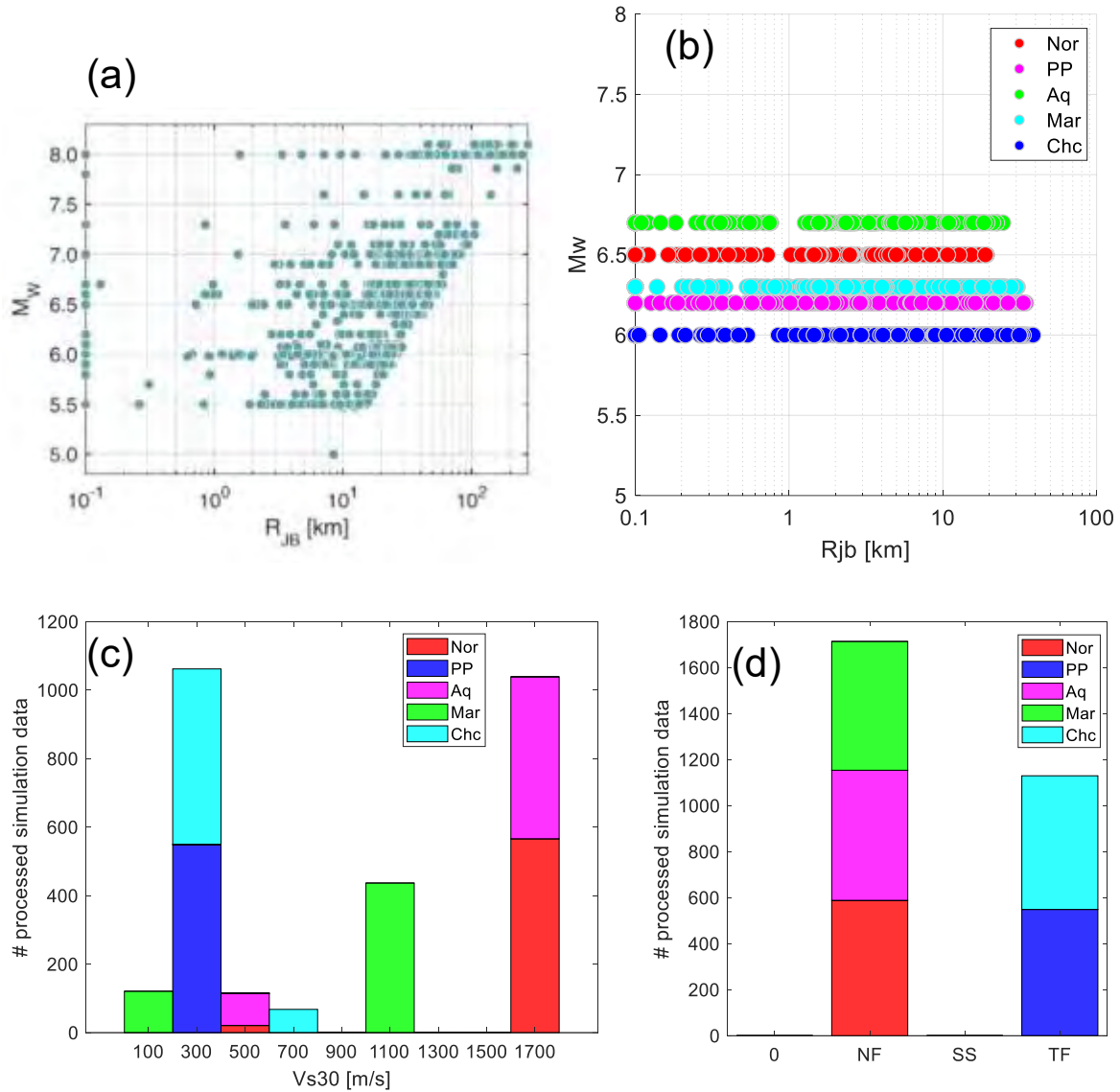


Figure 4.3 Flatfile data distribution of BB-SPEEDset_V0 at current stage of work, compared with NESS data set (a, from DPC - RELUIS 2016 report). For flatfile: (b) M_w vs R_{JB} ; (c) number of processed receiver points with respect to $V_{s,30}$; (d) number of processed receiver points with respect to style of faulting.

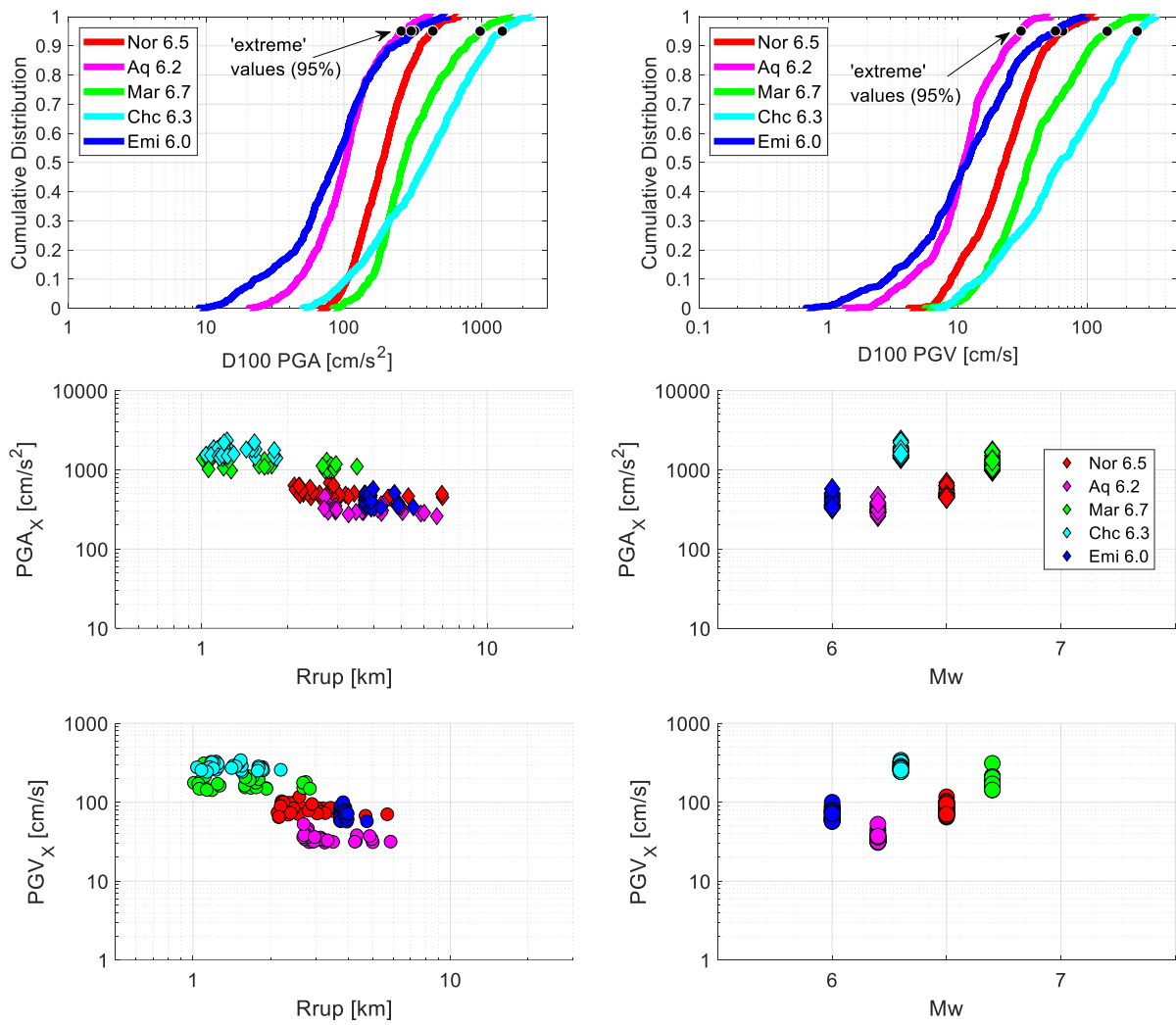


Figure 4.4. (*top*) Cumulative distribution function of RotD100 PGA and RotD100 PGV of flatfile datasets. (*bottom*) “Extreme” values of PGAs (diamonds) and PGVs (circles) versus rupture distance and moment magnitude M_w . The data are colored according to the corresponding simulation.

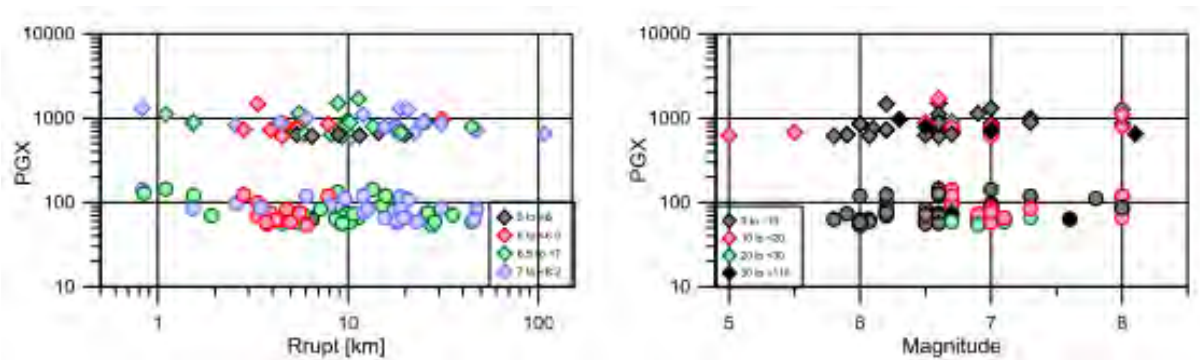


Figure 4.5. From NESS database: “extreme” PGAs (diamond) and PGVs (circles) versus rupture distance and moment magnitude. The data are colored according to magnitude (*left*) and rupture distance (*right*). Figures from DPC - RELUIS (2016) report.

5. Towards a near-source ground motion model from PBS

As well known, GMPEs provide the probability distribution of a prescribed IM as a function of a few explanatory variables, such as magnitude, source-to-site distance, site characteristics and source characteristics (style of faulting). Results depend on the adopted functional form and on the selected recorded ground motion dataset. Predictions of near source ground motion are not always consistent with records, mainly because of two reasons: on one side the paucity of near-source recordings in actual databases, on the other side the peculiarity of near-source features. Effects observed in the near-source regions typically involve polarization of motion, directionality, directivity, pulse-like ground motion, permanent displacements, and hanging-wall (HW) or footwall (FW) characteristics.

For these reasons, particular care was taken in this phase of the work to the analysis of the database, in order to identify the main aspects of ground motion, according to the mentioned near source peculiarities, namely: the performance of different source-to-site distance metrics (Section 5.1), the definition of a simple but representative attenuation model with distance (Section 5.2), analysis of ground motion directionality, in terms of FN/FP and Vertical-to-Horizontal (V/H) ratios, as a function of distance (Sections 5.3 and 5.4).

Considerations and results are strictly related to the range of magnitudes, distances and source characteristics of the processed scenarios, included in the BB-SPEEDset_V0 dataset (see Figure 4.3).

For each scenario of Table 3.1, selected ground motion intensity measures, such as PGA, PGV and SA(3s) have been analyzed with reference to different components of motion (including FN/FP and V/H ratios), distances from the source, position with respect to the source and site characteristics.

5.1 Effect of different source-to-site distance metrics

The aim of this Section is to analyze the impact of different source-to-site distance metrics on the prediction of peak ground motion values (maximum amplitudes and corresponding variability) and their attenuation with distance, particularly in the vicinity of the fault. In the following analyses, all distance metrics have been calculated using the 'effective' source dimensions, so that they can be regarded as effective source-to-site distances, consistent with the magnitude of the simulated scenario.

Some common source-to-site distance metrics have been computed for each receiver point in the flatfile, namely: epicentral distance (R_{epi}), hypocentral distance (R_{hyp}), Joyner and Boore distance (R_{JB}), rupture distance (R_{rup}), the horizontal distance R_X (defined below and shown in Figure 5.1) together with an alternative distance metric, first introduced by Paolucci et al. (2016), called R_{line} . As sketched in Figure 5.2, R_{line} is defined as the closest distance from the surface projection of the top edge of the fault. It is similar to the R_X metric introduced by Chiou and Youngs (2008), i.e., the horizontal distance measured perpendicular to the fault strike from the top edge of rupture plane, and used essentially to discriminate between the hanging ($R_X > 0$) and footwall ($R_X < 0$) of the fault. At variance with R_X , R_{line} is always positive, and it is introduced because it only requires the identification of the top edge of the fault, generally better constrained than either the dip angle or the bottom edge of the fault, that are the basic geometric parameters to define R_{rup} or R_{JB} . For this reason, R_{line} is easier to be measured in practice, as it is affected by less uncertainties than R_{rup} and R_{JB} , relying on the definition of the complete geometry of the fault plane.

Notice that in Figure 5.2, L_{eff} is the length of the fault, according to its effective dimensions, calculated through the approach suggested in Thingbaijam and Mai (2016). The dependency of these effective measures on magnitude through scaling relationships has been verified (using e.g. Wells and Coppersmith 1994 or Leonard 2010).

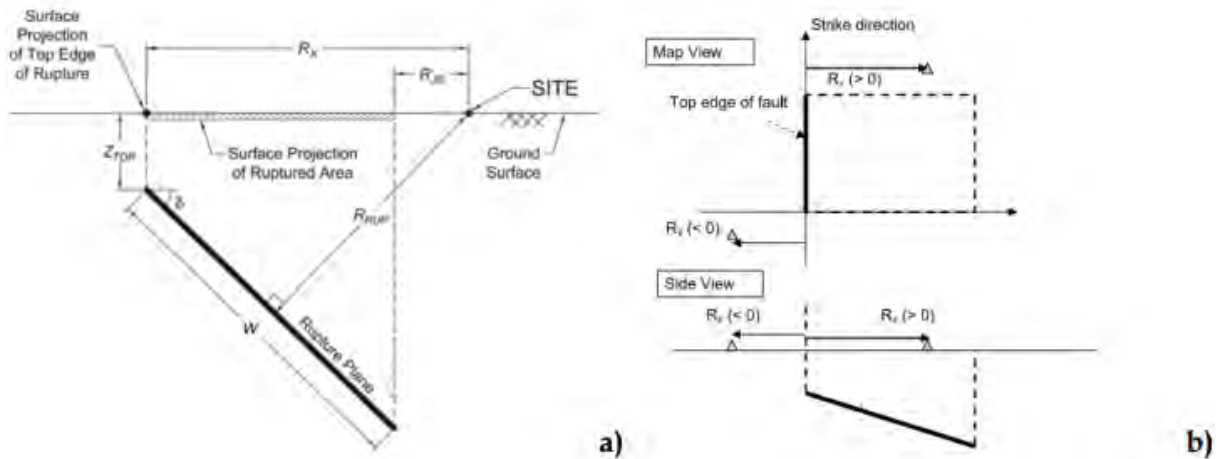


Figure 5.1. a) Representation of the earthquake source and distance measures using a vertical cross section through a fault rupture plane (taken from Kaklamanos et al., 2011). b) map (top) and side (bottom) view of the source-to-site distance measure (R_x) for an example fault (thick black line) plane and stations located on the hanging wall ($R_x > 0$) and footwall ($R_x < 0$) side (taken from Ancheta et al., 2013).

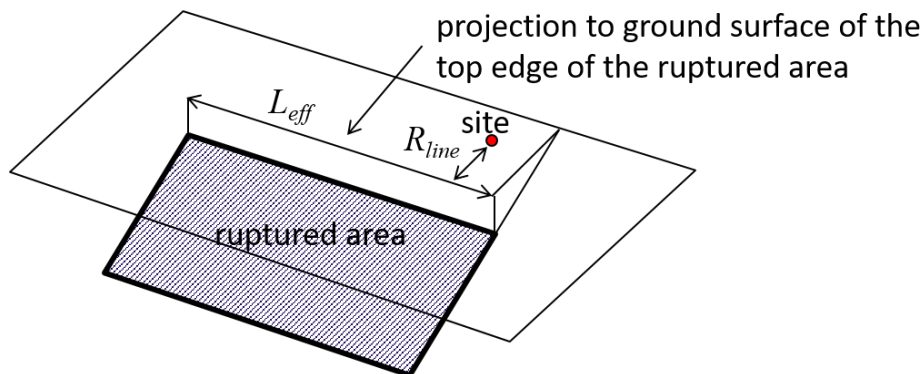


Figure 5.2. Definition of R_{line} distance metric for a specific site, with respect to a certain fault area.

Figure 5.3 shows correlations between the distance metrics calculated for all the selected receivers of the scenarios taken into account; specifically, it shows R_{line} , R_{JB} and R_{hyp} with respect to R_{rup} , taken as reference. Some well-known trends in terms of correlation between distance metrics can be seen (see e.g. Scherbaum et al., 2004), such as that R_{JB} is a lower bound for R_{rup} and that they tend to approach only for $R_{rup} > 40$ km (at least for the selected magnitude range from 6.0 to 6.7), and that, again for the selected magnitude range, a poor correlation between R_{hyp} and R_{rup} is evident. On the opposite, R_{line} shows a closer relation with R_{rup} , that justifies the similar features of the two metrics when processing results.

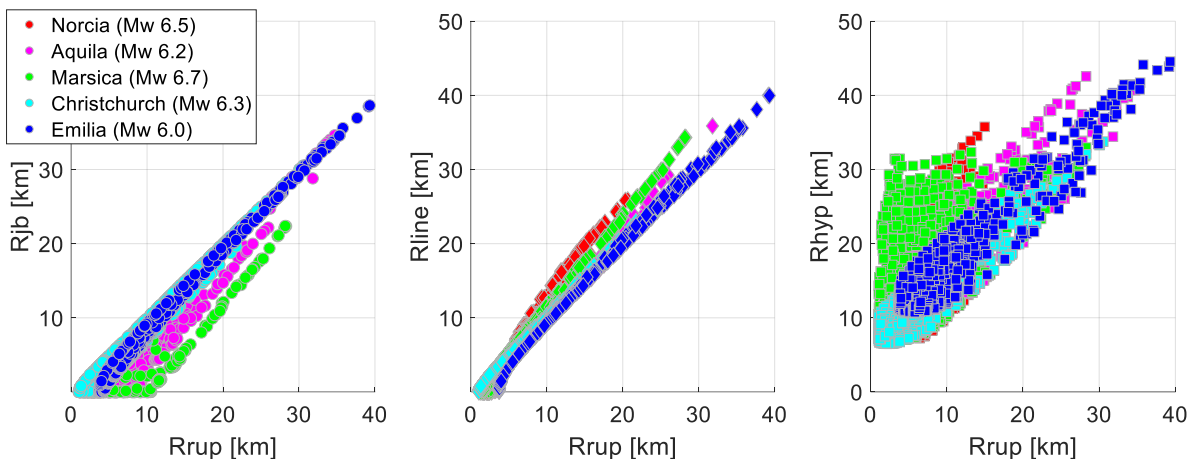


Figure 5.3. Correlation between the investigated distance metrics. R_{JB} , R_{line} and R_{hyp} versus R_{rup} .

Figure 5.4 shows the attenuation of PGV values as a function of R_{hyp} , R_{line} , R_{rup} and R_{JB} for each scenario. Simulations at surface receivers are colored according to their position with respect to the fault: red unfilled circles for HW receivers, blue unfilled circles for FW, red filled circles for in-fault projection receivers. GMPEs predictions are shown as well, using different models, with reference to the distance metric at play. The selected GMPEs are: ITA14 (Bindi et al. 2014), for R_{hyp} plots, ITA18 (Lanzano et al. 2019 for R_{JB} plots, and CZ15 (Cauzzi et al. 2015) for R_{rup} plots. The GMPEs have been computed with respect to both ground type A and the prevailing ground type of the surface receivers of the considered simulation. More specifically, $V_{s,30}=145$ m/s for the Marsica scenario, $V_{s,30} = 300$ m/s for Po Plain and Christchurch, $V_{s,30}=490$ m/s for Norcia and $V_{s,30}=410$ m/s for L'Aquila. The style of faulting of each simulation (shown in Figure 4.3) has been considered as well. For each plot, 16th, 50th and 84th percentiles values (green dots and vertical bars) have been calculated, with reference to different bins of distances. Available observations from NESS data set are shown for all scenarios (except Marsica), showing a general agreement, especially at short distances. Disagreements with Norcia case at distances longer than 10 km are ascribed to softer soil conditions of observations with respect to simulated ones.

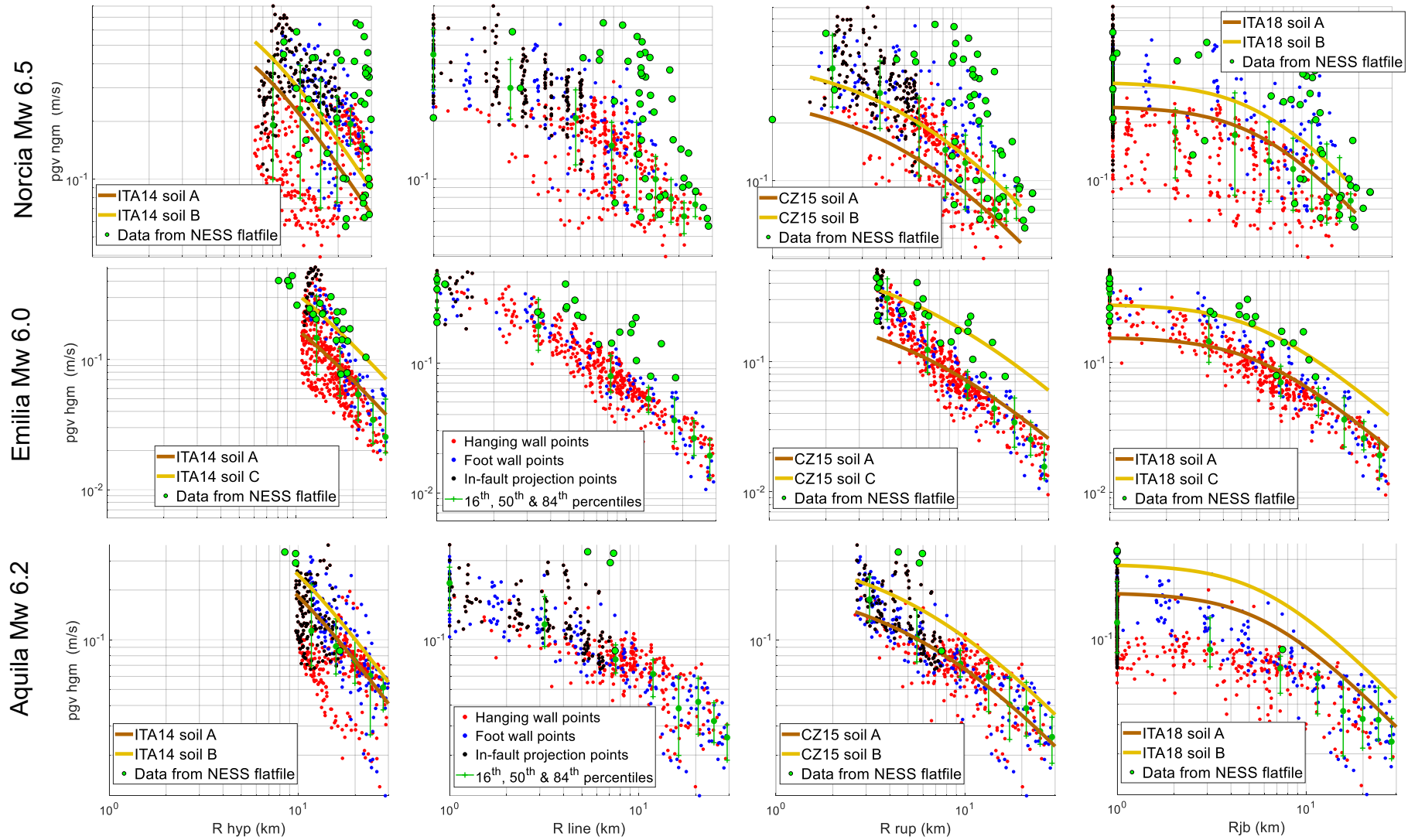
The analysis of these results suggest the following remarks:

- a large scatter is observed at $R_{JB}=0$, as also illustrated by the ground motion maps in the Appendix C, suggesting the large variability of ground motion throughout the surface projection of the fault. Such scatter increases for larger magnitude earthquakes, since the fault size increases. Furthermore, as a consequence of this spread, median values at $R_{JB}=0$ tend to decrease, as compared to those obtained by either R_{line} or R_{rup} ;
- similar to R_{JB} , R_{hyp} shows a large variability for low distance values and lower median values, especially for large magnitude events. The attenuation of peak ground motion amplitudes with distance is generally poorly reproduced because the sites of maximum ground motion amplitudes may be far from the epicenter;
- R_{line} and R_{rup} show a similar performance at very small values, with a significantly reduced spread of results and larger median values with respect to R_{JB} and R_{hyp} . Furthermore, a proper decrease of amplitude with distance is found;
- empirical GM models tend to provide a similar attenuation with distance as PBS, provided the same distance metric is adopted.
- a limited variability can be found for some simulations, such as the Po Plain, with respect to others (such as Norcia), most likely due the specific rupture propagation effects and relatively homogeneous geological conditions;

- footwall positions tend to show higher values of PGV at higher distances, while the opposite is found at short distances.

Note that the same considerations apply to other intensity measures, such as PGA or spectral accelerations at longer periods, not shown here for sake of brevity but shown in the Appendix C.

Finally, it is to be noted that the very large peak values of ground motion for the Christchurch simulation (see Figure 5.4), notably at short distances, are due to super-shear effects together with absence of non-linear soil response. As mentioned previously, these issues will be overcome in the next version of the database.



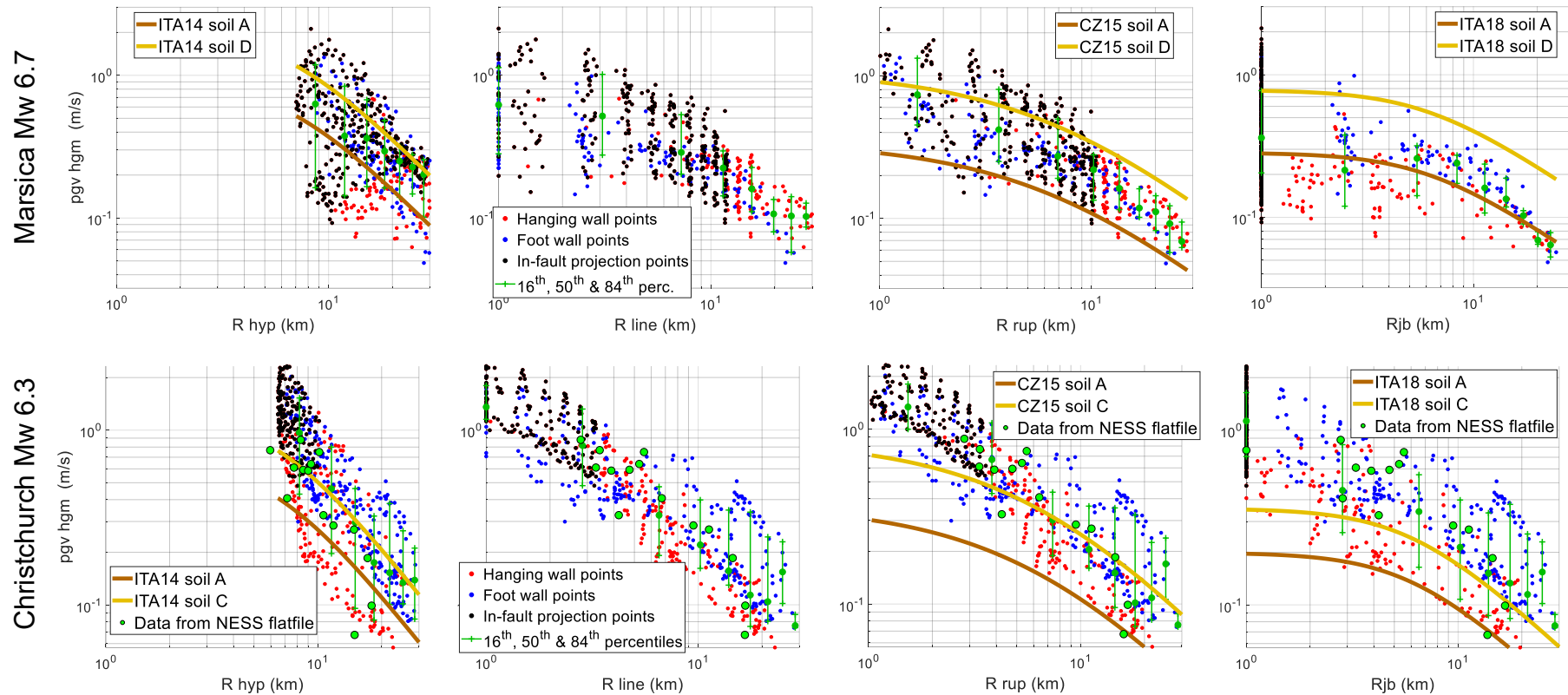


Figure 5.4. PGV values of horizontal ground motion versus different distance metrics: R_{hyp} , R_{line} , R_{rup} and R_{jb} . Data at surface receivers are colored according to position: red unfilled circles for hanging wall receivers, blue unfilled circles for foot wall, red filled circles for in-fault projection receivers. GMPEs predictions for the scenario at play are shown as well: ITA14, for Bindi et al. (2014), ITA18 for Lanzano et al. (2019), CZ15 for Cauzzi et al. (2015). Percentiles of PGV values are shown in green for different bin values.

To better highlight the dependency of the median values and of the dispersion of the data at very short distances, as a function of the distance metrics, Figure 5.5 shows, for each scenario, the median intensity measures (IM_{max} : top) and the standard deviation of the logarithm of the data (σ_{ln0} : bottom) for PGV, PGA and SA(3s), at the lowest distance bin (the “zero” distance one), as a function of the different distance metrics. As noticeable, the lowest values of IM_{max} are systematically related to R_{hyp} or R_{JB} distance, while the highest ones to R_{line} and R_{rup} , owing to the larger spread of results using either R_{hyp} or R_{JB} , as highlighted by the σ_{ln0} values reported in the bottom panel of the same figure.

Figure 5.6 shows the standard deviation of the logarithm of the data (σ_{ln}), at all distance bins, averaged over all scenarios. The highest dispersion is found for R_{hyp} , while other distance measures are comparable. Dispersion tends to be more or less constant for all distances, except for R_{hyp} , for which it decreases with distance.

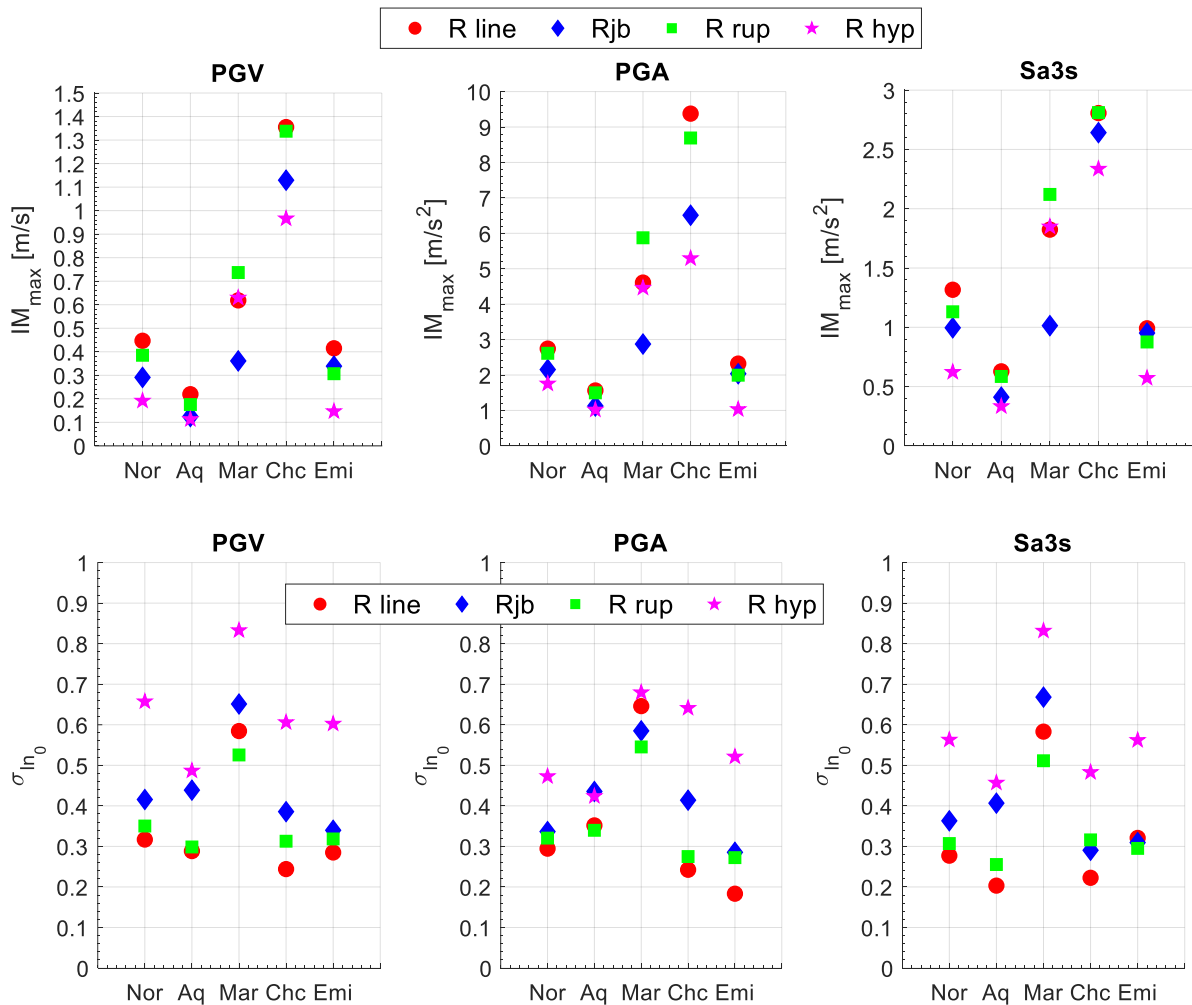


Figure 5.5. Median intensity (*top*) and dispersion measures (*bottom*) at “zero” distance for horizontal geometric mean of peak ground velocity (*left*), acceleration (*middle*), and spectral acceleration at 3 s (*right*), shown per scenario and distance metric: R_{line} (red circles), R_{JB} (blue diamonds), R_{rup} (green squares) and R_{hyp} (pink stars).

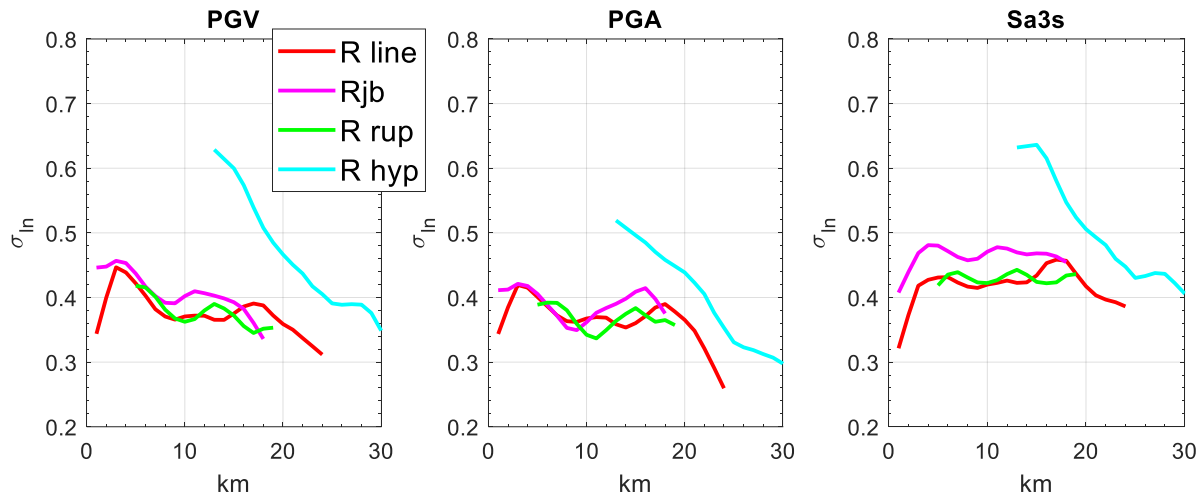


Figure 5.6. Dispersion trends for different distance measures in terms of standard deviation of logarithmic values of different IMs (mean values among different scenarios).

We can conclude from this analysis that, at least for the considered range of magnitude and for dip-slip faults, the choice of the distance metric is critical for accurate predictions in near-fault conditions. The R_{line} and R_{rup} distances might represent, in our concern, the best type of metric, leading to a reduced dispersion and higher median values at distances approaching zero. Furthermore, as noted before, R_{line} is easier to be estimated for practical applications, as it is affected by less uncertainties than R_{rup} .

5.2 A preliminary near-source ground motion model

In this section a preliminary proposal for a near-source ground motion (GM) model is introduced. The objective is to keep the functional form of the model as simple as possible, and the number of parameters as small as possible, in order for the main factors affecting the ground motion in near-source to be properly highlighted. The background for such a model is that a measure of the intensity of ground motion (IM_{max}), expressed for example in terms of its median value, be defined at the ideal “zero” distance, and that a simple attenuation model be introduced for such IM in terms of a normalized distance metric.

Based on these considerations, the suggested near-source GM model is then defined according to the following simple functional form:

$$\frac{IM}{IM_{max}} = \left(1 + \frac{R_{line}}{L_{eff}} \right)^{-\alpha} \quad (5.1)$$

where IM_{max} is shown in Figure 5.5 for the considered scenarios and for the selected IMs, i.e., the geometric mean of PGA, PGV and Sa(3s), L_{eff} is the effective length of the fault (shown in Figure 5.2) and the parameter α governs the decay of IM with distance. The selection of R_{line} is based on the considerations from the previous section, but it could be replaced by other distance metrics.

Figure 5.7 shows such normalized IMs as a function of R_{line}/L_{eff} . The analytical form of the regression model of Eq. 5.1 is shown as well, for each IM. Red and blue lines distinguish the prevailing soil conditions of the receivers (“inside” or “outside” basin) used for interpolations. Regressions have been performed at distances up to a value of R_{line}/L_{eff} less than 0.5. Note that for some scenarios (e.g. Christchurch or L’Aquila) larger ground motions are visible at longer distances ($R_{line}/L_{eff} > 0.5$); in our opinion, these values are mainly be related to directivity and/or radiation pattern.

Figure 5.8 shows, for each analyzed scenario, the parameters (IM_{max} and α) of the attenuation model of Eq. (5.1), as a function of the IM component of motion; that is: horizontal geometric mean (HGM), vertical component (UD), fault normal component (FN); fault parallel component (FP). The standard deviation (σ_{in}) of the fitting model is show as well. In the same figures, square symbols identify results associated to prevailing soil conditions (inside basin), circles identify results obtained with prevailing rock conditions (outside basin ones). Similar values for α may be identified (around 3-4), but further analysis and scenarios are needed for a better understanding. Note that the parameter α in Eq. (5.1) is not modelling a geometrical attenuation with distance, so values greater than one are expected. The dispersion σ_{in} of the attenuation model is found to be around 0.4 for all IMs and scenarios. It is observed that the σ_{in} resulting from our analyses is lower than the intra-event variability of empirical GMPEs (generally about 0.5 to 0.7) because our dispersion measure is related to a single earthquake scenario. As a matter of fact, for that specific scenario, the simulation refers to a common geological context with the same site conditions and outcropping bedrock as well as the same realization of fault rupture. A thorough understanding of the components of ground motion variability at play may be better constrained when a higher number of scenarios will be processed to properly compute the inter- and intra-event variabilities.

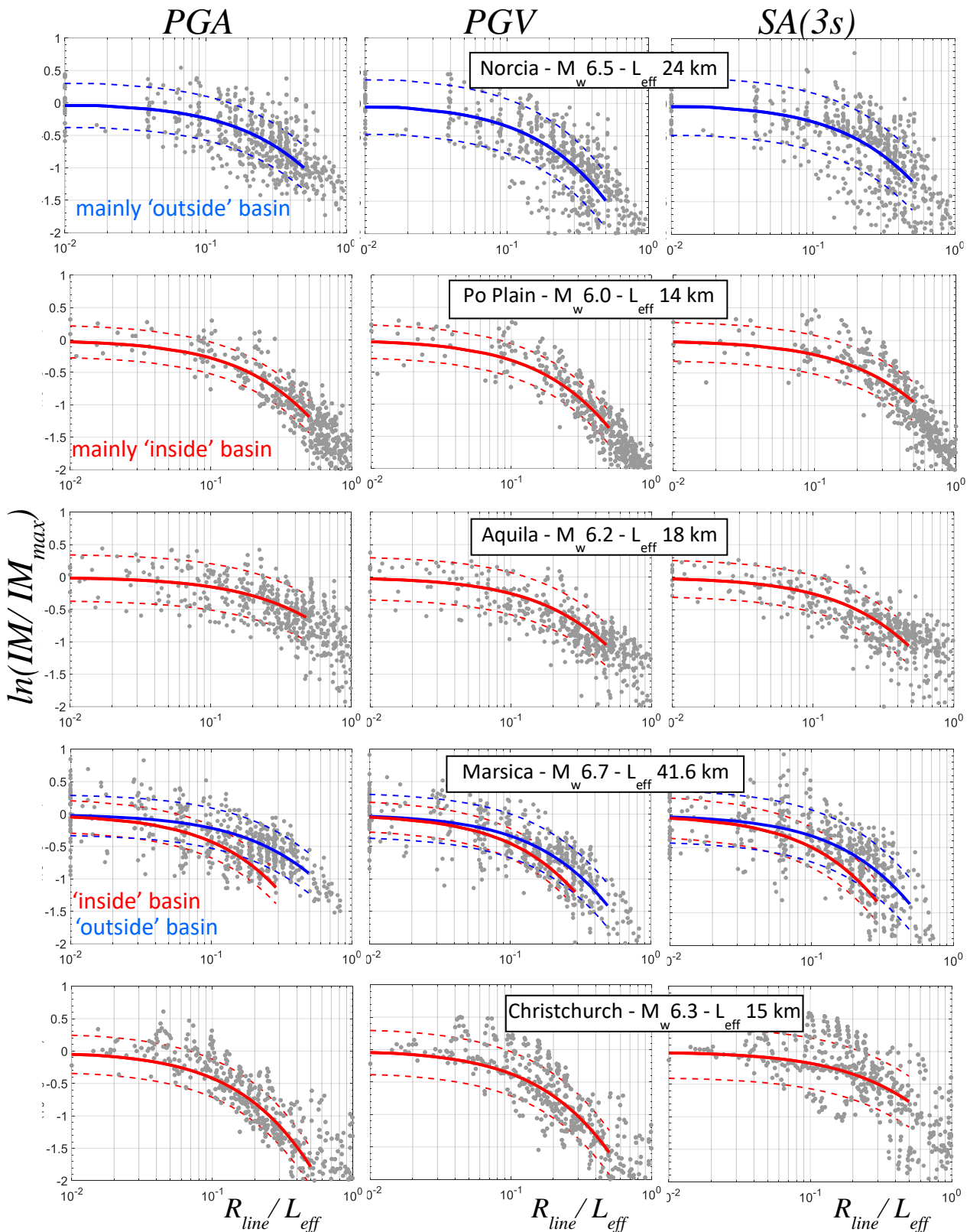


Figure 5.7. Geometric mean of PGA, PGV and $Sa(3s)$ as a function of R_{line}/L_{eff} . IM are normalized to IM_{max} , as explained in the text. The interpolation model of Eq. (5.1) is shown as well, for each IM. Red and blue lines distinguish the prevailing soil conditions of the receivers used for interpolations. Receiver data are shown by grey dots, without distinction of soil conditions.

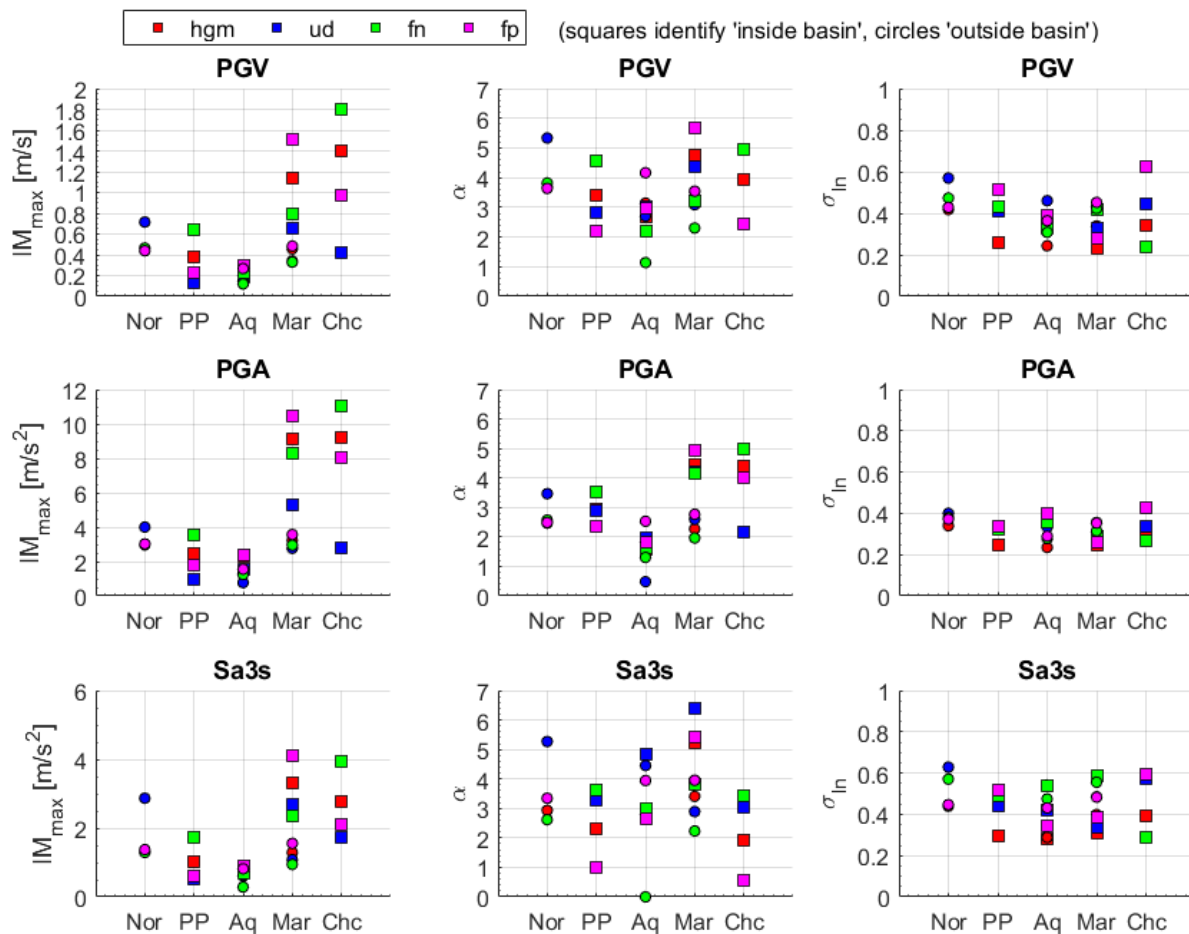


Figure 5.8. Parameters (IM_{max} and α) and standard deviation (σ_{in}) of the interpolation model of Eq. (5.1) as a function of the component type of the intensity measure (HGM: horizontal geometric mean, ud: vertical component, fn: fault normal; fp: fault parallel) and of the simulated scenario.

Based on these results, the following remarks can be made:

- the introduction of a simple functional form of the GM model and its dependence on a normalized distance metric provides a relatively stable picture of the attenuation of motion, with similar features for different scenarios and with a relatively mild dependence on site conditions;
- this suggests that an even simpler form of near-source GM could be introduced, where the only explicit dependence on magnitude and site conditions may be summarized in the parameter IM_{max} , and a single value of the decay parameter α be introduced.
- an investigation of the effect of different distance metrics may be useful to determine which metric is capable of reducing the spread of results.
- introduction of further scenarios in the dataset, particularly with the extension to larger and smaller magnitudes than the range from 6 to 6.7 considered so far, may be suitable to support these preliminary remarks.

5.3 Directionality: FN/FP

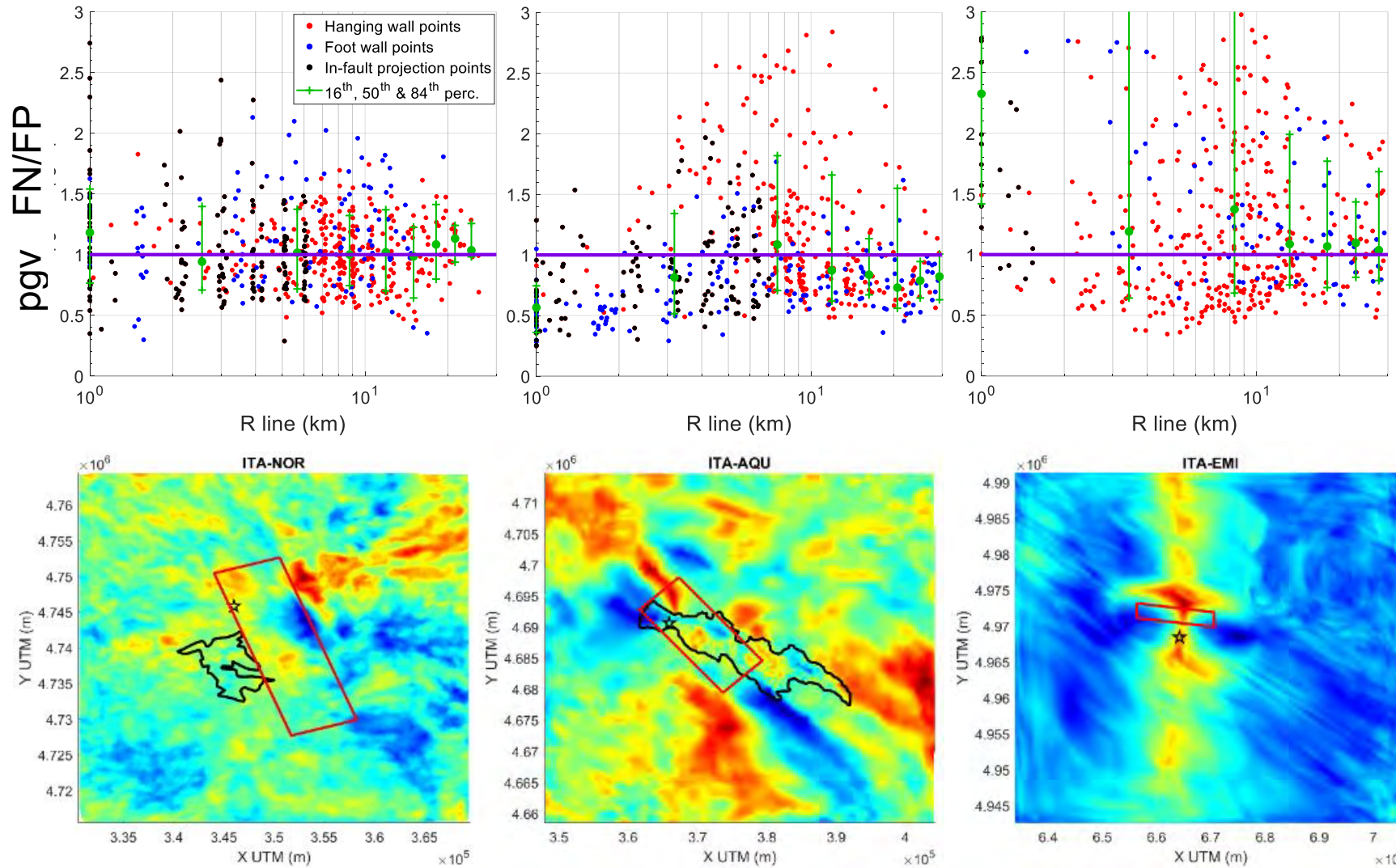
This section and the following ones address some specific features for near-source GM characterization that may be further exploited in view of a more comprehensive near-source model. In this section we will illustrate the GM polarization that may result in large values of the ratio of the FN vs FP horizontal components, while the vertical-to-horizontal ratio and the identification of pulse motions will be addressed in the following sections, respectively.

Figure 5.9 shows FN/FP ratios of PGV as a function of R_{line} , for different scenarios, with the corresponding maps. It is difficult to clearly identify patterns. The single cases where the FN/FP ratio at short distances tends to be significantly higher than 1 seems to correspond to up-dip directivity conditions in the two reverse fault scenarios, i.e., Po Plain and Christchurch. As it will also be shown later, these are also conditions for identification of pulse signals with period T_p in the range between 1s and 3 s. In the Marsica scenario, there is instead a clear dominance of the FP component, plausibly related to the interaction with the very soft basin conditions of the Fucino plain, leading to onset of surface waves travelling in the longitudinal direction of the basin. The Norcia and L'Aquila scenarios provide instead relatively neutral polarization conditions, with FN/FP ratios on average equal to 1.

Norcia (Mw 6.5)

Aquila (Mw 6.2)

PoPlain (Mw 6.0)



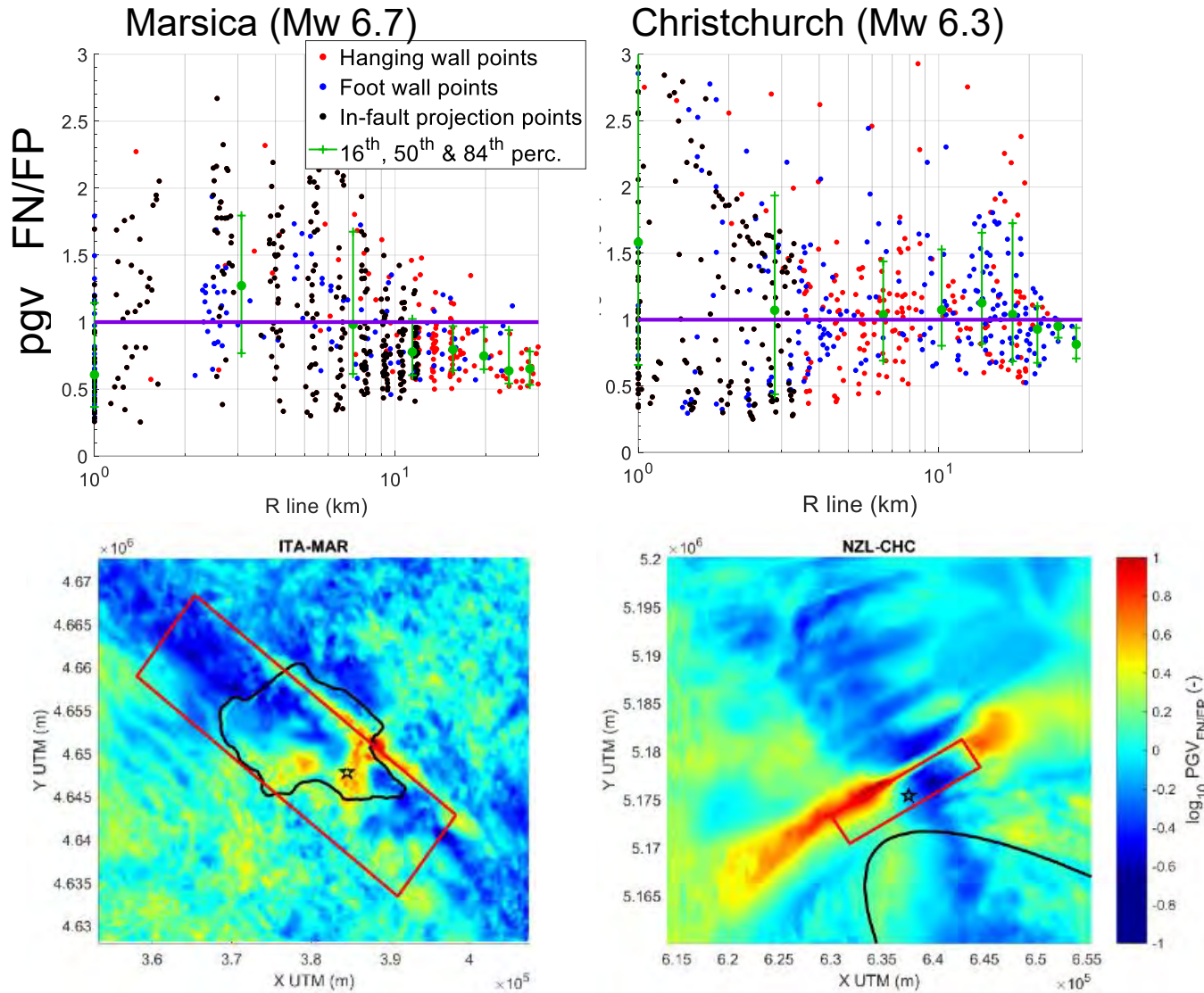


Figure 5.9. Top: Fault normal over fault parallel PGV ratios as a function of R_{line} , for different scenarios. Data at surface receivers are colored according to their position: red unfilled circles for hanging wall receivers, blue unfilled circles for foot wall, red filled circles for in-fault projection receivers. Percentiles values calculated per distance bin are shown as well in dark green. Bottom: maps of the corresponding FN/FP PGV ratios

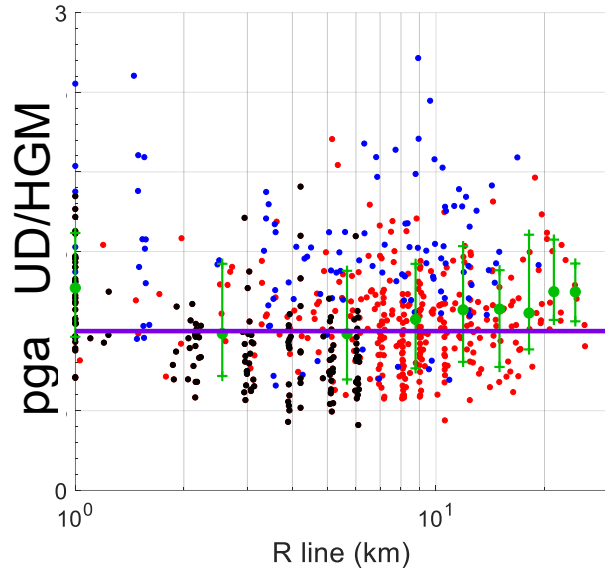
5.4 Vertical-to-Horizontal Ratios

Large vertical ground motion, especially at short periods, may characterize near source records, notably when up-dip rupture propagation effects play an important role. For this reason its ratio with respect to horizontal geometric mean has been analyzed, for each IM. Figure 5.10 shows V/H ratios for PGA (where H is the horizontal geometric mean). The corresponding ratios are also shown in the Appendix C for PGV and Sa(3s).

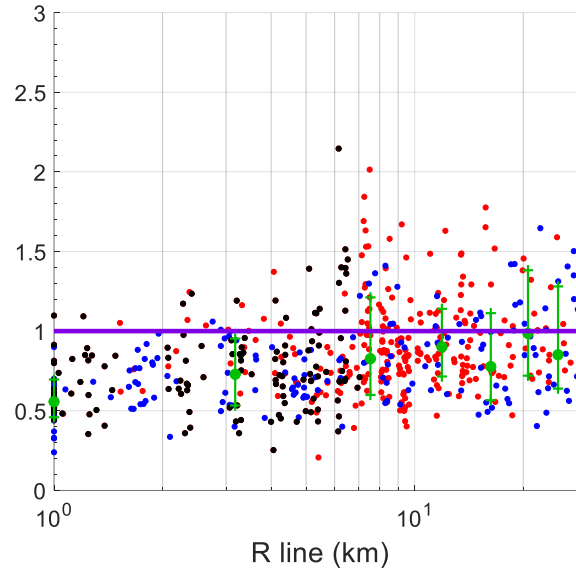
The observed trend is towards low V/H ratios (around 0.5) for all those scenarios where basin or soft-soil conditions are prevalent, i.e., all scenarios with the Norcia exception. As a matter of fact, such soft conditions provide prevailing amplification of the H components implying the lowering of the V/H ratio.

The Norcia map, where basin conditions are present only within the basin delimited by the black line, suggests the interesting result that large V/H ratios are found especially in the fault normal direction at R_{line} close to 0 and on the footwall side of the fault. This spatial pattern of V/H ratios can be ascribed to up-dip rupture propagation effects and it is in general agreement with the recordings (as shown in Figure 5.11), with large VH ratios especially at R_{line} tending to 0, NE of the epicenter (see CNE, CLO and T1244 stations). The influence of up-dip rupture propagation on large V/H ratios can be also found from the other maps (see e.g. L'Aquila), where larger VH ratios are typically found especially in the regions along the fault slip direction, both on HW and FW side, off the surface fault projection and basin area, but at larger distances.

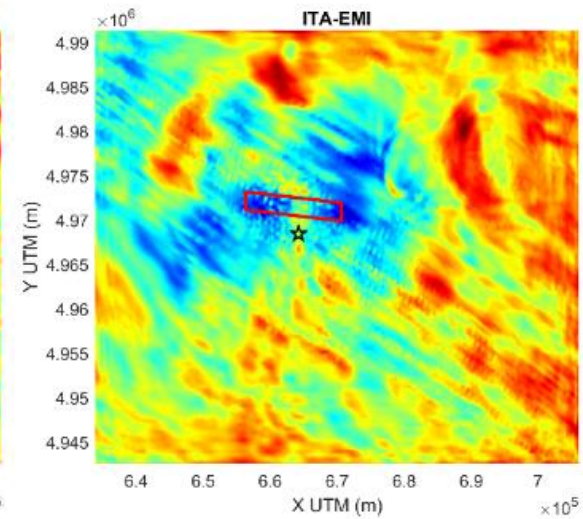
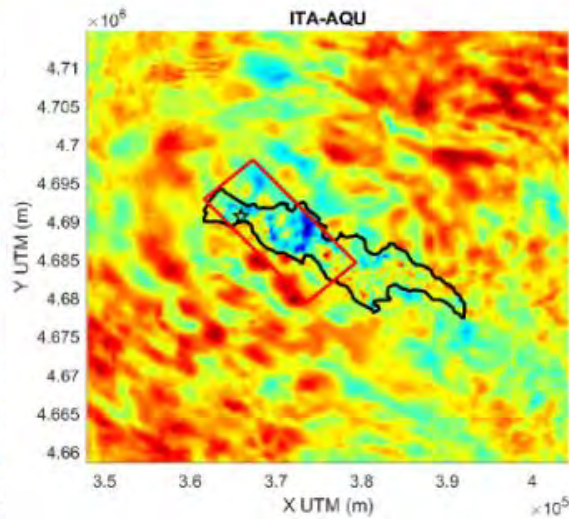
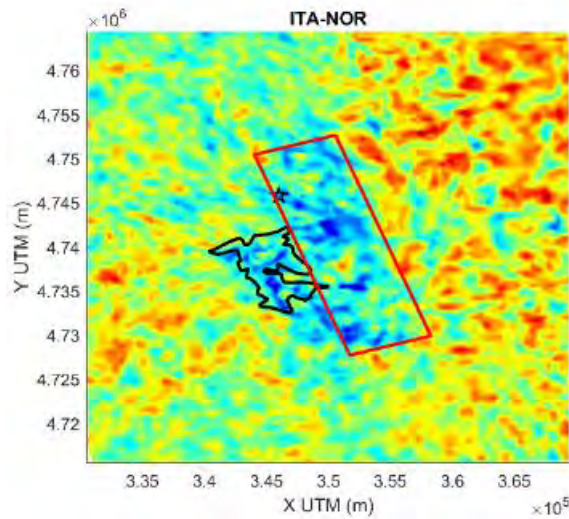
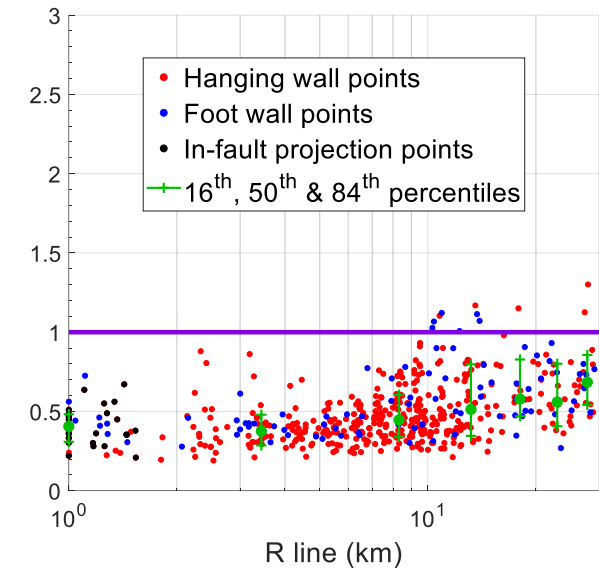
Norcia (Mw 6.5)



Aquila (Mw 6.2)



PoPlain (Mw)



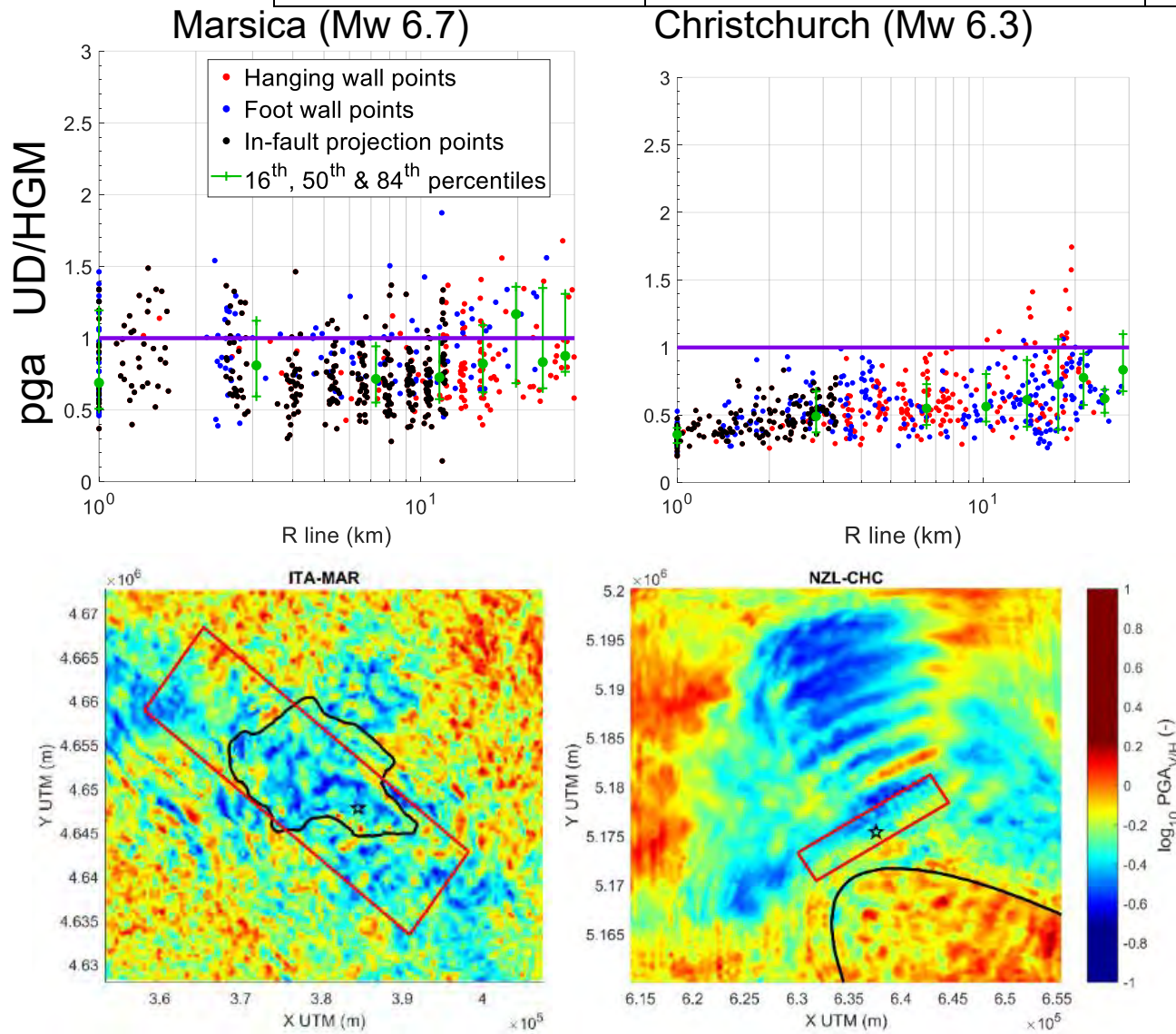


Figure 5.10. Top: vertical-to-horizontal geometric mean of PGA ratios as a function of R_{line} , for different scenarios. Bottom: Maps of the corresponding V/H ratios

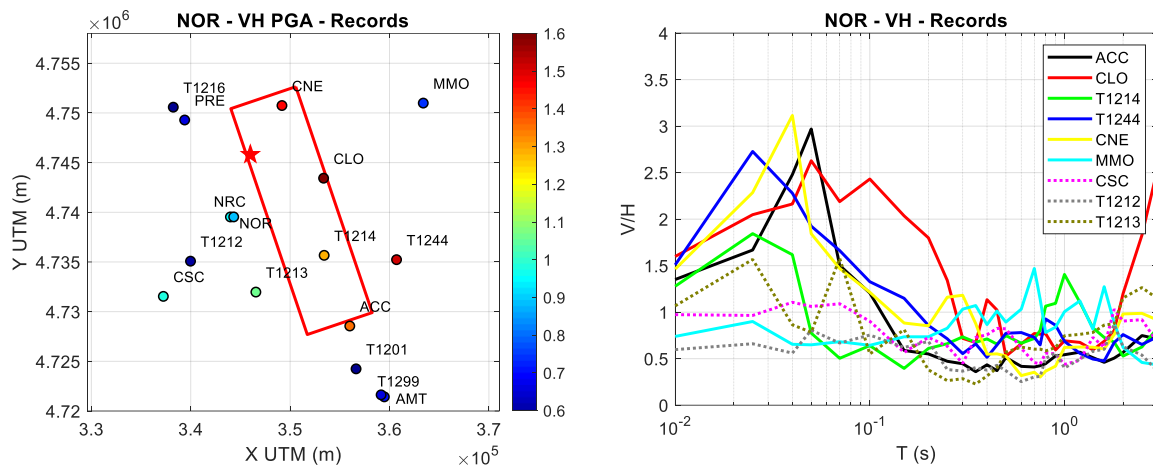


Figure 5.11. Left: Map of V/H ratios for PGA at the stations which recorded the 2016 Norcia earthquake. Right: V/H spectra for selected stations.

5.5 Pulse periods

In this section the attention is devoted to the identification of pulse signals within the simulation results, together with the corresponding period T_p , tagged and stored in the flatfile table for each selected receiver.

The identification of pulse-like waveforms and of T_p has been done relying on the algorithm proposed by Shahi and Baker (2014). Figure 5.12 shows T_p values as a function of R_{line} , for all processed scenarios. T_p shows values from 1 to 7 s, with amplitudes tending to increase with magnitude (Baker 2007; Mavroeidis and Papageorgiou, 2003, Shahi and Baker 2011). Further investigations have to be performed, in order to understand what are the conditions leading to the largest values of T_p , probably related to coupling with deep basin conditions; indeed, calculated T_p values are in reasonable agreement, within comparable magnitude ranges, with observations, as shown in Figure 5.13, where T_p is plotted versus magnitude, for BB-SPEED and NESS datasets. Notice that for some PBS (like Po Plain and Marsica) site amplification affects results, remarkably at long periods, increasing T_p estimates with respect to observations.

Neglecting for the moment pulses with $T_p > 3s$, it is worth to note that an interesting correlation is found between fault normal peak values and the presence of pulse-like motions with T_p in the range 1-3 s (enveloped in the blue rectangle of Figure 5.12). Figure 5.14 shows maps of the presence of pulse-like signals for three processed scenarios (Norcia, Emilia and Aquila), compared to the corresponding FN PGV maps. As noticeable, the pulse maps highlight areas in good agreement with those presenting peaks of the FN component of velocity, typically close the top edge of the fault, where R_{line} takes its lowest values. Similar features are also found in the Marsica and Christchurch scenarios, not shown for brevity.

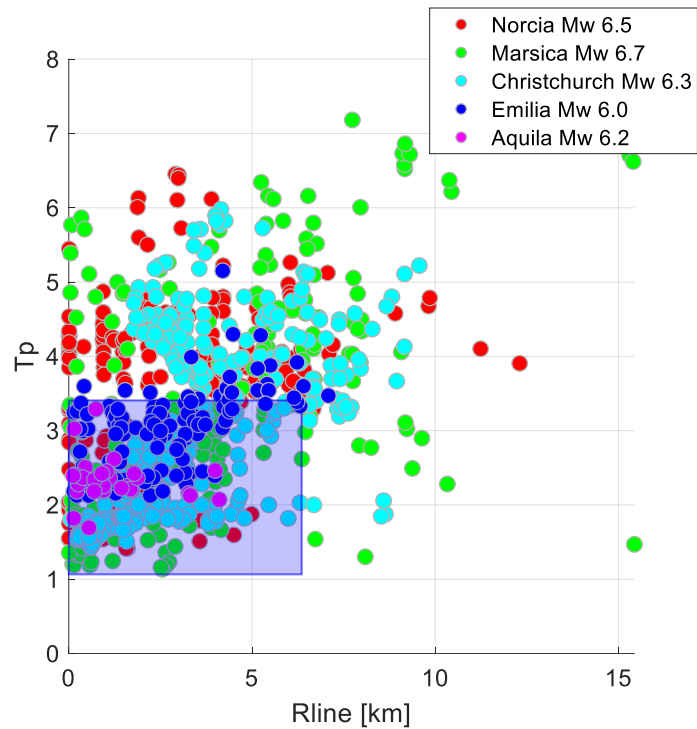


Figure 5.12. Pulse period T_p versus R_{line} distance, for each scenario. The blue rectangle identifies the ranges of T_p values used in subsequent Figure 5.14.

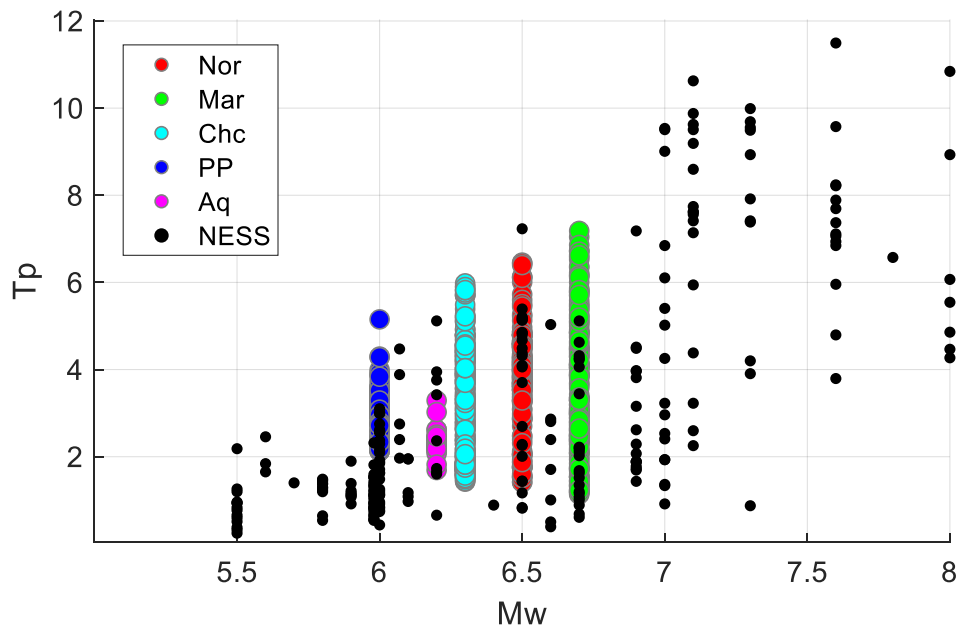


Figure 5.13. Pulse period T_p versus earthquake magnitude for observed pulse-like ground motions of BB-SPEEDset (colored dots) and NESS dataset (black dots).

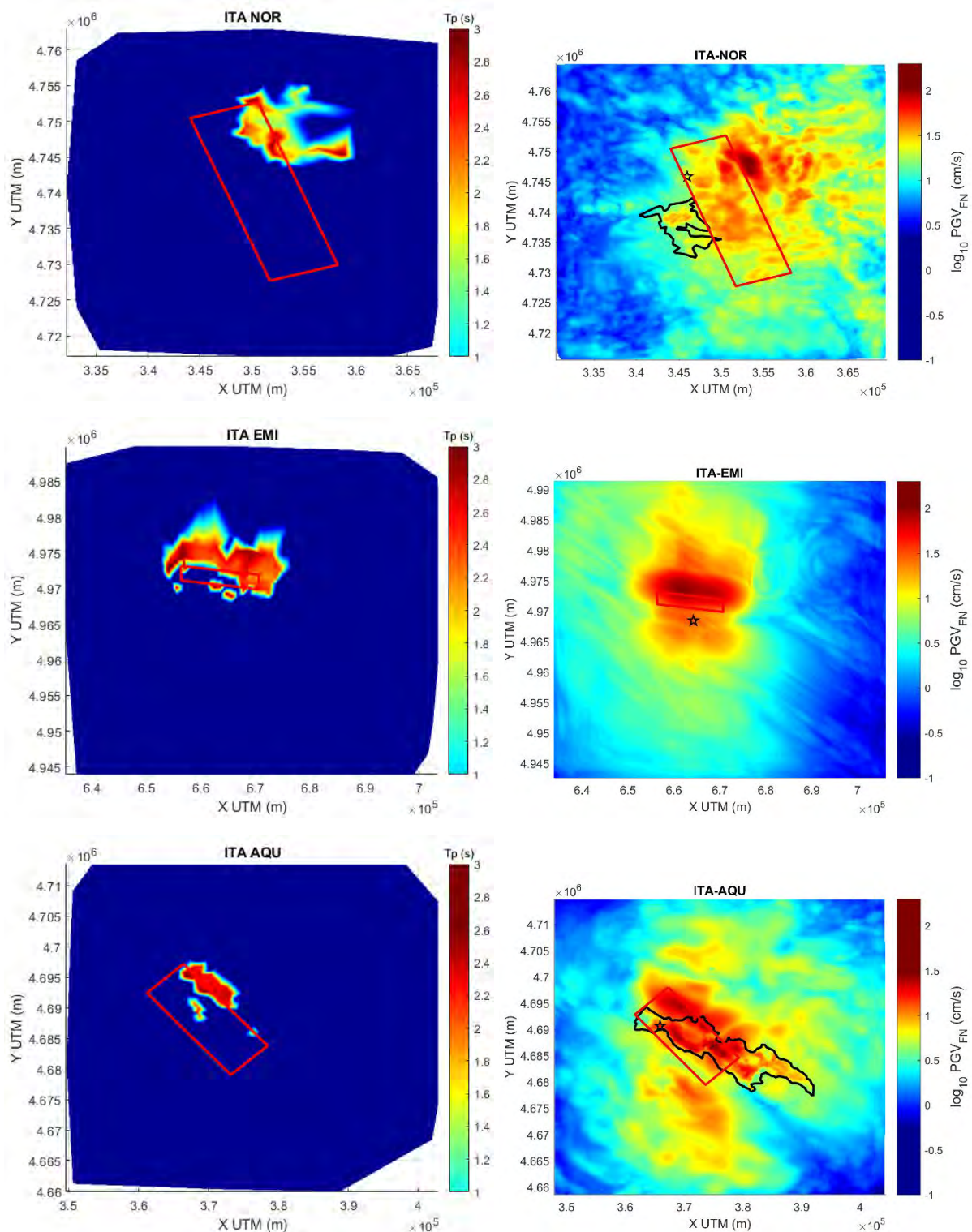


Figure 5.14. Left: maps of pulse period T_p for Norcia, Mw 6.6, (top), Emilia, Mw 6.0, (center) and Aquila, Mw 6.2 (bottom). Right: FN PGV maps (in \log_{10} scale) for the same scenarios.

Further investigations on the period pulse T_p are shown in Figure 5.15, where results from BB-SPEEDset and NESS, on the left and right-hand side of the figure, respectively, are compared in terms of the R. Paolucci et al. - Construction of a near-source broadband earthquake ground motion dataset from 3D physics-based numerical simulations - SIGMA2-2020-D3-051

variability of T_p with respect to PGD/PGV. The figure on the right side, with results for NESS dataset is taken from DPC – RELUIS, 2018.

In the left of the figure, a blue triangle envelopes the set of T_p values within the BB-SPEEDset, while in the right the same blue triangle is overlapped to the NESS values. A reasonably good agreement between the two sets is found, within comparable magnitude ranges (i.e., M_w from 6.0 to 6.7). NESS displays in fact even lower (or higher) values of T_p , related to events with respectively lower (<6.0) or higher (>6.5-7.0) magnitudes. Note that the pulse identification procedure used in the BB-SPEED and NESS datasets is not exactly the same, as NESS uses a slightly modified procedure from Shahi and Baker (2014)⁷.

Tentative correlations between T_p and PGD/PGV ratios are shown as well in Figure 5.15, with thick red dashed lines, as a function of the pulse type function associate to simulated ground motion. Considering a velocity pulse of the “Ricker wavelet” type, with peak of the Fourier spectrum at $f_p=1/T_p$, it can be easily found that the analytical relationship between T_p and PGV/PGD is as given in the top-left of Figure 5.15, while, considering a “double-impulse” type, the relationship is as given in the center-left of Figure 5.15⁸. Examples from processed simulations of the BB_SPEED set (within the ranges of periods and peak ratios identified by the orange circles) allowed verification of these simple findings.

It is also interesting to notice that the analytical correlation derived for the “Ricker wave type” velocity pulses perfectly fits the average line of the NESS dataset, on the right picture, suggesting that most pulses identified within NESS are of the Ricker wavelet type.

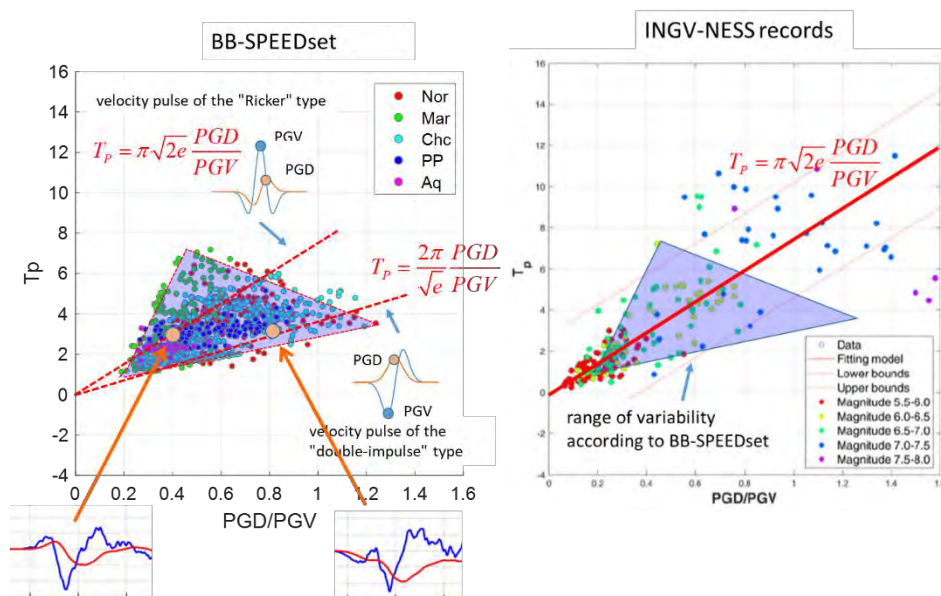


Figure 5.15. Pulse period T_p as a function of PGD/PGV for the BB-SPEED dataset (*left*) and for the NESS dataset (*right*, after DPC – RELUIS, 2018), together with analytical relationships for Ricker wavelet and double-impulse functions. Examples of time histories from the BB-SPEEDset are also shown, on the bottom, for comparison with the analytical ones.

⁷ Further details can be found here: [http://itaca.mi.ingv.it/itacaNet_31/#/documents/pulse like identification](http://itaca.mi.ingv.it/itacaNet_31/#/documents/pulse%20like%20identification)

⁸ The Ricker wavelet velocity is defined as $v(t) = (1 - 2\alpha^2 t^2) e^{-\alpha^2 t^2}$, with $\alpha = \pi f_p$. The double-impulse velocity is defined as $v(t) = 2\pi f_p \sqrt{e} t e^{-\alpha^2 t^2}$, with $\alpha = \sqrt{2}\pi f_p$. Both pulses have unit peak amplitude.

Further analyses on the variability of T_p will be performed in the future, using different peak ratios, as shown in Figure 5.16, where T_p is plotted as a function of PGV/PGA and $PGA*PGD/PGV^2$. The distribution functions of the tested peak ratios (PGD/PGV , PGV/PGA , $PGA*PGD/PGV^2$) have been analyzed in Figure 5.17, comparing values among signals identified as 'impulsive' or 'non-impulsive' within the whole BB-SPEEDset and within the NESS set (at comparable magnitudes). Fitted lognormal probability functions are shown as well. Note that there is an overall agreement between the two dataset, despite the fact that peak ratios from NESS tend to be slightly lower since data were selectively high-pass filtered after visual inspection. Notably, PGV/PGA ratios tend to be higher for impulsive signals in both datasets, while the opposite occurs for the other peak ratios.

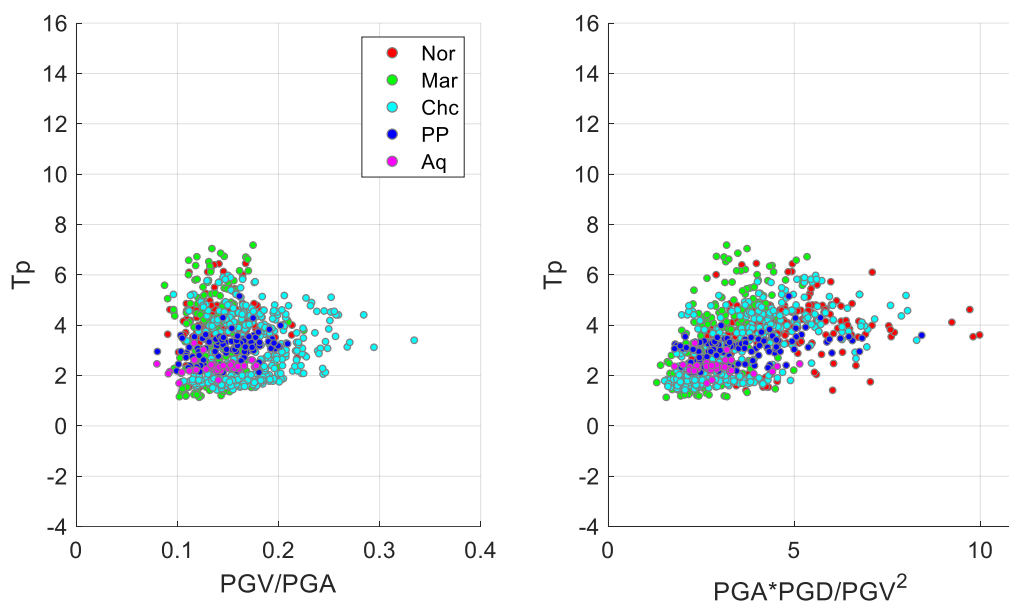


Figure 5.16. Pulse period T_p as a function of PVD/PGA (*left*) and $PGA*PGD/PGV^2$ (*right*) for the BB-SPEED dataset.

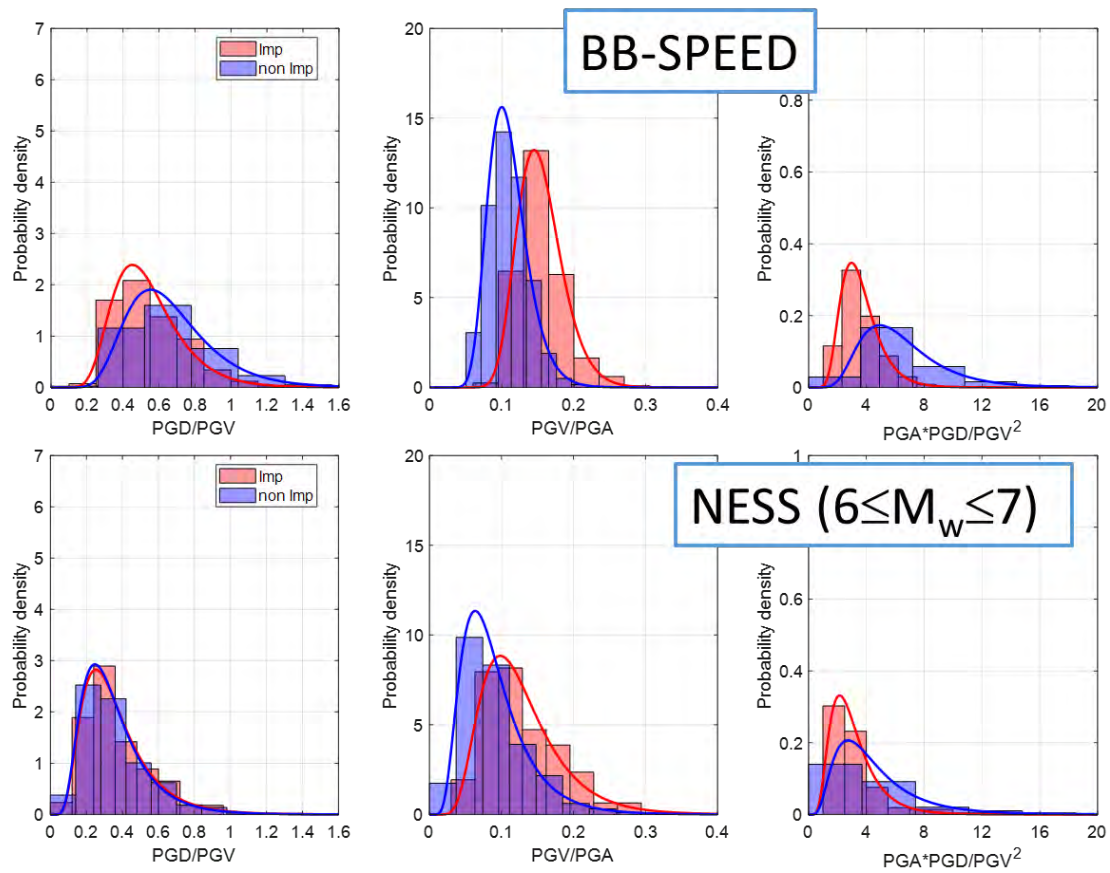


Figure 5.17. Probability density functions of different peak ratios, for 'impulsive' and 'non-impulsive' identified signals, for the whole BB-SPEEDset (*top*) and for the NESS dataset at comparable magnitudes, i.e. $6 \leq M_w \leq 7$ (*bottom*). Fitted lognormal pdf functions are shown as well by continuous lines for both type of signals.

6. Conclusions and future developments

Within the Task C of SIGMA2 Project, the research activity of Politecnico di Milano aimed at constructing a near-source broadband earthquake ground motion dataset from 3D physics-based numerical simulations (PBS) obtained by the computer code SPEED. The ultimate goal of this research, which is still on-going, is to assemble and post-process PBS of different real and realistic worldwide earthquakes in a homogeneous format and produce a flatfile of synthetic ground motions in near-source conditions. This flatfile can be used, as a complementary tool of empirical databases (e.g. the near-source strong motion database NESS, Pacor et al. 2018), to produce a Ground Motion Model (GMM) and investigate systematically some features of near-source earthquake ground motions. These include a variety of aspects, ranging from the attenuation of peak amplitudes with distance, radiation pattern and directivity effects, pulse-like motions, vertical-to-horizontal ratios, spatial correlation, coupling of near-source effects with surface geology, etc., which can be hardly explored from records because of their limited number.

In this Deliverable, we have documented in detail the steps which are preparatory to the construction of this database, referred to as BB-SPEEDset, and then presented an overview of the preliminary results obtained from a selection of five PBS to give insights into some of the aforementioned key features of near-source ground motion. For this reason, the results included in this Deliverable shall be considered as preliminary and further work will be carried out in the next year of the Project to include further PBS

in BB-SPEEDset and to extend the analyses to a wider and more representative set of ground motions in terms of seismo-tectonic context, geological conditions and magnitude range.

Optimized workflow for SPEED broadband processing and flatfile generation

An effective workflow has been devised and implemented in Matlab to post-process PBS results from SPEED in a homogeneous and repeatable format (see Figure 2.1). The core of the workflow is the generation of broadband ground shaking maps and waveforms starting from PBS results according to the ANN2BB procedure first proposed in Paolucci et al. (2018) and improved in this project.

The workflow includes a set of tools executable in a semi-automatic way starting from raw SPEED results which allow one to:

- generate broadband ground shaking maps following the ANN2BB approach for SA at different periods;
- compute a representative set of site response proxies, such as (but not only) V_{s30} and depth to the geologic bedrock, which are helpful to explore the correlation of ground motions with surface geology features;
- compute the effective fault dimensions, consistent with the magnitude scaling relationships, according to the approach proposed by Mai and Beroza (2000) and extended by Thingbaijam and Mai (2016): this is a fundamental step to avoid bias in the computation of distance metrics within the development of a near-source ground motion model (regardless of its synthetic or empirical nature);
- generate broadband waveforms starting from raw SPEED time histories according to the ANN2BB approach, for an arbitrary set of receivers selected according to prescribed criteria (e.g. higher density at very short distances, on the fault plane). A revised ANN2BB procedure was devised to improve the quality of waveforms and make it suitable for massive post-processing of PBSs in a semi-automatic fashion with no manual interventions;
- prepare for each PBS “ID cards” containing all relevant information regarding both input and output data;
- produce for each PBS a flatfile including all relevant metadata regarding the source, post-processing, station, site-to-source distances and several IMs including not only response spectral ordinates but also integral parameters (CAV, Arias Intensity, duration, pulse period, etc..).

The fields of the flatfile (Table 4.1) are defined in such a way to be as much as possible consistent with the NESS database, since a direct comparison between synthetics and recordings is considered as a fundamental step of this work.

BB-SPEEDset_V0

A first “beta” version of the database of PBS, referred to as BB-SPEEDset, was created by processing five different scenarios with magnitude M_w in the range 6.0-6.7 and source-to-site distances in the range 0-40 km (see Table 3.1 and Figure 4.3). It is worth noting the optimum coverage at very short distances that can be achieved with synthetic ground motion simulations. The first PBS included in BB-SPEEDset correspond mainly to the simulation of real earthquakes (2012 Po Plain; 2009 L’Aquila; 2011 Christchurch; 1915 Marsica; 2016 Norcia), for which extensive validation studies against recordings were already accomplished.

An overview of the processed scenarios is provided in the Deliverable in terms of both ground shaking maps of ground motion IMs, namely, PGA, PGV, SA(3s), and synthetic waveforms (see e.g. Figure 3.1 to Figure 3.3), pointing out the capability of the ANN2BB approach to generate realistic waveforms and reproduce the spatial variability of ground motion and its correlation with surface geology.

From the statistical analysis of the distribution function of RotD100 PGA and PGV, it was possible to extract “extreme” PGAs and PGVs, defined as those with probability of exceedance less than 5% within the scenario, and to illustrate their dependence on distance and magnitude (Figure 4.4). Remarkably,

the amplitude of extreme values, within comparable ranges of magnitude and distance, is consistent with that found on the whole NESS database (which shows actually a poor dependence on M_w and distance).

Preliminary results on near-source features and a GMM from PBS

The analysis of the BB-SPEEDset, carried out at this stage separately for each PBS, allowed us to make the following remarks in relation to the characterization of near-source ground motions.

Effect of different source-to-site distance metrics

- Current empirical GM models tend to provide a similar attenuation with distance as simulations, provided the same distance metric is adopted;
- the choice of the distance metric is crucial for accurate predictions in near-fault conditions, at least for the considered range of magnitude and style of faulting (dip-slip), see Figure 5.4. Among the different distance metrics investigated, R_{line} and R_{rup} turn out to be the best distance metrics leading to a reduced dispersion and higher median values at distances approaching zero, assuming these larger values to be more representative of near-source conditions. On the other hand, R_{JB} and R_{hyp} show systematically a large scatter and lower median values, especially for large magnitude events, and describe poorly the decrease of motion with distance;
- Although with similar features as R_{rup} , R_{line} appears as an interesting distance metric for practical applications, as it is easier to be measured (only the top edge of the fault is needed) and, thus, it is affected by less uncertainties than R_{rup} .

Insights into a near-source GMM calibrated on PBS

- A simple functional form is suggested (see Eq 5.1) providing median IM, normalized with respect to the IM at “zero” distance (IM_{max}), as a function of a normalized distance metric (i.e., R_{line}/L_{eff}) and a decay parameter α . The calibration of such a functional form on the scenarios of BB-SPEEDset suggests that normalization of the distance metric by the effective fault length may be a rational option to construct a simple near-source GMM (Figure 5.7);
- The decay parameter α turns out to be similar in the different cases, suggesting that dependence on magnitude and site conditions may be summarized in the parameter IM_{max} (Figure 5.8). A similar dispersion is also found for the different scenarios.

Near-source features: FN/FP ratios, vertical-to-horizontal ratios and pulse period

- There is a tendency for the FN/FP ratios at short distances to be significantly higher than 1 when up-dip directivity conditions are met (see Po Plain and Christchurch, reverse fault scenarios). These are also conditions for identification of pulse signals with period T_p in the range between 1s and 3 s. In the Marsica scenario, characterized by very soft basin conditions and the onset of surface waves, there is a clear dominance of the FP component. In the other cases, FN/FP ratios are on average equal to 1, see Figure 5.9;
- The vertical-to-horizontal (HGM) ratios (VH) tend to be larger than 1 at short distances ($R_{line} < 3$ km) in those scenarios dominated by rock conditions; on the other hand, for other scenarios dominated by soft soil conditions, VH ratios tend to be lower than 1 (about 0.5), most likely due to amplification effects on the horizontal ground motion, see Figure 5.10;
- The pulse period (T_p) of pulse-like motions was computed according to Shahi and Baker (2014) and the T_p values from synthetics are in reasonable agreement, within comparable magnitude ranges, with those from NESS database. Interestingly, it was found that the spatial region of T_p values between 1 to 3 s correlates well with the region of maximum FN PGV, which is typically at R_{line} values approaching zero (i.e. above the top edge of the fault), Figure 5.14;

- The variability of T_p values, as a function of the ratio PGD/PGV, is found to be consistent with that obtained from the NESS database for the same range of magnitudes and it can be described tentatively by two linear relationships of PGD/PGV with slopes given by $\pi\sqrt{2e}$ (upper bound) and $2\pi/\sqrt{e}$ (lower bound). These relationships are found by analytical derivations considering either a “Ricker type” velocity waveform (upper bound) or a “double impulse” waveform (lower bound), see Figure 5.15.

Future developments

The following main topics are planned to be addressed for the future developments and finalization of this research:

- Finalization of the BB-SPEEDset dataset including further scenarios, already available from past studies, to sample a wider range of magnitudes, up to Mw7.4 (e.g. Istanbul, Beijing, Sulmona, Thessaloniki), and to support these preliminary findings;
- A systematic comparison between BB-SPEEDset and NESS dataset (herein only outlined) will be completed in terms of attenuation with distance, components of ground motion variability, distribution of ground motion “extreme” values, FN/FP ratios, vertical-to-horizontal ratios, pulse period, fling effects;
- Check the predictive capability of Eq. (5.1) on a larger set of PBS and investigate the dependence on different distance metrics;
- Based on results at previous point, calibration of a near-source GMM based on BB-SPEEDset.
- Publication of the BB-SPEEDset scenarios on a Web Repository accessible to any interested end user: <http://speed.mox.polimi.it/WebRepository/> (a beta version of the Web Repository is already available, as sketched in Figure 6.1).

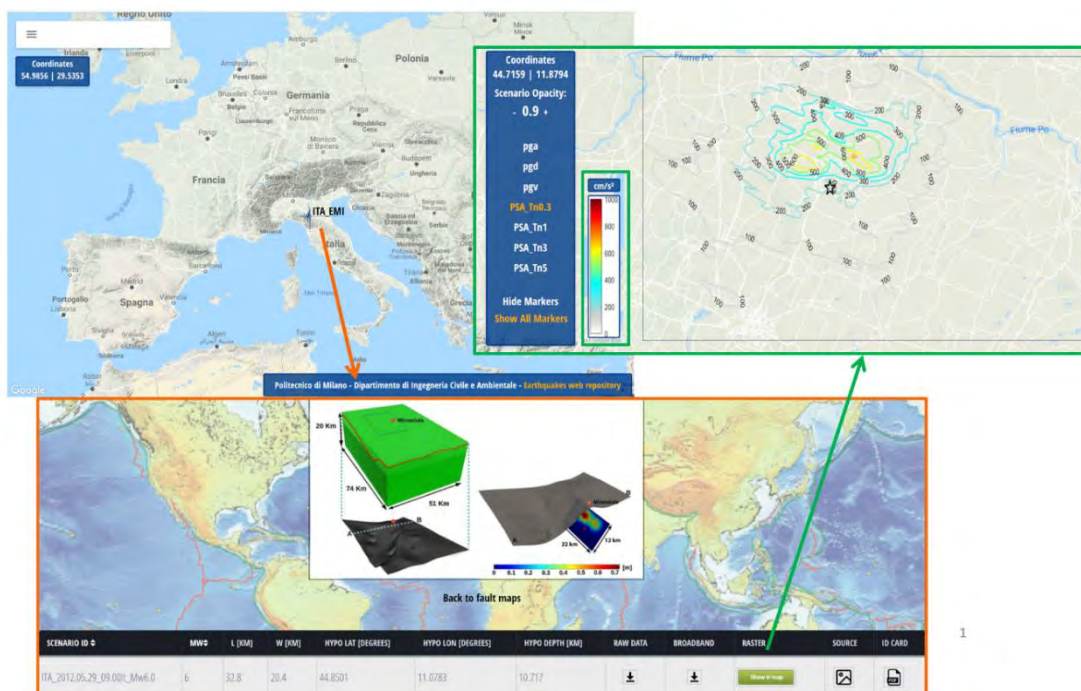


Figure 6.1. Preliminary version of the SPEED Web Repository of processed PBS (<http://speed.mox.polimi.it/WebRepository/>).

References

- Ancheta T.D., Darragh R.B., Stewart J.P., Seyhan E., Silva W.J., Chiou B.S.J., Wooddell K.E., Graves R.W., Kottke A.R., Boore D.M., Kishida T., Donahue J.L. (2013). PEER NGA-West2 Database, PEER Report No. 2013/03, Pacific Earthquake Engineering Research Center, University of California, Berkeley, CA, 134 pp
- Antonietti P.F., Mazzieri I., Melas L., Paolucci R., Quarteroni A., Smerzini C., Stupazzini M. (2020) Three-dimensional physics-based earthquake ground motion simulations for seismic risk assessment in densely populated urban areas, *Mathematics in Engineering*, accepted for publication.
- Baker, J. W. (2007). Quantitative classification of near-fault ground motions using wavelet analysis, *Bull. Seismol. Soc. Am.* 97, no. 5, 1486–1501.
- Bindi, D., M. Massa, L. Luzi, G. Ameri, F. Pacor, R. Puglia, P. Augliera (2014). Pan-European ground-motion prediction equations for the average horizontal component of PGA, PGV, and 5 %-damped PSA at spectral periods up to 3.0 s using the RESORCE dataset, *Bull Earthquake Eng*, DOI 10.1007/s10518-013-9525-5
- Boore D.M. (2010). Orientation-independent, nongeometric-mean measures of seismic intensity from two horizontal components of motion. *Bull. Seismol. Soc. Am.*, 100: 1830–1835
- Bracewell, R. N. (1986). *The Fourier Transform and Its Applications*, Second Ed., McGraw-Hill, New York.
- Cauzzi C, Faccioli E, Vanini M, Bianchini A (2015) Updated predictive equations for broadband (0.01-10 s) horizontal response spectra and peak ground motions, based on a global dataset of digital acceleration records. *Bulletin of Earthquake Engineering* 13(6): 1587-1612. DOI 10.1007/s10518-014-9685-y
- Chiou B.S.J., Youngs R.R. (2008), An NGA model for the average horizontal component of peak ground motion and response spectra. *Earthq Spectra*, 24:173-215.
- DPC - RELUIS (2016). Numerical simulations of earthquakes and near-source effects, Deliverable D3-2016, Engineering characterization of near-source earthquake ground motion, Reluis Research Project RS2. March 2017.
- DPC - RELUIS (2018). Numerical simulations of earthquakes and near source effects, Deliverable D2-2018, The worldwide near-source dataset: data collection and analysis, Reluis Research Project RS2. March 2019.
- Evangelista L., del Gaudio S., Smerzini C., d’Onofrio A., Festa G., Iervolino I., Landolfi L., Paolucci R., Santo A., and Silvestri F.. Physics-based seismic input for engineering applications: a case study in the Aterno River valley, Central Italy. *Bulletin of Earthquake Engineering*, 15(7):2645–2671, 2017
- Guidotti R., Stupazzini M., Smerzini C., Paolucci R. & Ramieri P. (2011) Numerical study on the role of basin geometry and kinematic seismic source in 3D ground motion simulation of the 22 February 2011 MW6.2 Christchurch earthquake, *Seism. Res. Lett.* 82(6): 767–782
- Herrero, A., Bernard P. (1994). A kinematic self-similar rupture process for earthquakes, *Bulletin of Seismological Society of America*, 84, 1216-1229.
- R. Paolucci et al. - Construction of a near-source broadband earthquake ground motion dataset from 3D physics-based numerical simulations - SIGMA2-2020-D3-051

- Infantino M. et al. (2020). 3D physics-based numerical simulations of ground motion in Istanbul from earthquakes along the Marmara segment of the North Anatolian Fault. Accepted for publication in Bulletin of Seismological Society of America.
- Kaklamanos, J., Baise, L.G., Boore, D.M. (2011). Estimating unknown input parameters when implementing the NGA ground-motion prediction equations in engineering practice. *Earthquake Spectra*, 27 (4), 1219-1235.
- Lanzano, G., S. Sgobba, L. Luzi, R. Puglia, F. Pacor, C. Felicetta, M. D'Amico, F. Cotton, and D. Bindi (2018). The pan-European engineering strong motion (ESM) flatfile: Compilation criteria and data statistics, *Bull. Earthq. Eng.*, doi: 10.1007/s10518-018-0480-z.
- Lanzano G., L. Luzi, F. Pacor, C. Felicetta, R. Puglia, S. Sgobba, M. D'Amico (2019). A Revised Ground-Motion Prediction Model for Shallow Crustal Earthquakes in Italy, *Bull. Seis. Soc. Am.*, doi: 10.1785/0120180210.
- Leonard M. (2010). Earthquake Fault Scaling: Self-Consistent Relating of Rupture Length, Width, Average Displacement, and Moment Release, *Bull. Seismol. Soc. Am.*, 100(5A), pp. 1971–1988, October 2010, doi: 10.1785/0120090189
- Mai, P.M. and G.C. Beroza (2000). Source scaling properties from finite-fault-rupture models, *Bull Seismol Soc Am* 90(3):604–615.
- Mavroeidis, G. P., and A. S. Papageorgiou (2003). A mathematical representation of near-fault ground motions, *Bull. Seismol. Soc. Am.* 93, no. 3, 1099–1131
- Mazzieri I, Stupazzini M, Guidotti R, Smerzini C (2013) SPEED: SPectral Elements in Elastodynamics with Discontinuous Galerkin: a non-conforming approach for 3D multi-scale problems. *Int J Numer Meth Eng* 95(12):991–1010
- Norme Tecniche per le Costruzioni 2018, Gazzetta Ufficiale della Repubblica Italiana no 42 del 20 febbraio 2018 (in italian).
- Özcebe, A. G.; Smerzini, C.; Paolucci, R.; Pourshayegan, H.; Rodríguez Plata, R.; Lai, C. G.; Zuccolo, E.; Bozzoni, F., Villani M. (2019) On the comparison of 3D, 2D, and 1D numerical approaches to predict seismic site amplification: the case of Norcia basin during the M6.5 2016 October 30 earthquake. In Proceedings of the 7th International Conference on Earthquake Geotechnical Engineering, Rome, 17-20 June 2019
- Pacor F., Paolucci R., Luzi L., Sabetta F., Spinelli A., Gorini A., Nicoletti M., Marcucci S., Filippi L., Dolce M. (2011). Overview of the Italian strong motion database ITACA 1.0. *Bull Earthquake Eng* 9 (6): 1723–1739. doi: 10.1007/s10518-011-9327-6.
- Pacor F., C. Felicetta, G. Lanzano, S. Sgobba, R. Puglia, M. D'Amico, E. Russo, G. Baltzopoulos, I. Iervolino (2018). NESS1: A Worldwide Collection of StrongMotion Data to Investigate Near-Source Effects, *Seism. Res. Lett.* Vol. 89 (6) November/December 2018.
- Paolucci R., Mazzieri I., Smerzini C., Stupazzini M. (2014) Physics-based earthquake ground shaking scenarios in large urban areas. In A. Ansal, editor, Perspectives on European Earthquake Engineering and Seismology, Geotechnical, Geological and Earthquake Engineering, volume 34.
- Paolucci R., Mazzieri I., Smerzini C. (2015). Anatomy of strong ground motion: near-source records and 3D physics-based numerical simulations of the Mw 6.0 May 29 2012 Po Plain earthquake, Italy, *Geophys. J. Int.* 203, 2001–2020.
- Paolucci R., Evangelista L., Mazzieri I., Schiappapietra E. (2016) The 3D numerical simulation of near-source ground motion during the Marsica earthquake, central Italy, 100 years later. *Soil Dynamics and Earthquake Engineering*, 91: 39-52.
- R. Paolucci et al. - Construction of a near-source broadband earthquake ground motion dataset from 3D physics-based numerical simulations - SIGMA2-2020-D3-051

- Paolucci, R., F. Gatti, M. Infantino, C. Smerzini, A. G. Özcebe, and M. Stupazzini (2018). Broadband Ground Motions from 3D Physics-Based Numerical Simulations Using Artificial Neural Networks, *Bulletin of Seismological Society of America* 108, 1272-1286.
- Paolucci R., Mazzieri I., Piunno G., Smerzini C., Vanini M., Özcebe A.G. (2020) Earthquake ground motion modelling of induced seismicity in the Groningen gas field, *Earthquake Engineering and Structural Dynamics*, submitted for publication.
- Pilz M., S. Parolai, M. Stupazzini, R. Paolucci, J. Zschau (2011). Modelling basin effects on earthquake ground motion in the Santiago de Chile basin by a spectral element code. *Geophys. J. Int.* (2011) 187, 929–945. doi: 10.1111/j.1365-246X.2011.05183.x
- Rathje EM, Abrahamson NA, Bray JD (1998) Simplified frequency content estimates of earthquake ground motions. *J Geotech Geoenviron Eng* 124(2):150–159
- Scherbaum F., J. Schmedes, and F. Cotton (2004). On the Conversion of Source-to-Site Distance Measures for Extended Earthquake Source Models. *Bulletin of the Seismological Society of America*, 94(3), 1053–1069.
- Schmedes, J., R.J. Archuleta, and D. Lavallée (2012). A kinematic rupture model generator incorporating spatial interdependency of earthquake source parameters, *Geophysical Journal International* 192, 1116-1131.
- Shai S.K., J.W. Baker (2011). An Empirically Calibrated Framework for Including the Effects of Near-Fault Directivity in Probabilistic Seismic Hazard Analysis. *Bulletin of the Seismological Society of America*, Vol. 101, No. 2, pp. 742–755, April 2011, doi: 10.1785/0120100090
- Shai S.K., J.W. Baker (2014). An Efficient Algorithm to Identify Strong-Velocity Pulses in Multicomponent Ground Motions. *Bulletin of the Seismological Society of America*, Vol. 104, No. 5, pp. 2456–2466, October 2014, doi: 10.1785/0120130191
- Smerzini C., Paolucci R., Stupazzini M. (2011) Comparison of 3D, 2D and 1D numerical approaches to predict long period earthquake ground motion in the Gubbio plain, Central Italy. *Bulletin of Earthquake Engineering*, 9(6):2007–2029.
- Smerzini C., Paolucci R., Faccioli E., Sirovich L., Sandron D. (2010) Numerical simulations of earthquake ground motion in near-fault conditions, Deliverable D4 Project PRIN "Prediction of ground motion and generation of shaking maps in the near-fault of an earthquake".
- Smerzini C., Villani M. (2012). Broadband Numerical Simulations in Complex Near-Field Geological Configurations: The Case of the 2009 Mw 6.3 L'Aquila Earthquake, *Bull. Seismol. Soc. Am.* 102, no. 6, 2436–2451.
- Smerzini C., Galasso C., Iervolino I., Paolucci R. (2014). Ground motion record selection based on broadband spectral compatibility, *Earthq. Spectra* 30, no. 4, 1427–1448.
- Smerzini C., Pitilakis K., Hashemi K. (2017) Evaluation of earthquake ground motion and site effects in the Thessaloniki urban area by 3D finite-fault numerical simulations. *Bulletin of Earthquake Engineering* 15(3):787–812
- C. Smerzini (2018) Spatial variability of earthquake ground motion from 3D physics-based numerical simulations. In *Proceedings of the 16th European Conference on Earthquake Engineering*, Thessaloniki, 18-21 June 2018.
- Stupazzini M., Paolucci R., Igel H. (2009). Near-fault earthquake ground-motion simulation in Grenoble Valley by high-performance spectral element code. *Bull Seismol Soc Am* 99(1):286–301, doi: 10.1785/0120080274

- Stupazzini, M., M. Infantino, A. Allmann, and R. Paolucci (2020). Physics-based Probabilistic Seismic Hazard and Loss Assessment in Istanbul, submitted to Earthquake Engineering and Soil Dynamics.
- Thingbaijam K.K.S., P.M. Mai (2016). Evidence for truncated exponential probability distribution of earthquake slip, *Bull Seismol Soc Am* 106(4):1802–1816.
- Villani M., Faccioli E., Ordaz M. & Stupazzini M. (2014) High-resolution seismic hazard analysis in a complex geological configuration: the case of the Sulmona basin in Central Italy, *Earthq. Spectra* 30(4): 1801–1824
- Wells, D., Coppersmith, K.. (1994). New Empirical Relationships among Magnitude, Rupture Length, Rupture Width, Rupture Area, and Surface Displacement. *Bull Seismol Soc Am* 84, 974-1002.

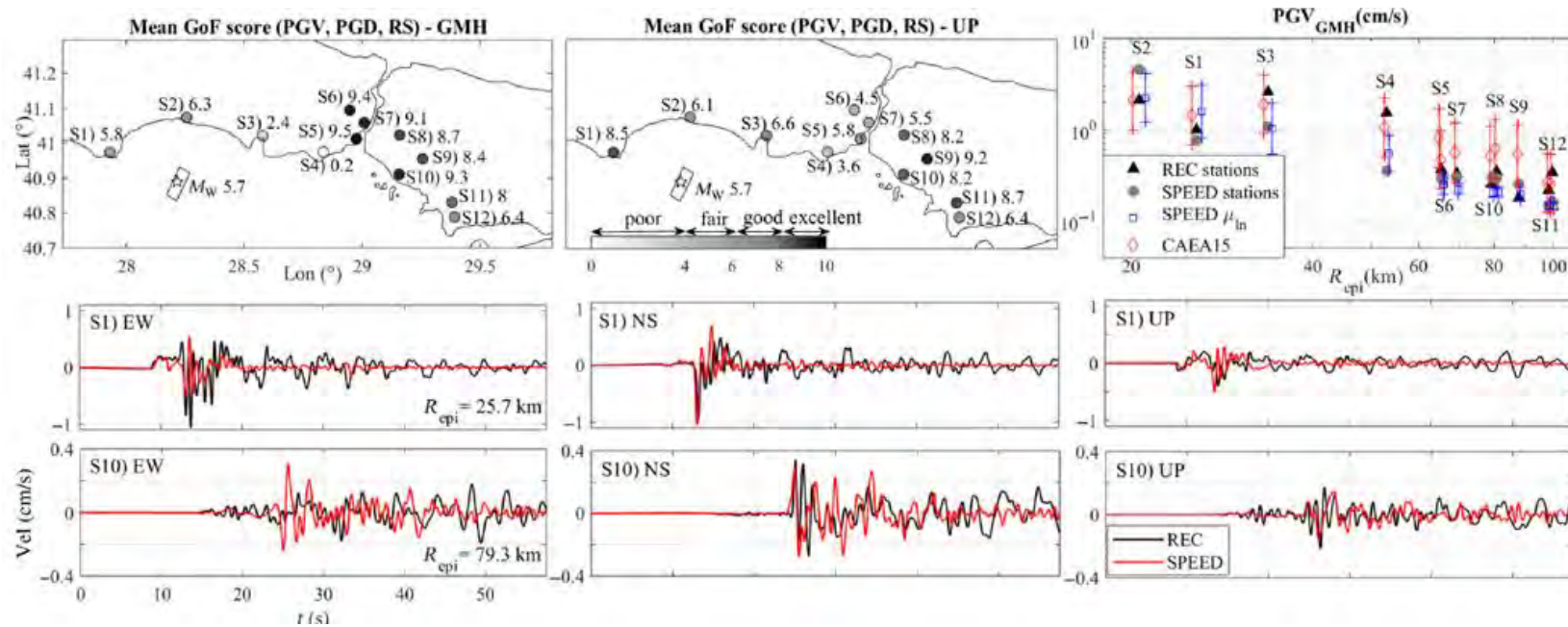
Appendix A

In the following pages, a collection of validations is shown, for the cases studied and published by the Politecnico di Milano research group. Validations include examples for:

1. validations against records of past earthquakes;
2. evaluation of the components of ground motion variability;
3. comparisons against GMPEs;
4. studies of spatial correlation and spatial coherency features;
5. estimation of local site response.

A.1.1 Istanbul case study: validation against records of a Mw 5.7 earthquake

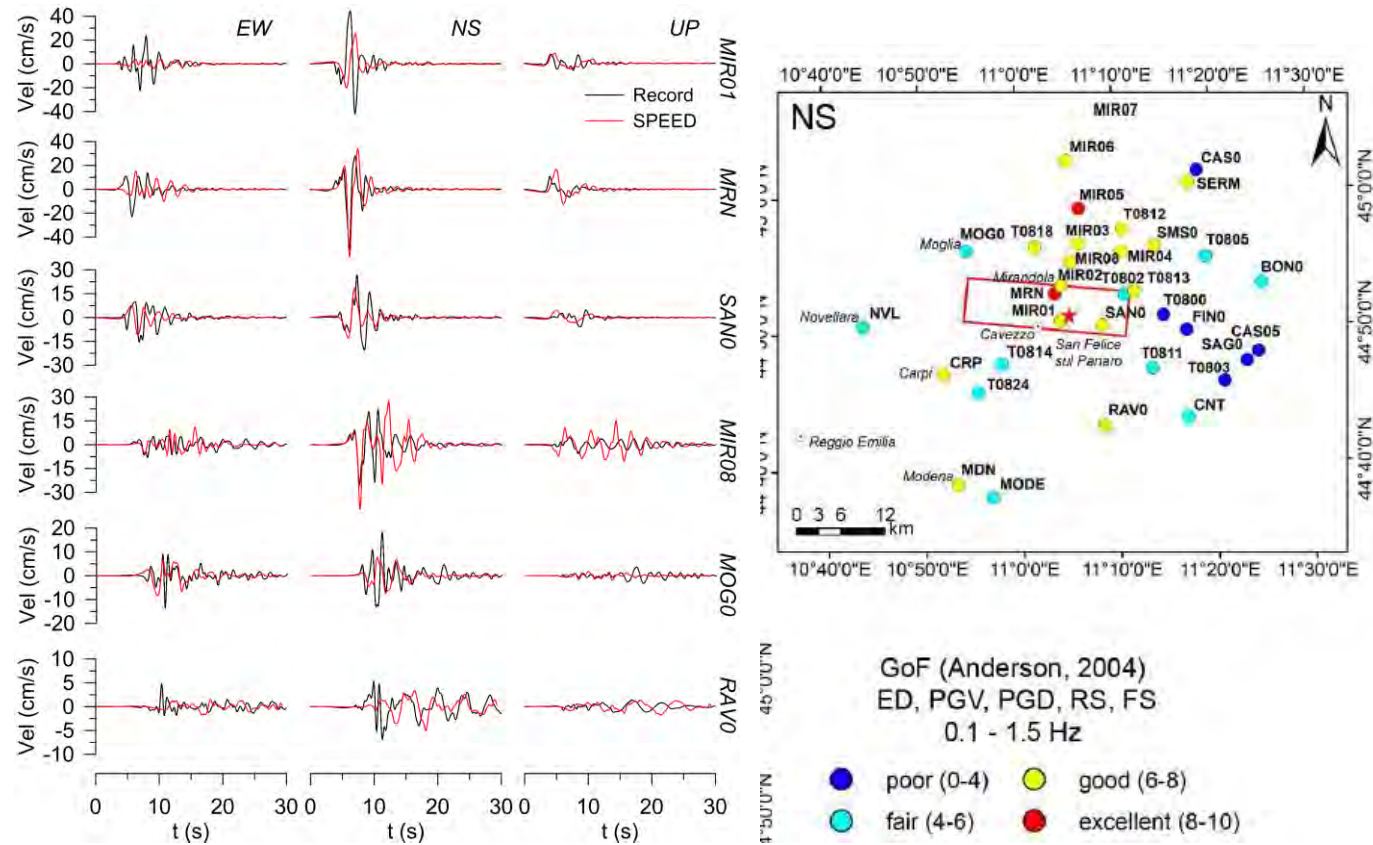
Infantino M., Mazzieri I., Ozcebe A.G., Paolucci R., Stupazzini M. (2020). 3D Physics-Based Numerical Simulations of Ground Motion in Istanbul from Earthquakes along the Marmara Segment of the North Anatolian Fault, BSSA, in press.



Validation comparisons between records of Mw5.7 September 26th, 2019 Marmara Sea earthquake and numerical simulations. Data are band-pass filtered between 0.05 and 1.5Hz. Top left: maps of the mean of three Good of Fitness (GoF) scores (PGV, PGD and RS) according to Anderson (2004) for the geometric mean of the horizontal components GMH and the vertical component UP. The score is also indicated close to each station. The fault projection and epicenter of the earthquake is also shown. Top right: PGV (HGM) trend with R_{epi} . Records (REC) are denoted by triangles, SPEED results by circles, while squares and lines denote the median and standard deviations of the SPEED values for values of distance and VS,30 consistent with REC. Moreover, the median +/- standard deviation of the Cauzzi et al. (2015) GMPE are shown and represented by diamonds and lines respectively. Bottom: three components velocity time histories comparison for 2 selected stations, namely S1 and S10.

A.1.2 Emilia Mw 6.0 case study: validation against records of the 2012 May 29 earthquake (I)

Paolucci R., Mazzieri I., Smerzini C. (2015). Anatomy of strong ground motion: near-source records and 3D physics-based numerical simulations of the Mw 6.0 May 29 2012 Po Plain earthquake, Italy, *Geophys. J. Int.* 203, 2001–2020.

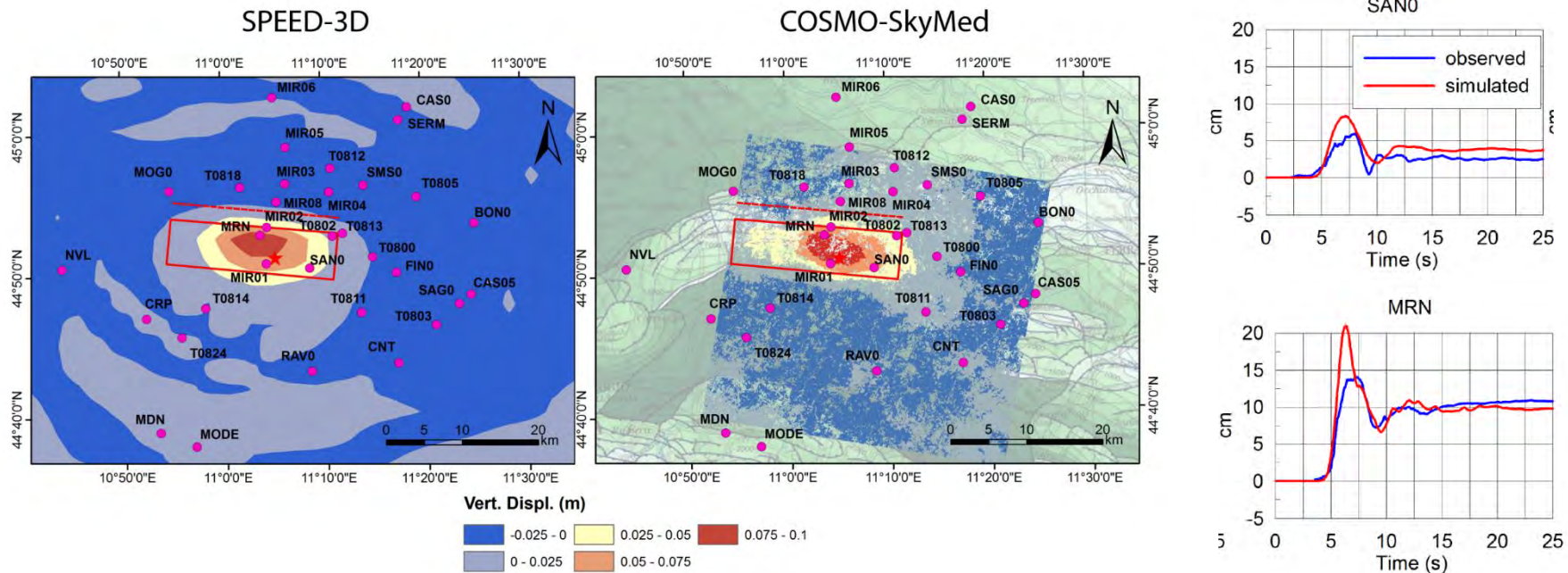


Left: comparison between recorded (black line) and simulated (red line) three-component velocity waveforms for a representative subset of strong motion stations. Data are band-pass filtered between 0.1 and 1.5 Hz. Right: map of GoF scores according to Anderson (2004) for all available stations at $R_{epi} < 30$ km for NS components.

R. Paolucci et al. - Construction of a near-source broadband earthquake ground motion dataset from 3D physics-based numerical simulations - SIGMA2-2020-D3-

A.1.3 Emilia Mw 6.0 case study: validation against records of the 2012 May 29 earthquake (II)

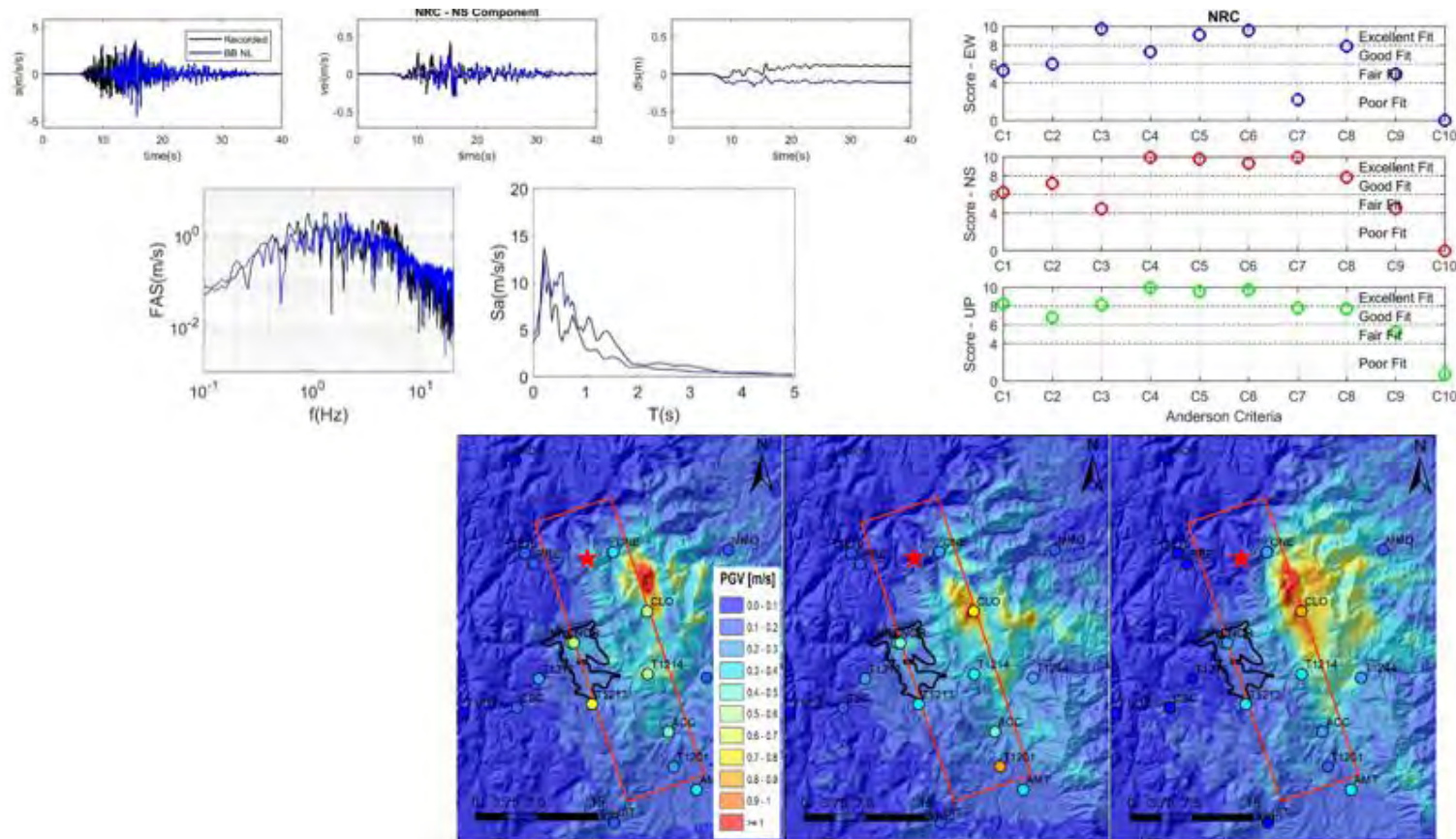
Paolucci R., Mazzieri I., Smerzini C. (2015). Anatomy of strong ground motion: near-source records and 3D physics-based numerical simulations of the Mw 6.0 May 29 2012 Po Plain earthquake, Italy, *Geophys. J. Int.* 203, 2001–2020.



Left: map of permanent ground uplift simulated by SPEED and observed by InSAR processing. In both maps the surface projection of the fault area is shown, together with the intersection of the fault plane with ground surface (dashed line). Right: comparison between observed (blue line) and simulated (red line) vertical displacement time histories at two near-source recording stations (left, SAN0; right, MRN). Acceleration records were processed by a piecewise baseline correction, suitable to recover permanent displacements.

A.1.4 Norcia Mw 6.5 case study: validations against records of the 2016 October 30 earthquake

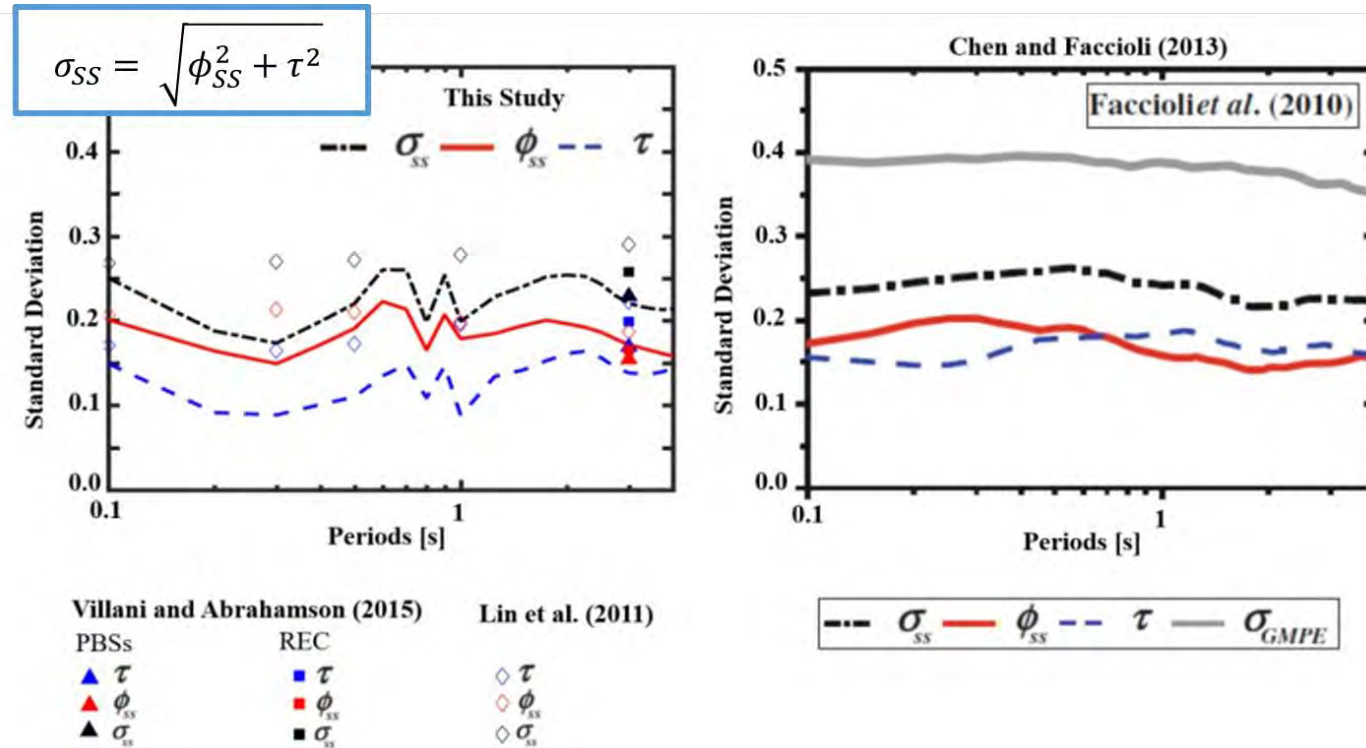
Özcebe, A. G. et al. (2019) On the comparison of 3D, 2D, and 1D numerical approaches to predict seismic site amplification: the case of Norcia basin during the M6.5 2016 October 30 earthquake. In Proceedings of the 7th International Conference on Earthquake Geotechnical Engineering, Rome, 17-20 June 2019



Top-left: comparison between broadband simulations and ground motion recordings at NRC station during the 30 Oct 2016 Norcia earthquake; Top-right: corresponding GoF criteria according to Anderson (2004). Bottom: EW, NS and UD PGV map from PBSs and comparison with the recorded values at the strong-motion stations (filled dots).

A.2 Istanbul case study: evaluation of the components of ground motion variability based on PBSs

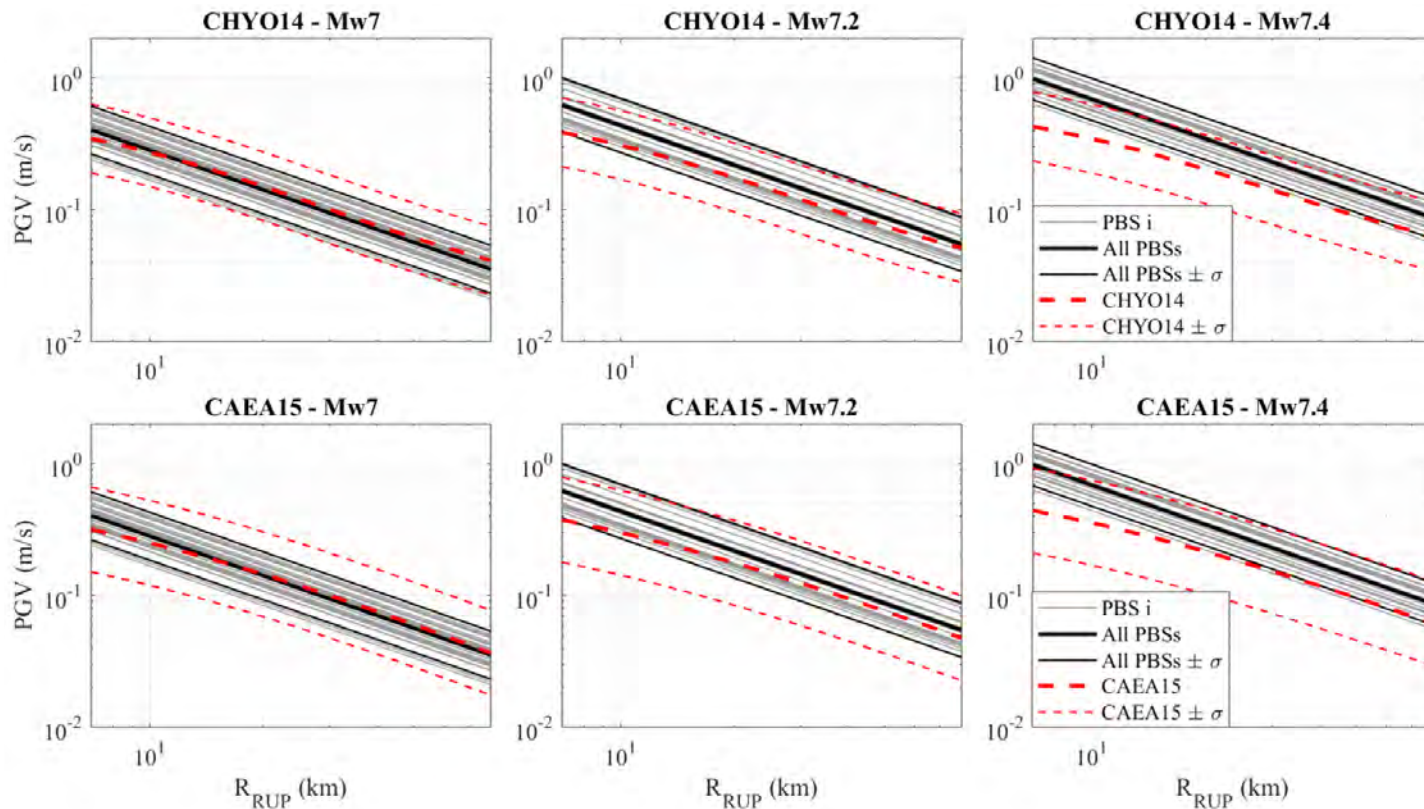
M. Stupazzini, M. Infantino, A. Allman, R. Paolucci. PHYSICS-BASED PROBABILISTIC SEISMIC HAZARD AND LOSS ASSESSMENT IN LARGE URBAN AREAS: AN APPLICATION TO ISTANBUL. Earthquake Engineering and Structural Dynamics. 2020 Submitted.



Left: components of single-station standard deviation from PBSs (lines) and from independent studies by Villani and Abrahamson (2015) (triangle and squares) and Lin et al. (2011) (diamonds). Right: components of single-station standard deviation of the Canterbury database from Chen and Faccioli (2013).

A.3 Istanbul case study: comparisons against GMPEs

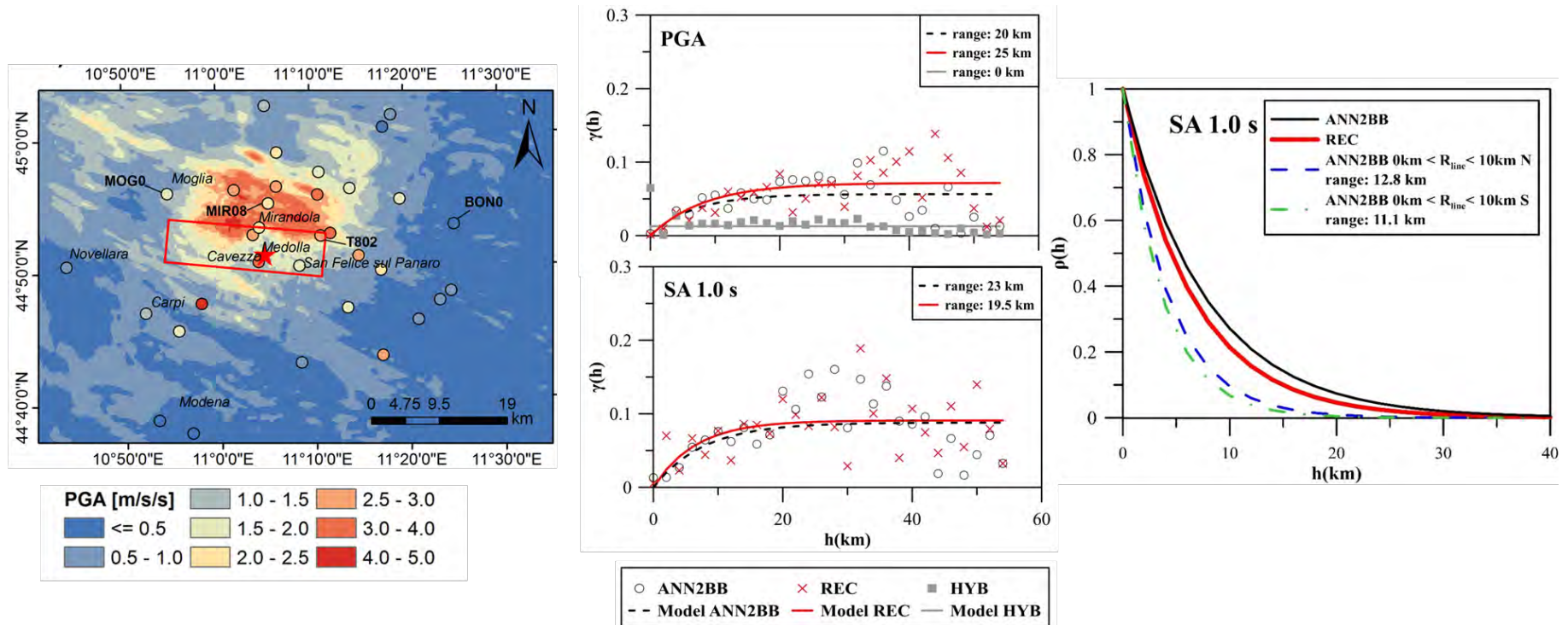
Infantino M., Mazzieri I., Ozcebe A.G., Paolucci R., Stupazzini M. (2020). 3D Physics-Based Numerical Simulations of Ground Motion in Istanbul from Earthquakes along the Marmara Segment of the North Anatolian Fault, BSSA, in press.



Comparison between Chiou and Youngs 2014 (CHYO14) (top panels) and Cauzzi et al. 2015 (CAEA15) (bottom panels) median PGV $\pm \sigma$ (dashed lines) and regression models based on PBSs (solid lines) for Mw 7.0 (left), 7.2 (centre) and 7.4 (right) for the sites with a V_{S30} of 650 m/s. The thin lines display the regression curves referred to each PBS.

A.4.1 Emilia Mw 6.0 case study: spatial correlation from PBS and records

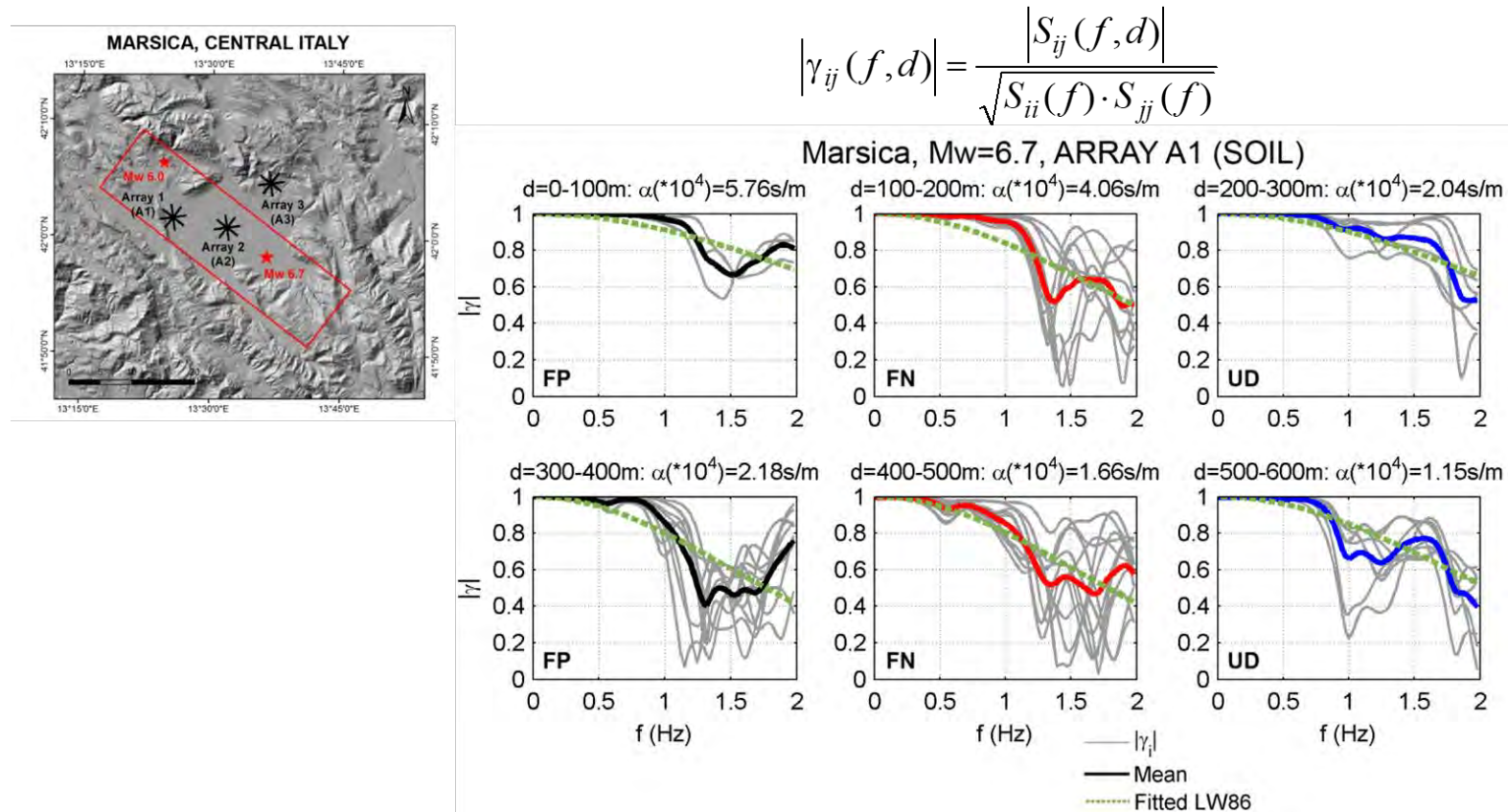
Paolucci, R., F. Gatti, M. Infantino, C. Smerzini, A. G. Özcebe, and M. Stupazzini (2018). Broadband Ground Motions from 3D Physics-Based Numerical Simulations Using Artificial Neural Networks, *Bulletin of Seismological Society of America* 108, 1272-1286.



Left: PGA map (geometric mean of horizontal components) from ANN2BB approach and comparison with recorded values (filled dots). Center: semi-variograms computed from PGA and SA(1.0s) using records (REC), the ANN2BB approach and the standard Hybrid (HYB) approach. Right: spatial correlation models obtained from the REC and ANN2BB values: sensitivity of the correlation with respect to the R_{line} range.

A.4.2 Marsica Mw 6.7 case study: spatial coherency estimates

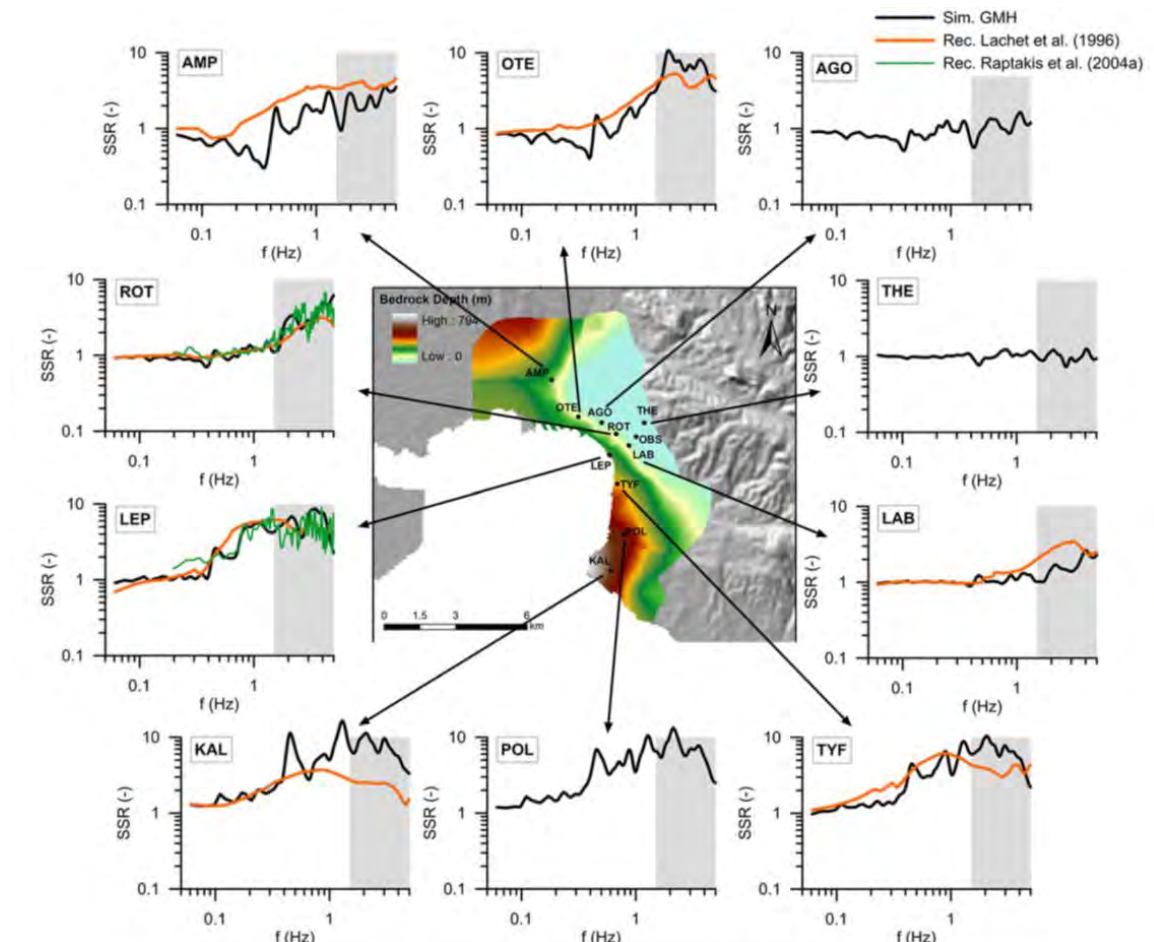
C. Smerzini (2018) Spatial variability of earthquake ground motion from 3D physics-based numerical simulations. In Proceedings of the 16th European Conference on Earthquake Engineering, Thessaloniki, 18-21 June 2018



Marsica (Mw 6.7): evaluation of lagged coherency function in the frequency range 0-2 Hz from pairs of PBS waveforms within different separation distance bins and for different components (FP, FN and UD). The mean coherency from simulations is compared with the best-fitting Luco and Wong (1986) semi-empirical model (dashed green lines).

A.5 Thessaloniki Mw 6.5 case study: estimation of local site response

Smerzini C., Ptilakis K., Hashemi K. (2017) Evaluation of earthquake ground motion and site effects in the Thessaloniki urban area by 3D finite-fault numerical simulations. *Bulletin of Earthquake Engineering* 15(3):787–812



Thessaloniki case study: comparison between recorded and simulated Standard Spectral Ratios (SSRs) at sites within the Thessaloniki urban area with respect to OBS reference station.

Appendix B

A brief description of the fields of the flat file table is given herein, grouping them as: 1) source metadata, 2) receiver metadata, 3) site response proxies, 4) source to site distances and 5) Intensity Measures.

1) Source Metadata

- Scenario ID: identifier of the simulated scenario
- Event ID: identifier of the simulated event
- Scenario ID card: link to the ID Card (pdf file) that summarizes numerical simulation data and results
- Event_Time: time and date of the simulated event
- Event Nation Code: ISO code of the country where the epicenter of the event is located
- Hypocenter Lat/Lon/Depth: geographic coordinates [decimal degrees] of the starting point of the rupture on the fault plane
- M_w : moment magnitude
- M_o : total seismic moment [Nm]
- Average slip: average slip on the fault [m]
- No. segments: number of ruptured fault segments
- Strike: fault strike [degrees from North]
- Dip: fault dip [degrees]
- Rake: fault rake [degrees]
- Fault mechanism: style of faulting of the simulated event (SS strike-slip, NN normal, TF thrust)
- Rupture top: depth of the fault top [km]
- Fault Vertices: geographic coordinates of the reference points of both “numerical” (i.e. as implemented in the mesh) and “effective” fault plane
- Length: numerical and effective fault length [km]
- Width: numerical and effective fault width [km]
- References: published references of the simulated event

- ANN_database: the database used to train the ANN
- Transition period: the merging period between PBS and ANN
- ANN2BB_procedure: the current version of the procedure used to merge low and high frequency signals

2) Receiver Metadata

- Receiver ID: identification number of the receiver of the numerical simulation
- Receiver East/North coordinates: geographical coordinates of the receiver
- Receiver elevation: elevation of the receiver [m]

2) Site Response Proxies (calculated from the numerical model)

- $V_{S,30}$: time-averaged shear wave velocity [m/s] in the uppermost 30 m
- $H_{bedrock}$: depth [m] to the geologic bedrock (corresponding to the lowest resonance frequency) of the simulation model
- $V_{S,H_{bedrock}}$: time-averaged shear wave velocity [m/s] of the layers down to the depth $H_{bedrock}$
- H_{800} : depth [m] of the layer with shear wave velocity equal or larger than 800 m/s

- $V_{s,800}$: time-averaged shear wave velocity [m/s] of the layers down to the depth H_{800}
- $V_{s,eq}$ (or $V_{s,H}$): time-averaged shear wave velocity [m/s] of the layers down to the depth $H=H_{800}$ (if $H>30$ m, then $H=30$ m)
- Slope: slope of the topographic surface

4) Source-to-Site Distances (calculated from effective fault dimensions)

- R_{hyp} : hypocentral distance [km], i.e. distance from the starting point of the rupture on the fault plane (hypocenter)
- R_{epi} : epicentral distance [km], i.e. distance from the surface projection of the hypocenter
- R_{line} : the closest distance [km] from the surface projection of the top edge of the fault plane
- R_X : hanging wall distance [km] calculated according to Ancheta et al. (2013)
- R_{JB} : Joyner and Boore distance [km], i.e. the closest distance from surface projection of fault plane
- R_{rup} : rupture distance [km], i.e. the closest distance from the fault plane

5) Intensity Measures (*)

- PGA: peak ground acceleration [m/s^2]
- PGV: peak ground velocity [m/s]
- PGD: peak ground displacement [m]
- Permanent displacement: permanent displacement [m]
- SA(T) for T from 0.01 to 10 s: spectral acceleration [m/s^2] for vibration periods from 0.01 to 10 s
- Pulse-like: 1/0 flag identifying pulse like behavior
- Pulse period: period [s] of the identified velocity pulse
- D_{s595}: significant duration defined as 5%-95% of Arias intensity
- D_{s575}: significant duration defined as 5%-75% of Arias intensity
- Housner Intensity: [m]
- Arias Intensity: [m/s]
- Cumulative Absolute Velocity: area under the absolute accelerograms [m/s]
- Mean period: mean period [s] based on the Fourier Amplitude Spectrum according to Rathje et al. (1998)

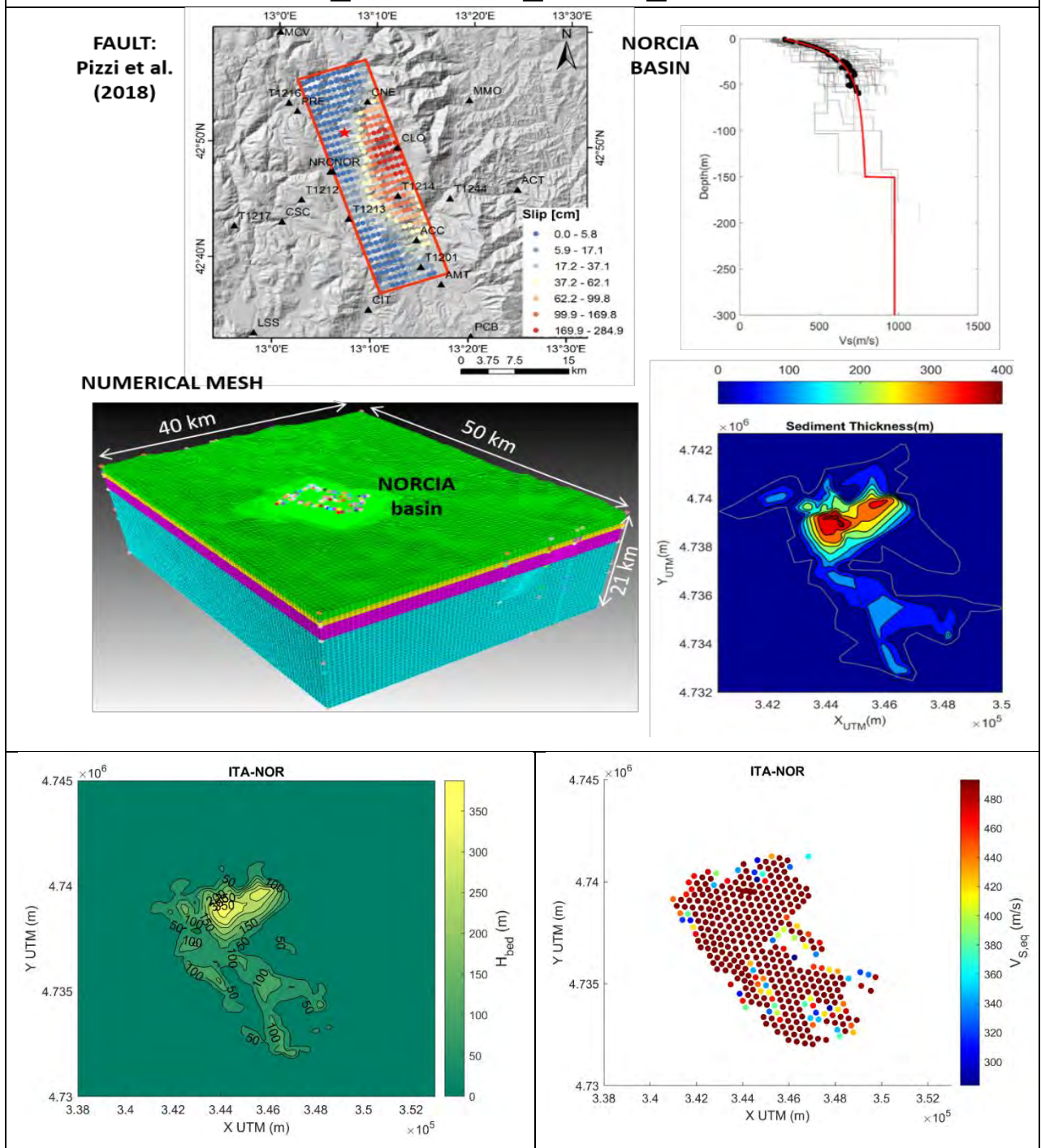
(*) Except pulse features, Intensity Measures are defined for the following directions: NS, EW = horizontal; UD = vertical; HGM= horizontal geometrical mean; FN=Fault Normal; FP=Fault Parallel; RotD50 = median value of the IM distribution obtained from rotated waveforms; RotD100 = maximum value of the IM distribution obtained from rotated waveforms. (Rotation angles are given as well.

Appendix C

In the following pages, a summary of the processed simulations is shown. For each scenario the following information is provided in 7 pages:

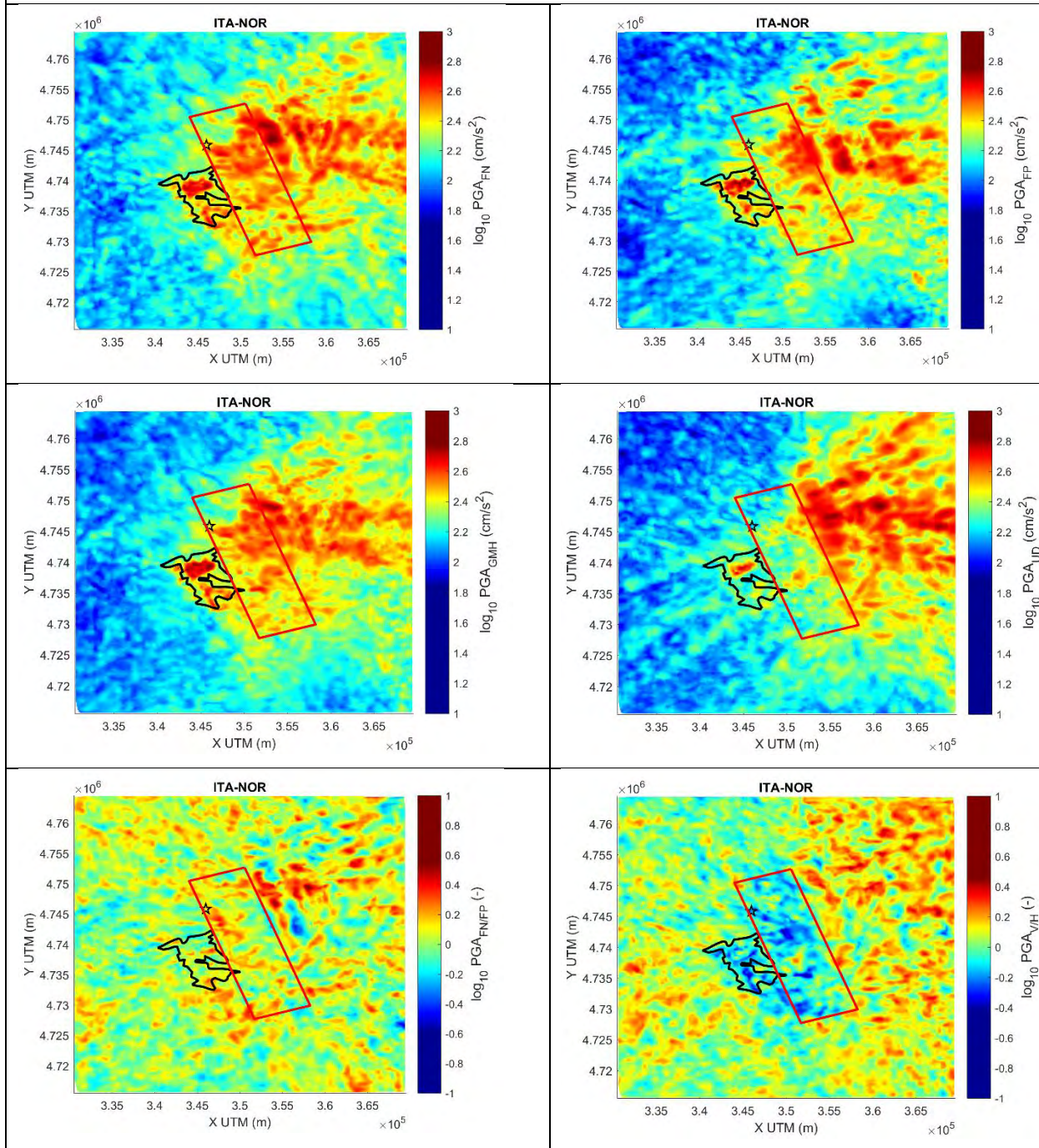
6. Numerical scenario overview;
7. PGA maps. Top: fault normal (FN) and fault parallel (FP) components. Center: geometric mean and vertical components. Bottom: (left) FN/FP ratio; (right) V/H ratio (where H=HGM);
8. PGA variability as a function of R_{line} : Top: fault normal (FN) and fault parallel (FP) components. Center: geometric mean and vertical components. Bottom: (left) FN/FP ratio; (right) V/H ratio (where H=HGM);
9. PGV maps. same as for PGA;
10. PGV variability as a function of R_{line} : same as for PGA;
11. SA(3s) maps. same as for PGA;
12. SA(3s) variability as a function of R_{line} : same as for PGA.

ITA_2016.10.30_07.40It_Mw6.5



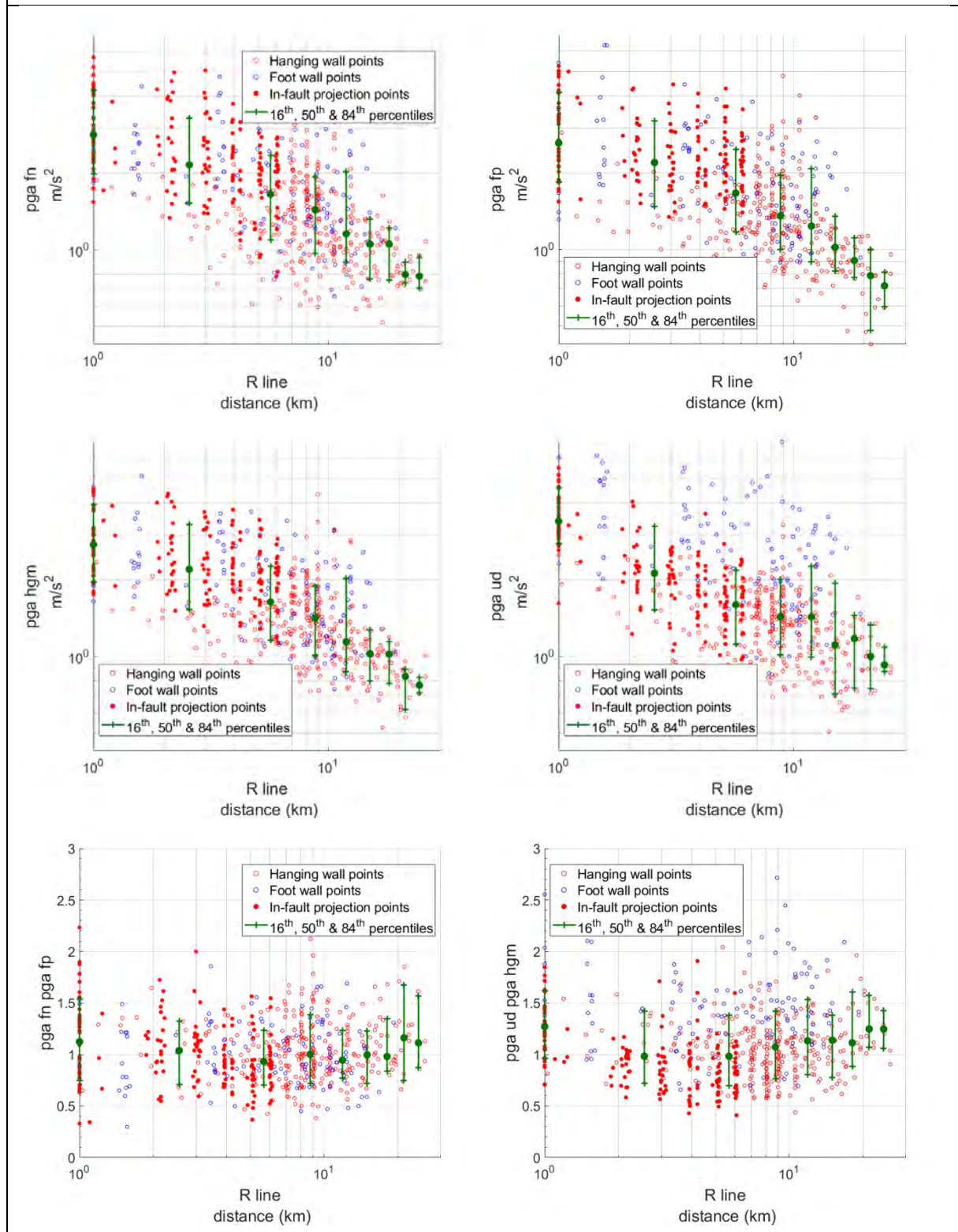
ITA_2016.10.30_07.40It_Mw6.5

MAPS: PGA



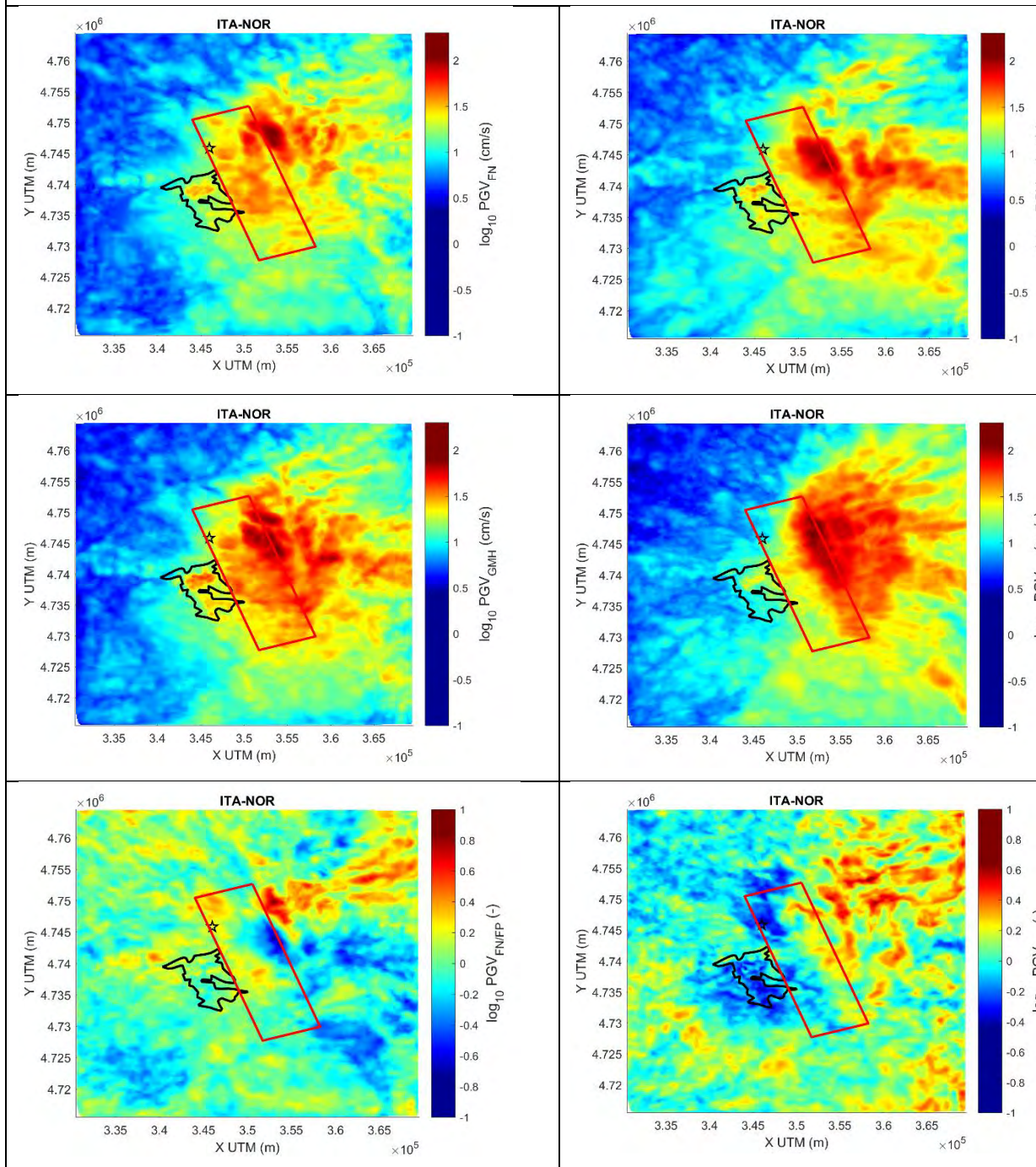
ITA_2016.10.30_07.40lt_Mw6.5

Attenuation with distance: PGA



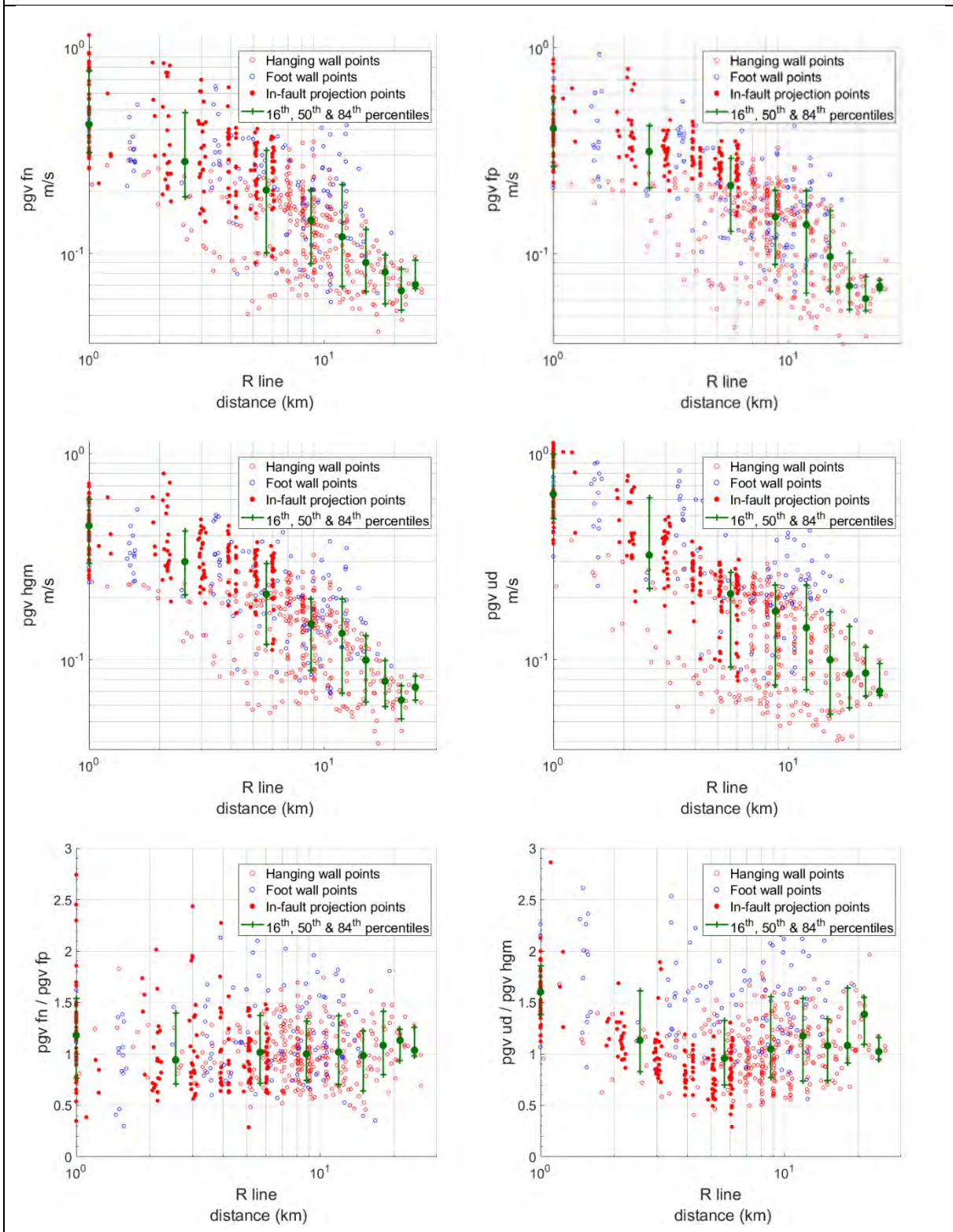
ITA_2016.10.30_07.40It_Mw6.5

MAPS: PGV



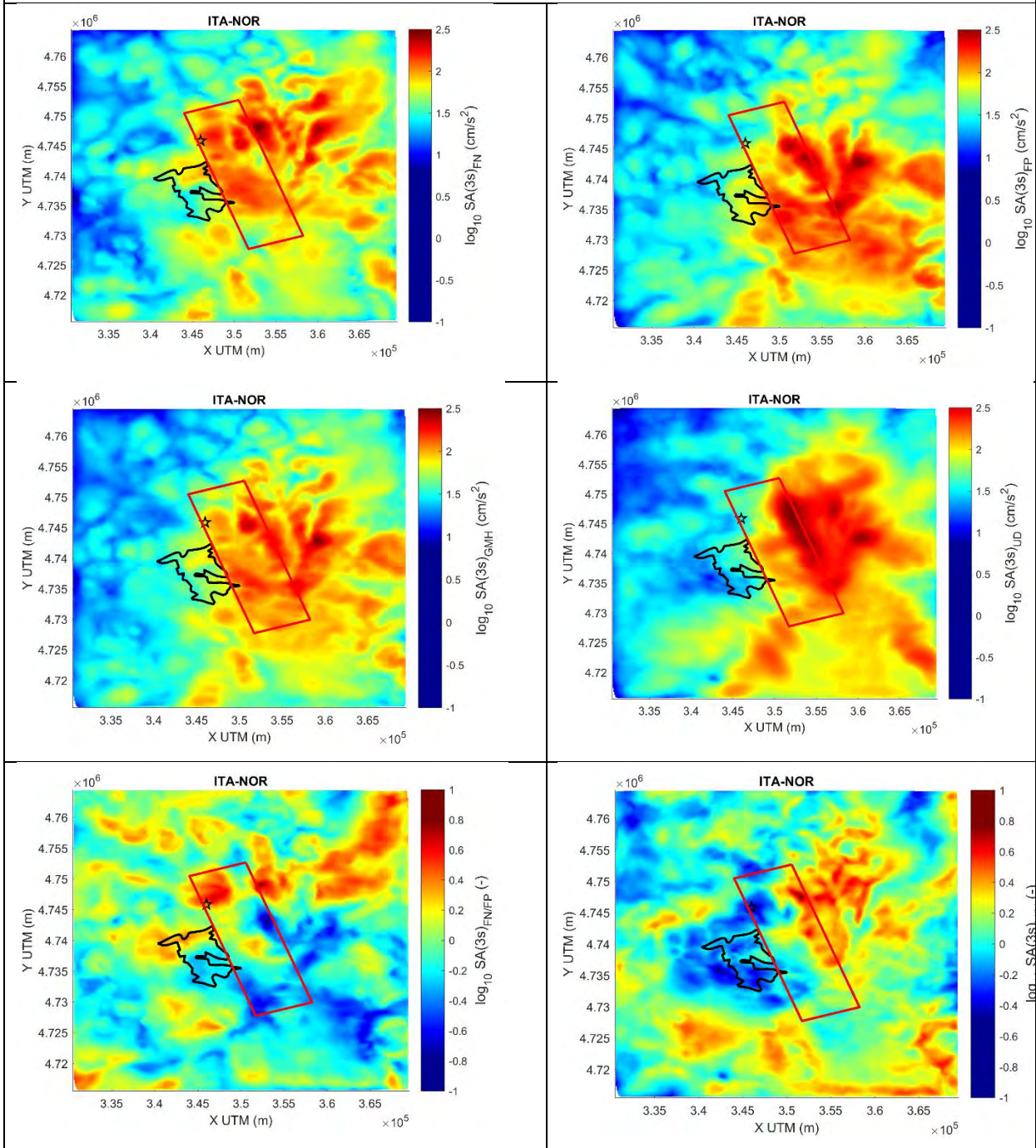
ITA_2016.10.30_07.40lt_Mw6.5

Attenuation with distance: PGV



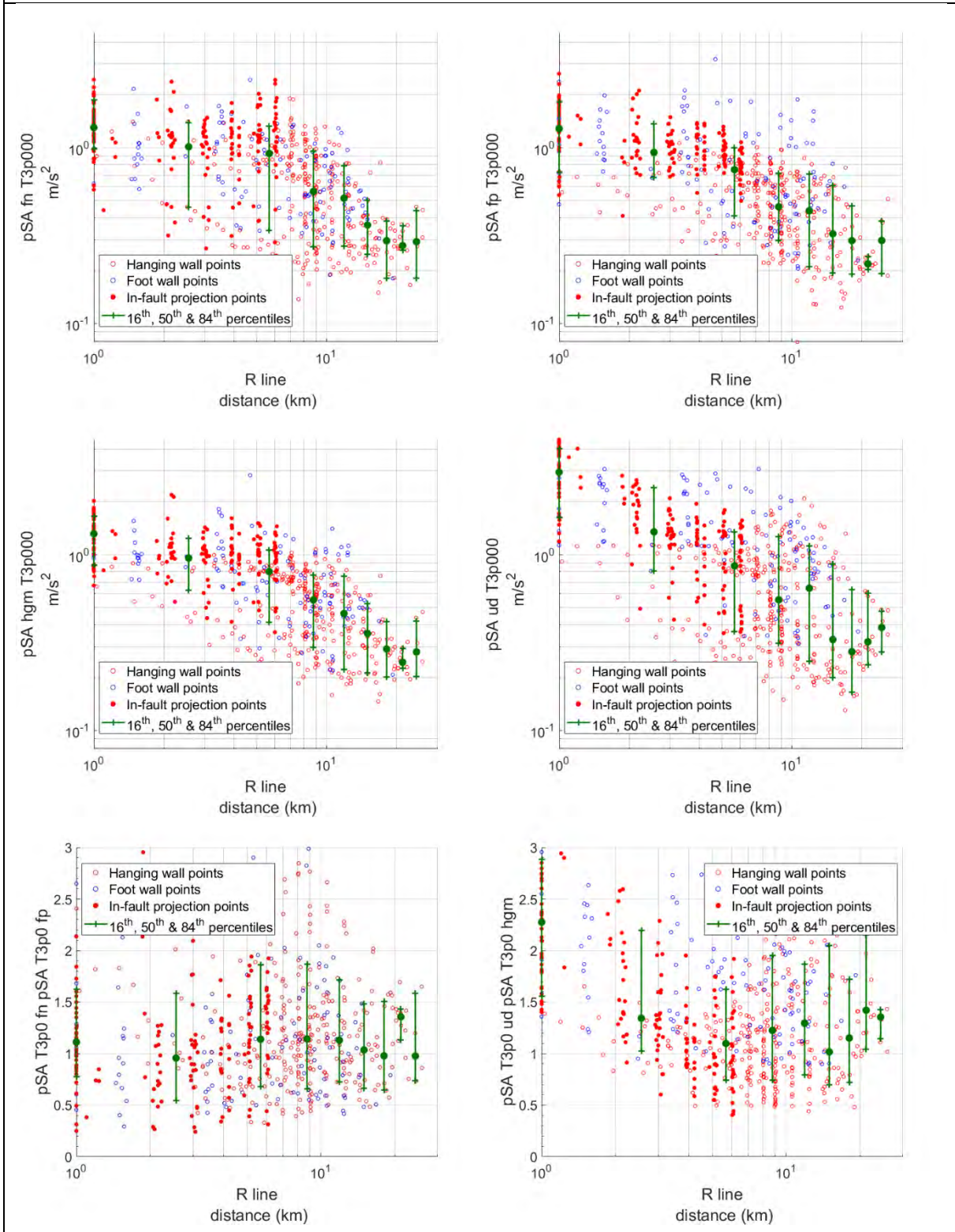
ITA_2016.10.30_07.40It_Mw6.5

MAPS: SA(3s)

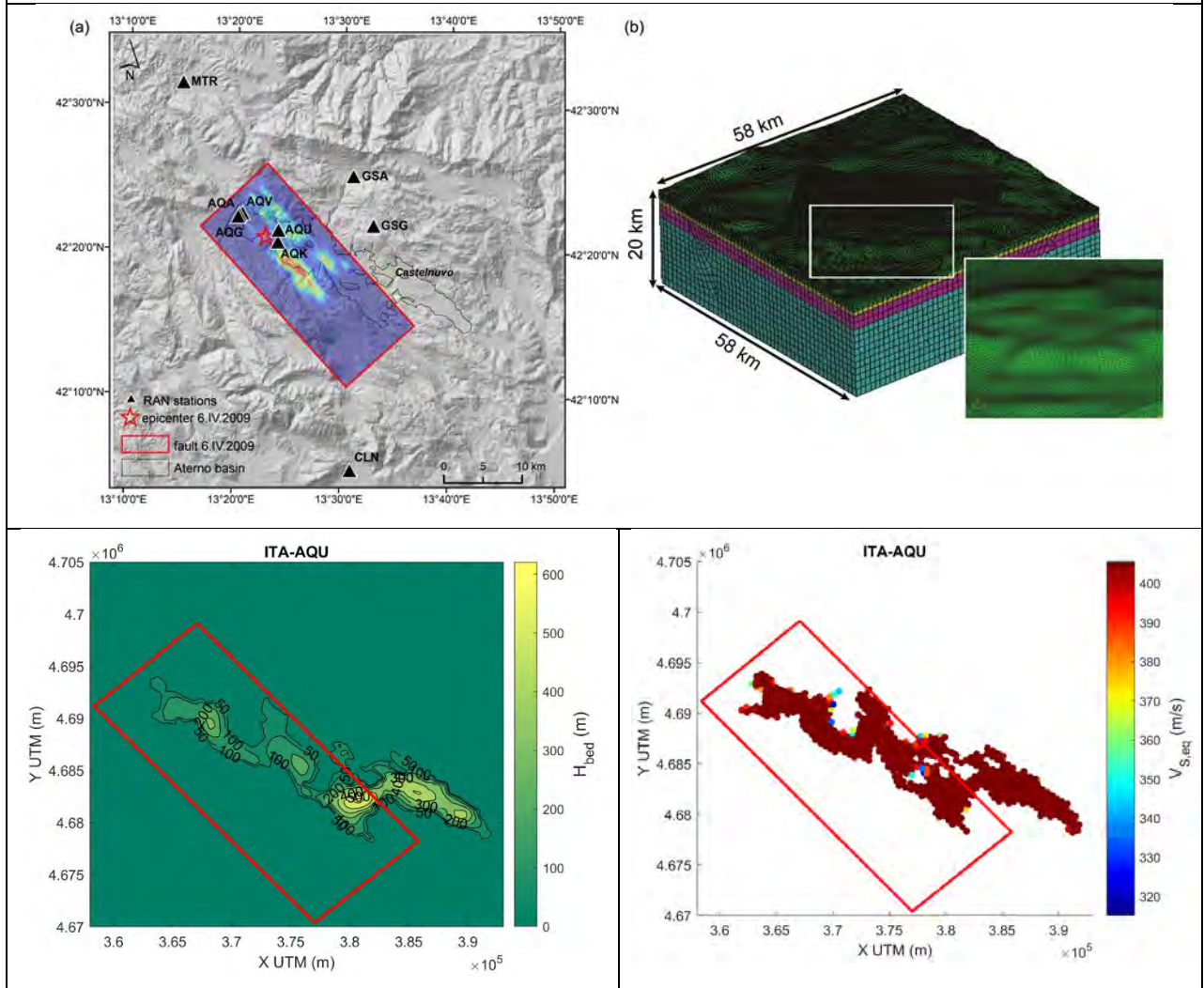


ITA_2016.10.30_07.40lt_Mw6.5

Attenuation with distance: SA(3s)

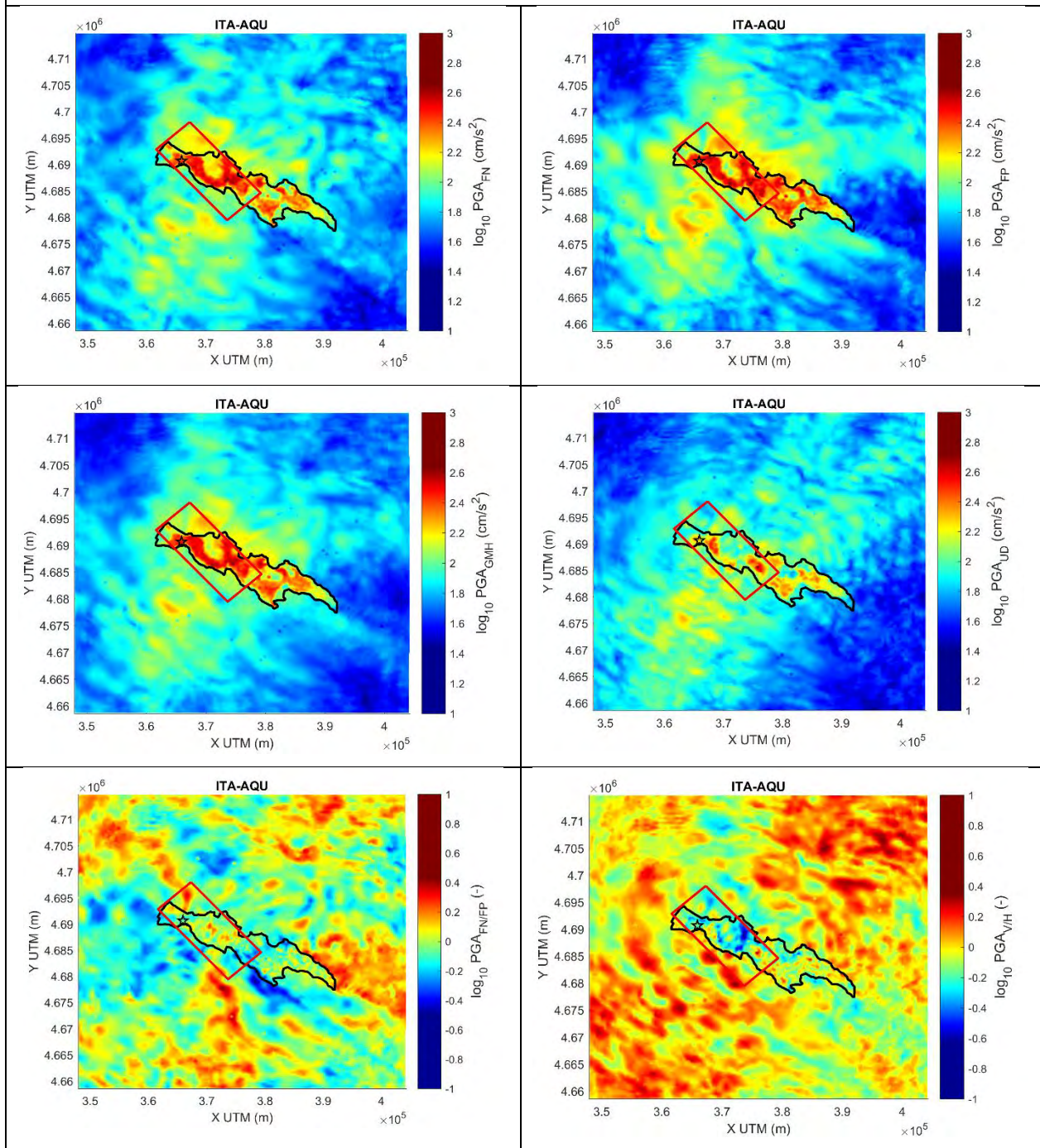


ITA_2009.04.06_03.32It_Mw6.2



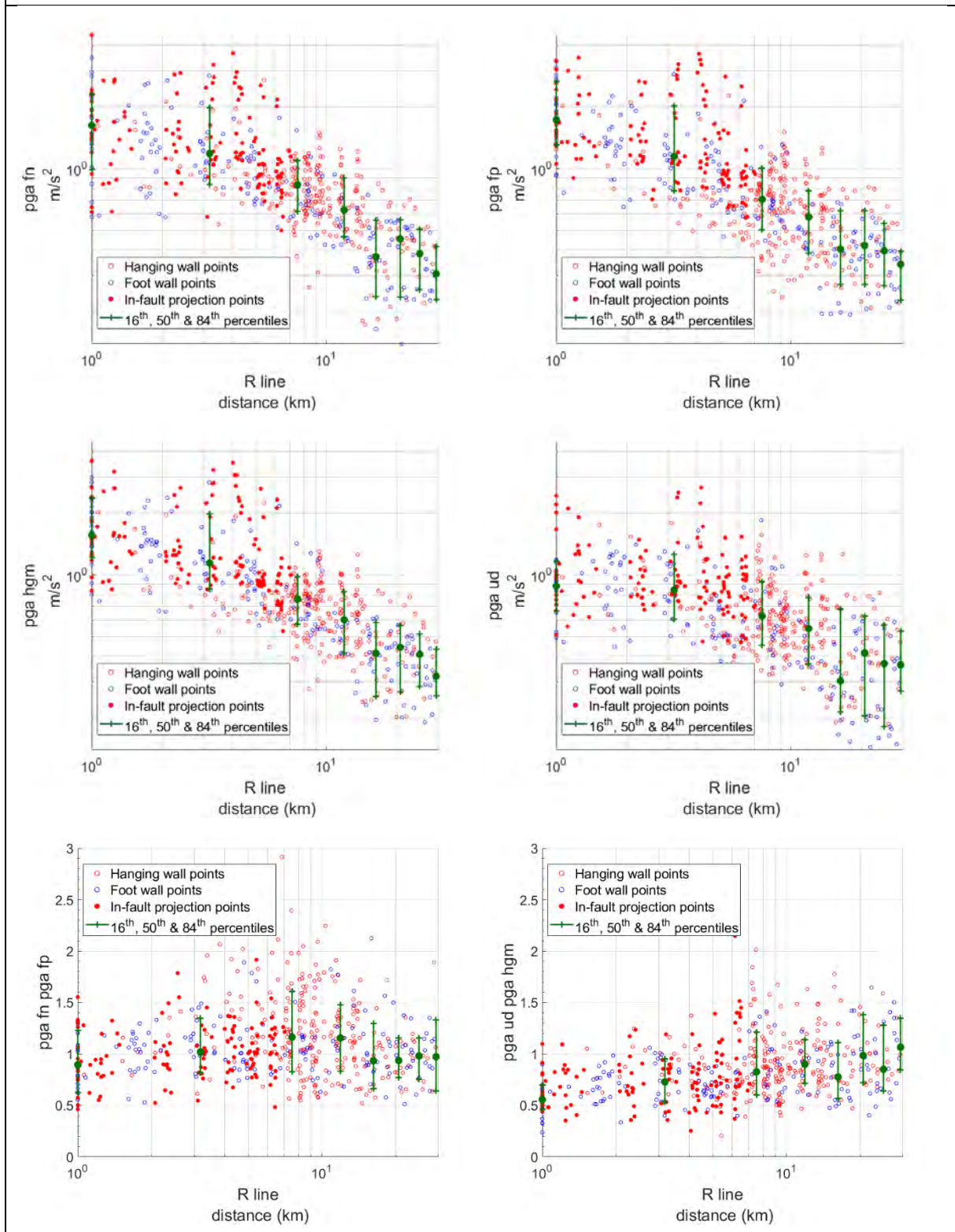
ITA_2009.04.06_03.32lt_Mw6.2

MAPS: PGA



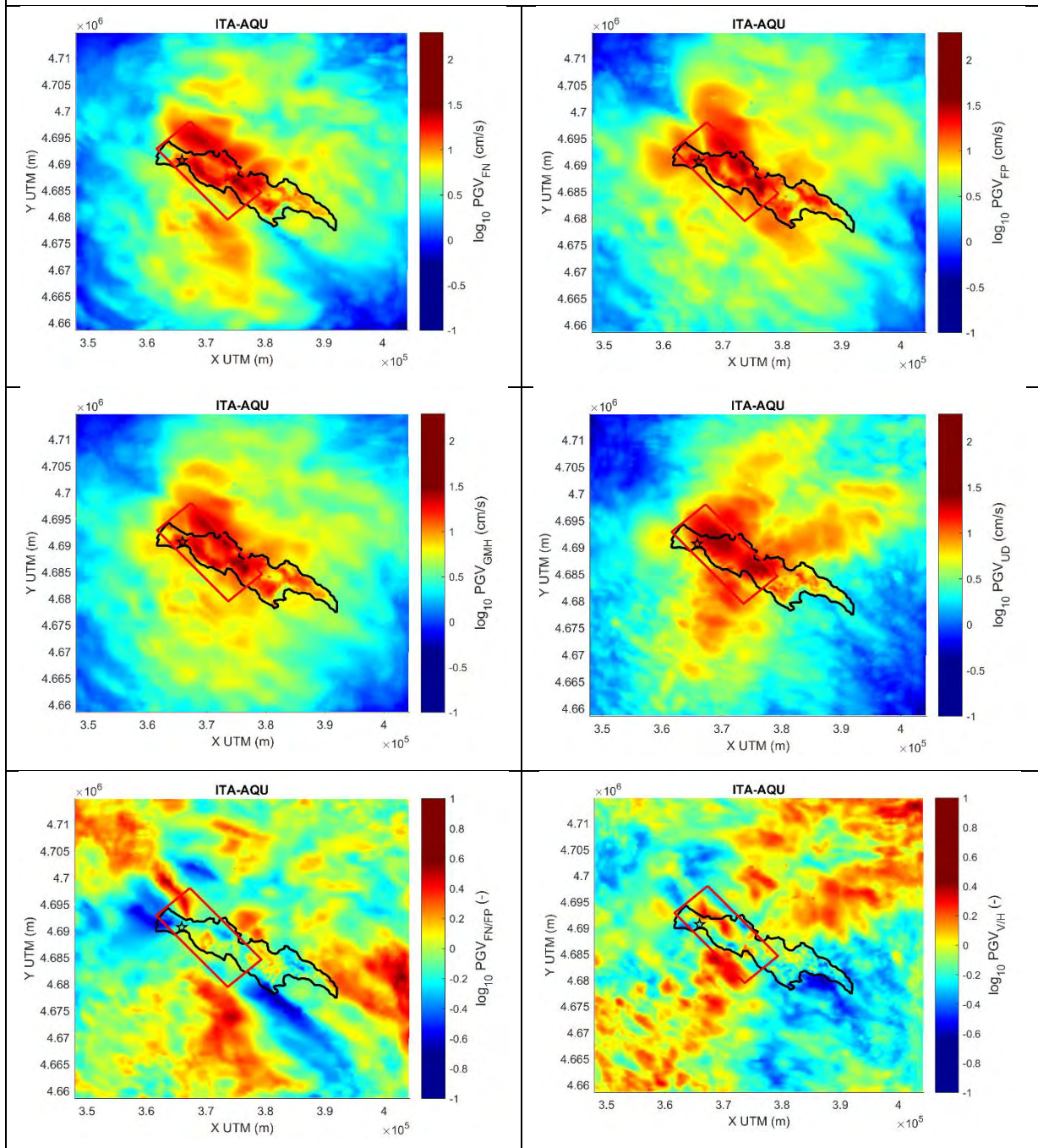
ITA_2009.04.06_03.32It_Mw6.2

Attenuation with distance: PGA



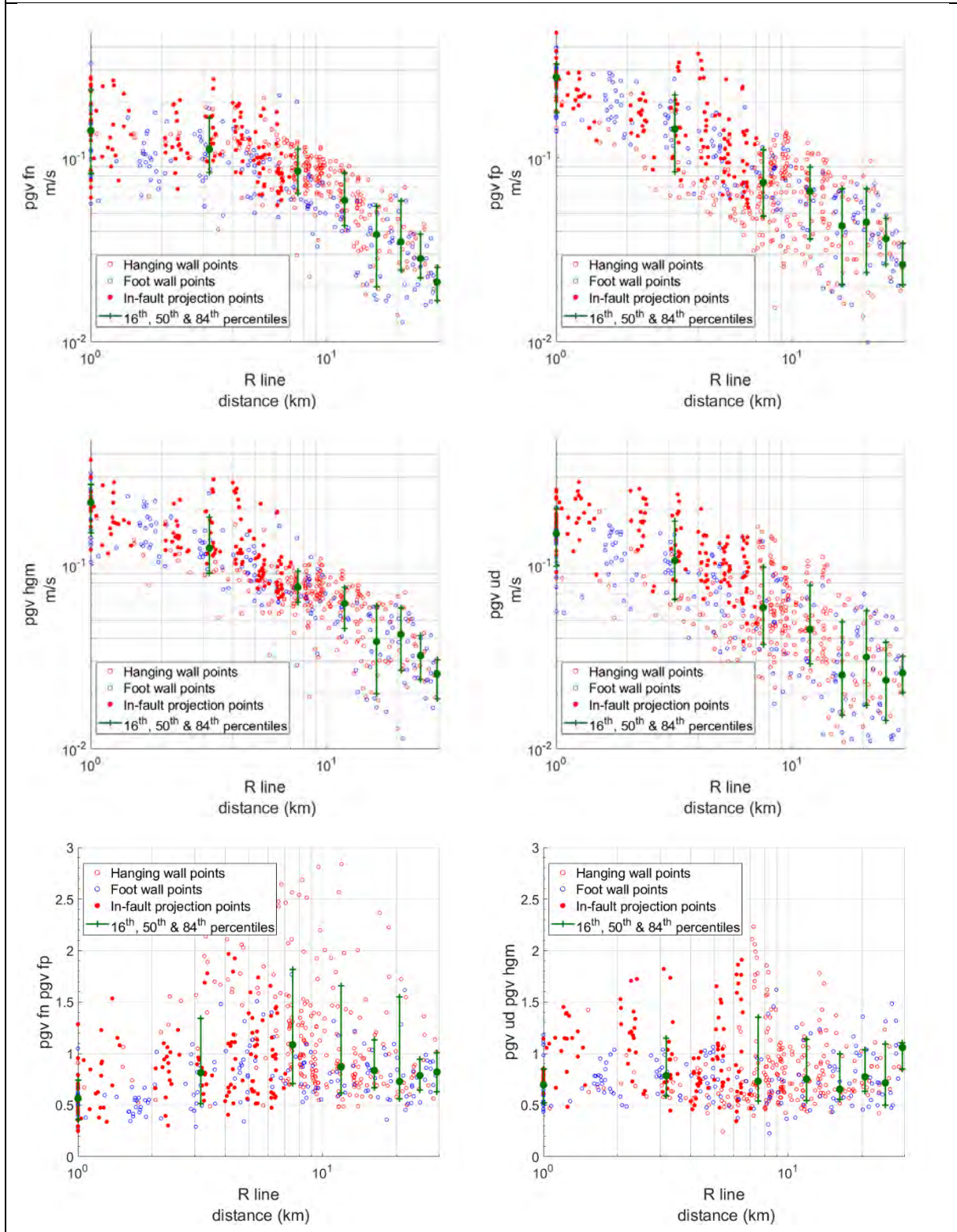
ITA_2009.04.06_03.32It_Mw6.2

MAPS: PGV



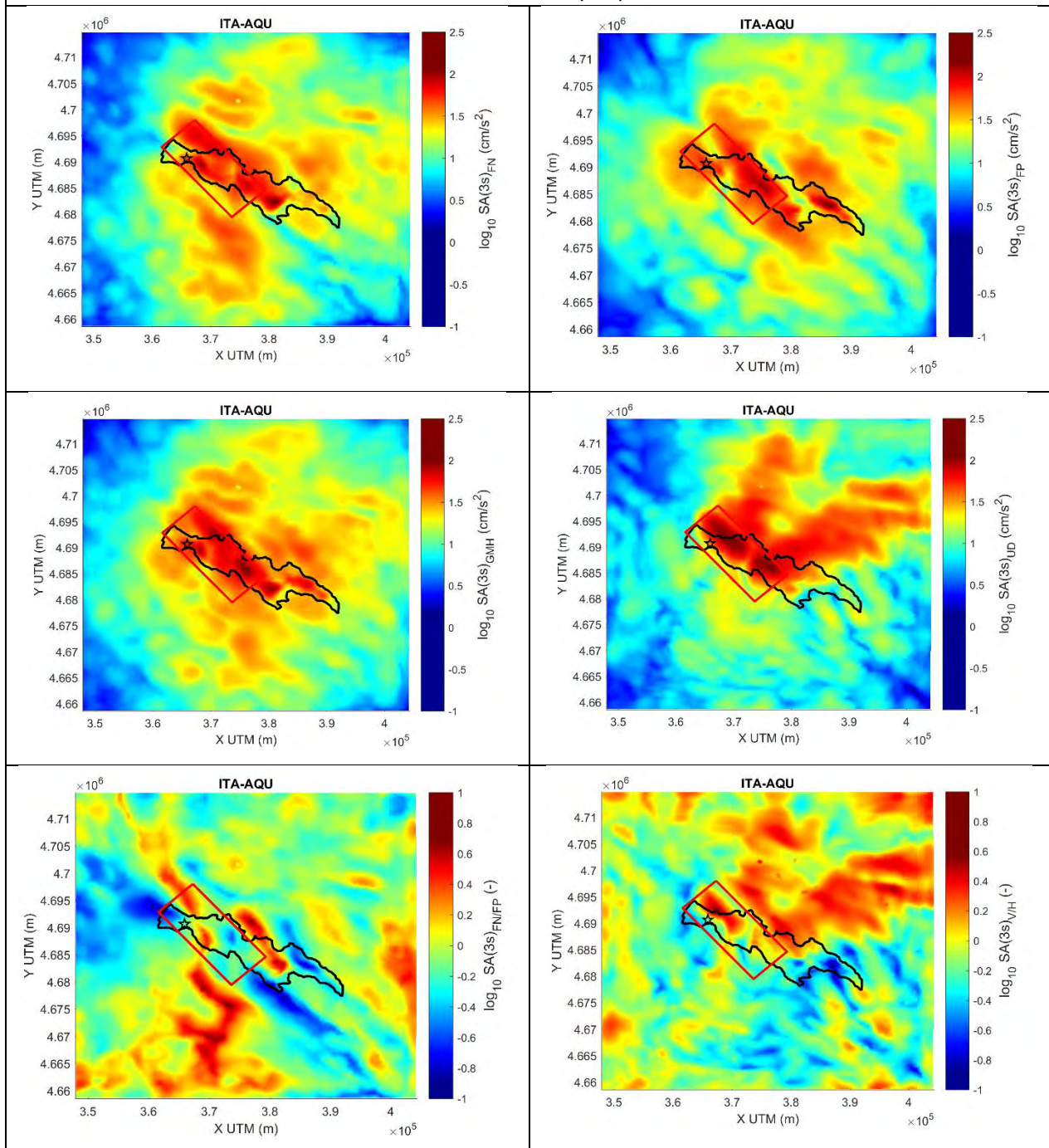
ITA_2009.04.06_03.32It_Mw6.2

Attenuation with distance: PGV



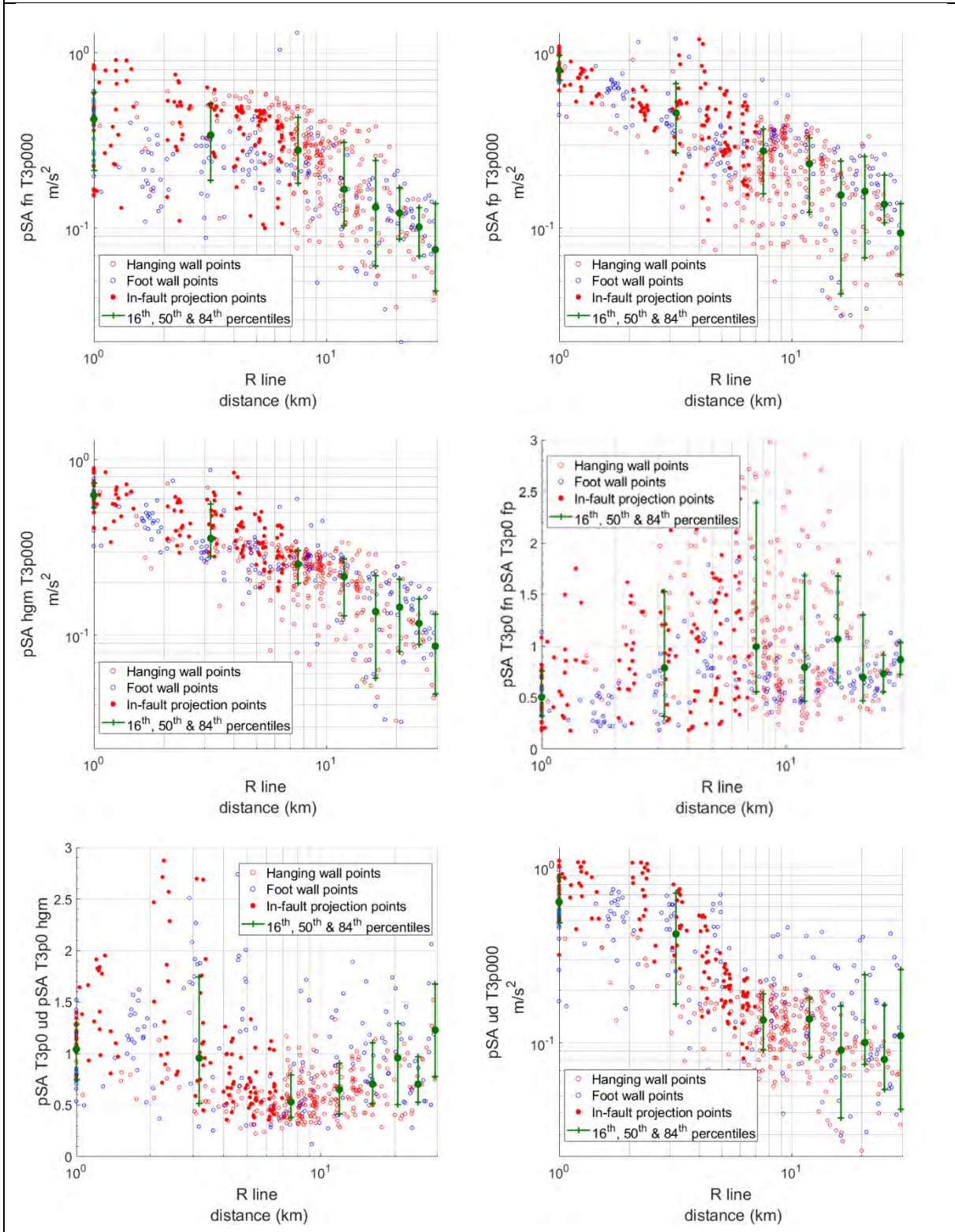
ITA_2009.04.06_03.32It_Mw6.2

MAPS: SA(3s)

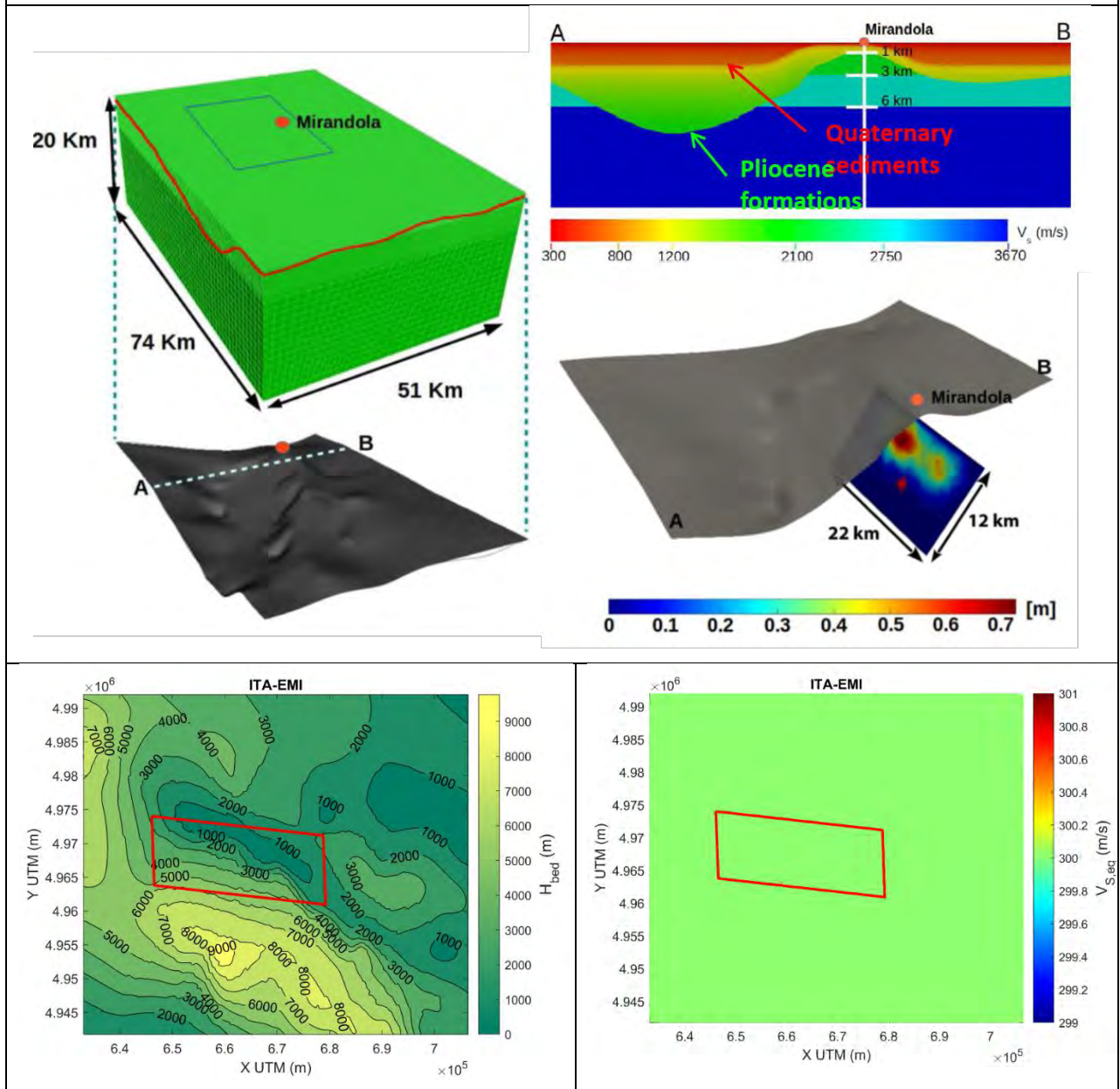


ITA_2009.04.06_03.32It_Mw6.2

Attenuation with distance: SA(3s)

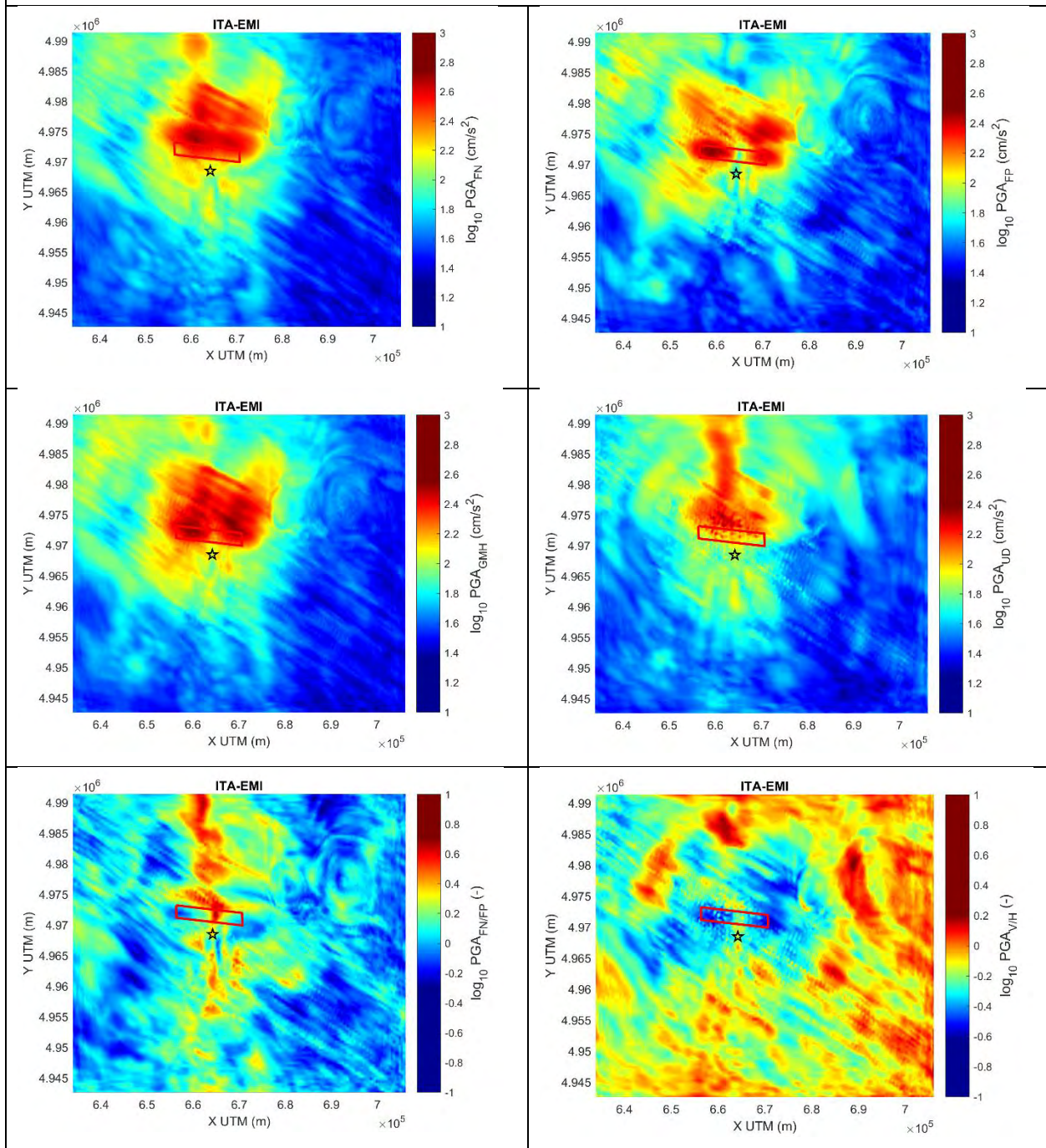


ITA_2012.05.29_09.00lt_Mw6.0



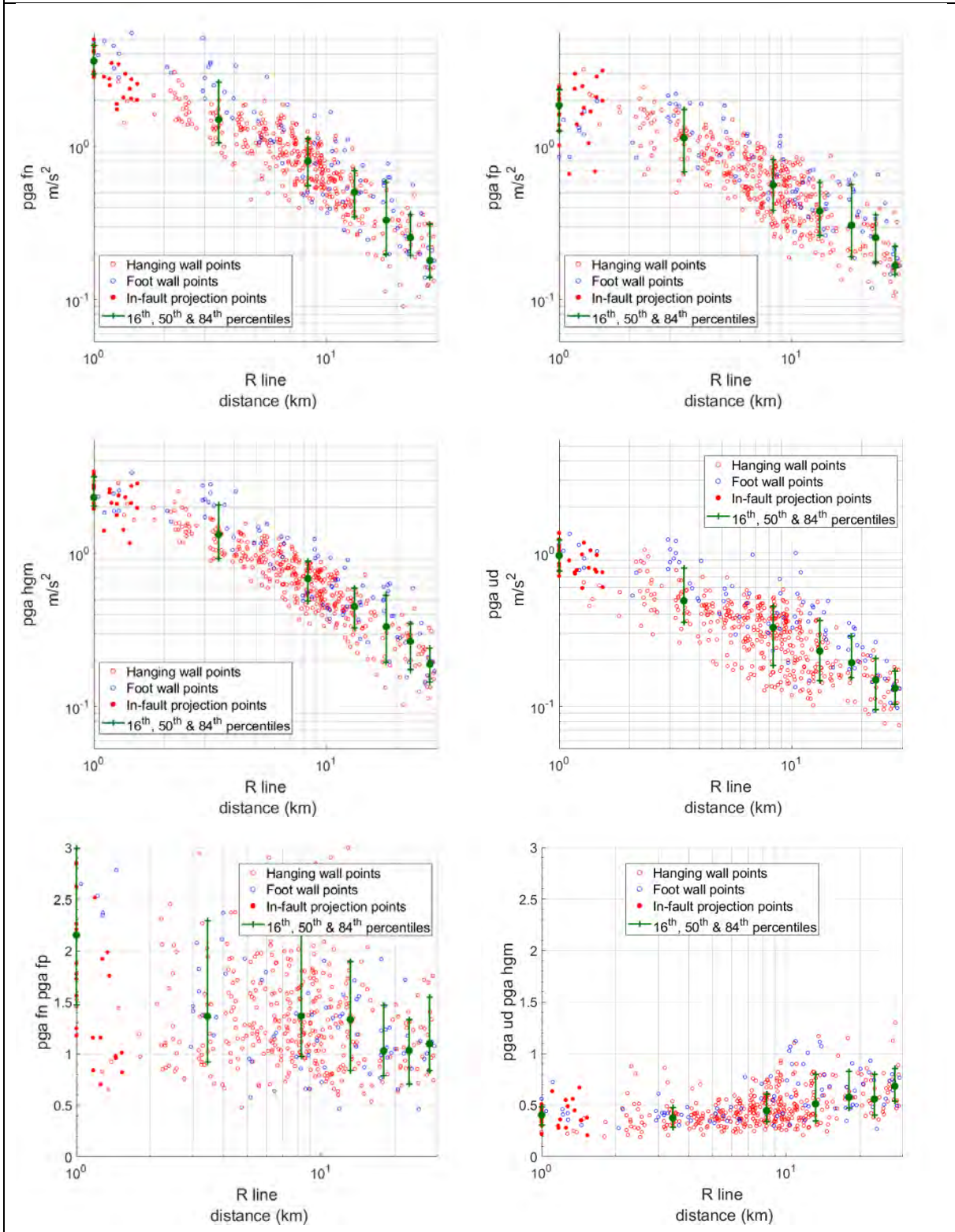
ITA_2012.05.29_09.00lt_Mw6.0

MAPS: PGA



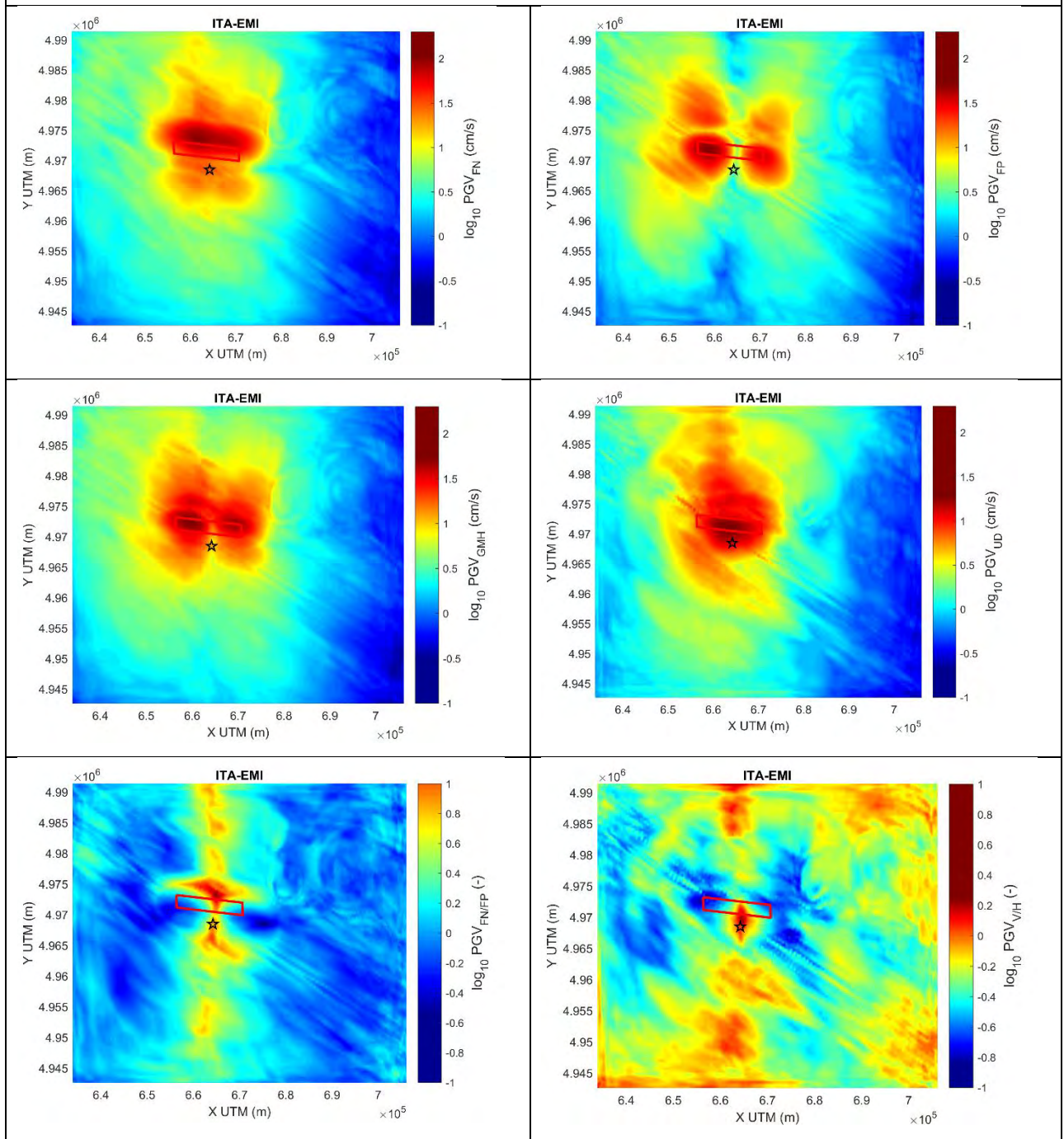
ITA_2012.05.29_09.00lt_Mw6.0

Attenuation with distance: PGA



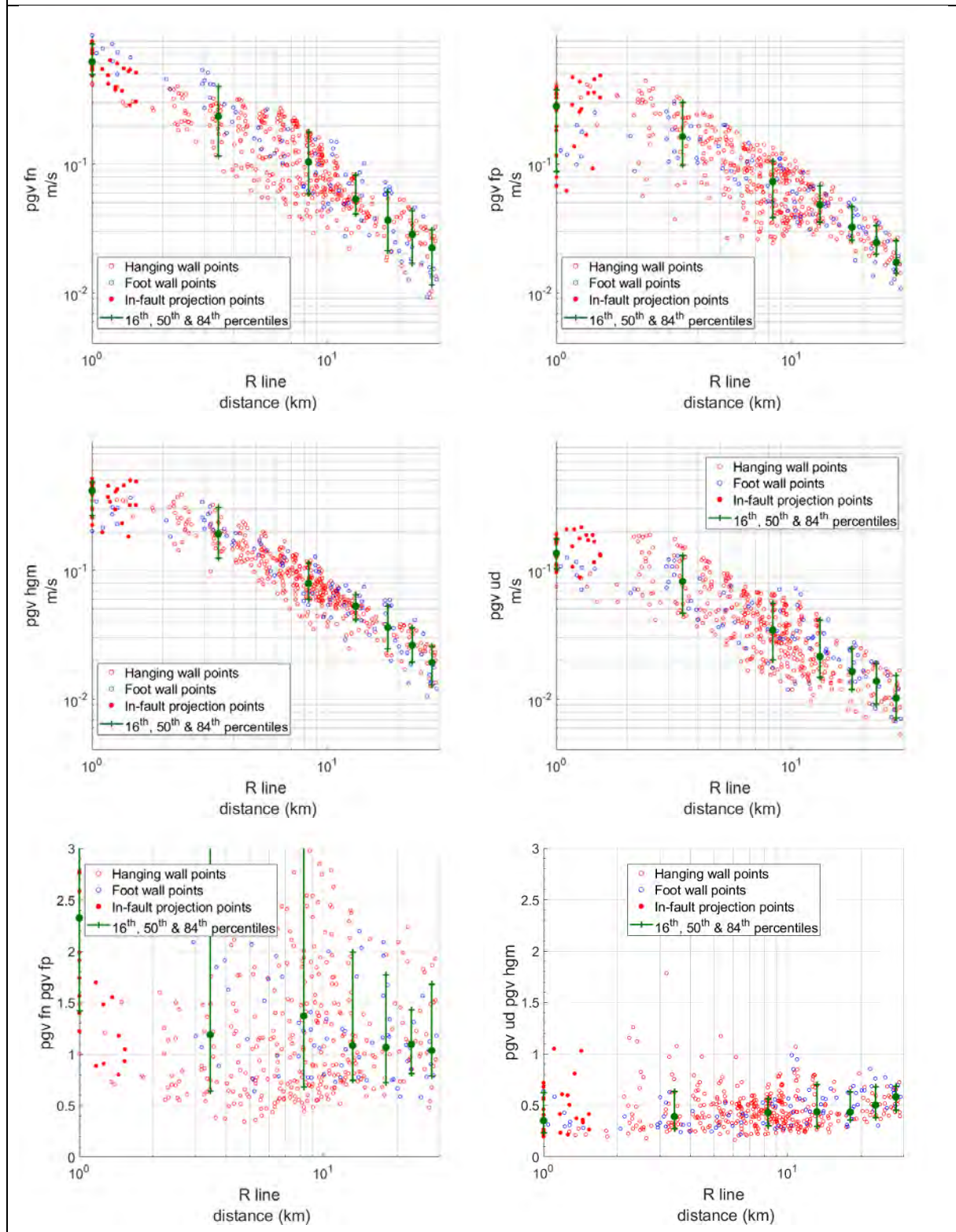
ITA_2012.05.29_09.00lt_Mw6.0

MAPS: PGV



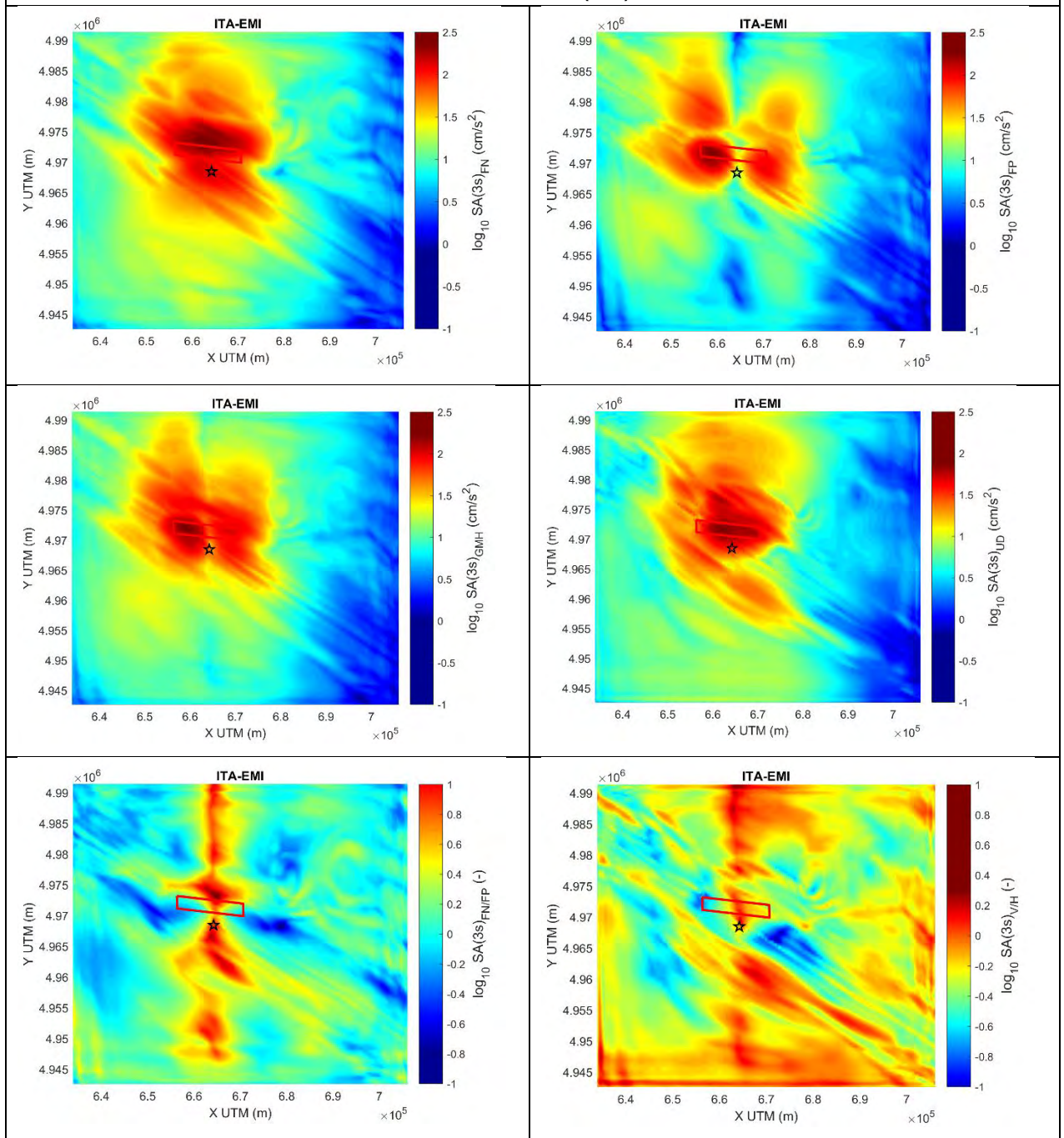
ITA_2012.05.29_09.00lt_Mw6.0

Attenuation with distance: PGV



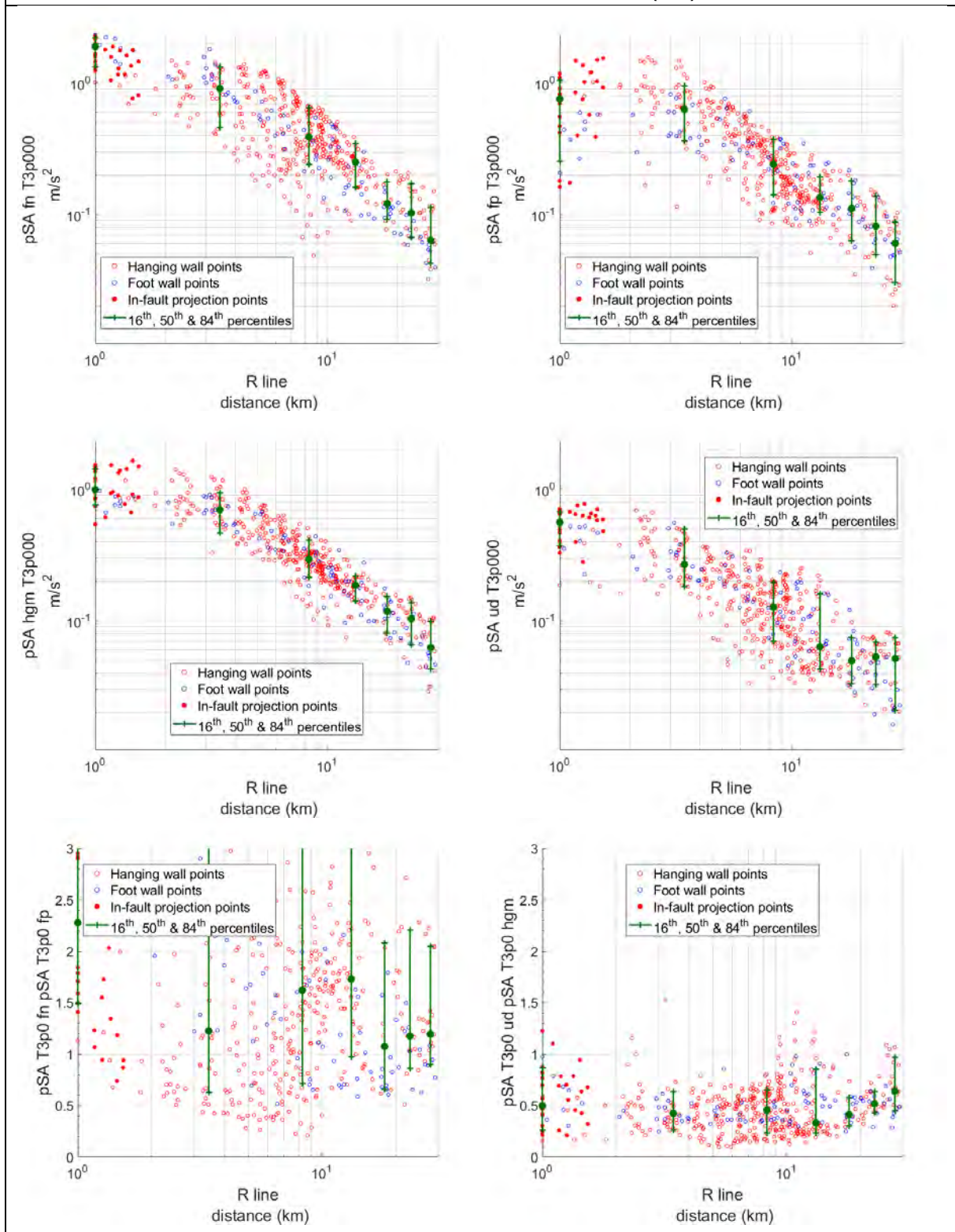
ITA_2012.05.29_09.00lt_Mw6.0

MAPS: SA(3s)

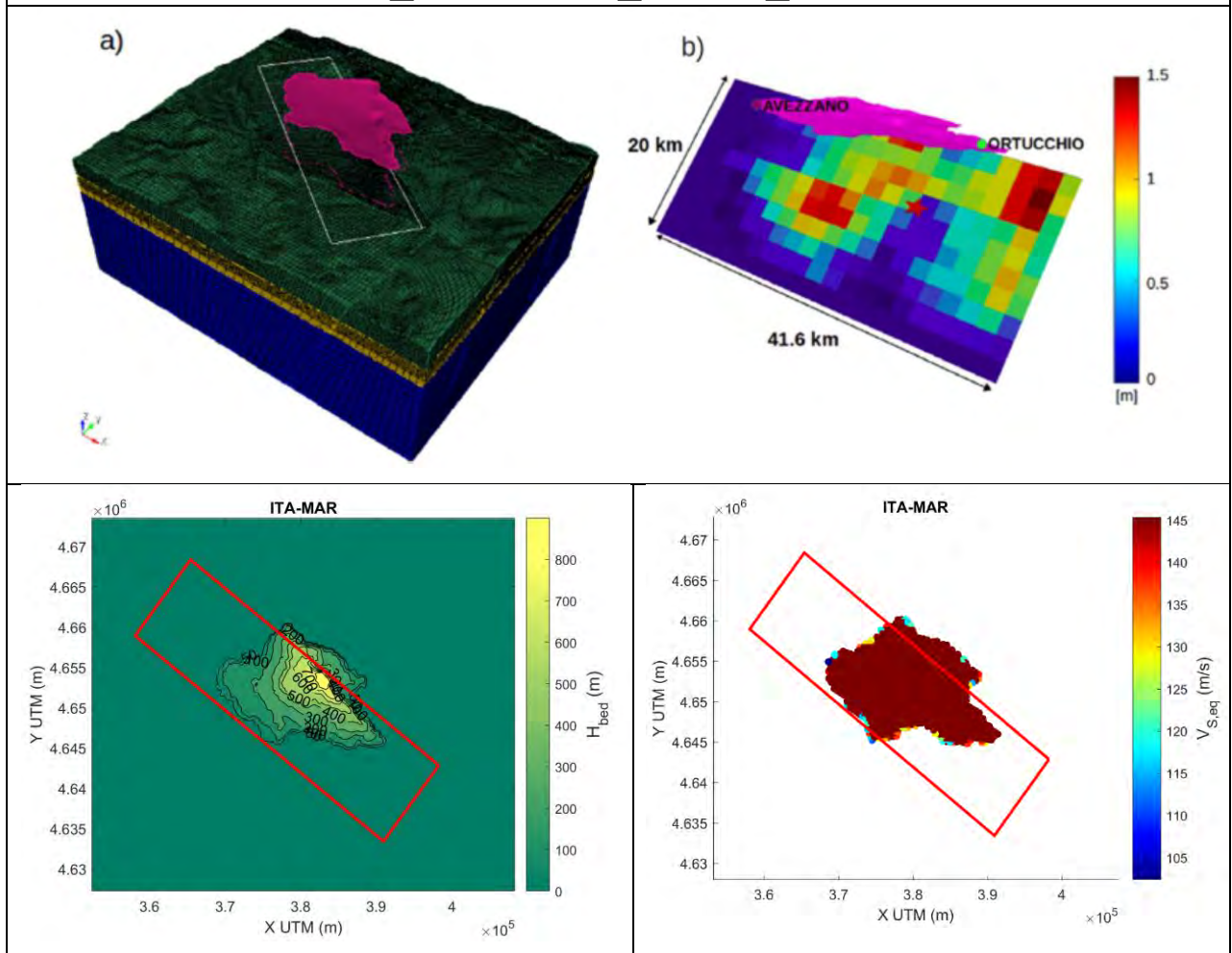


ITA_2012.05.29_09.00lt_Mw6.0

Attenuation with distance: SA(3s)

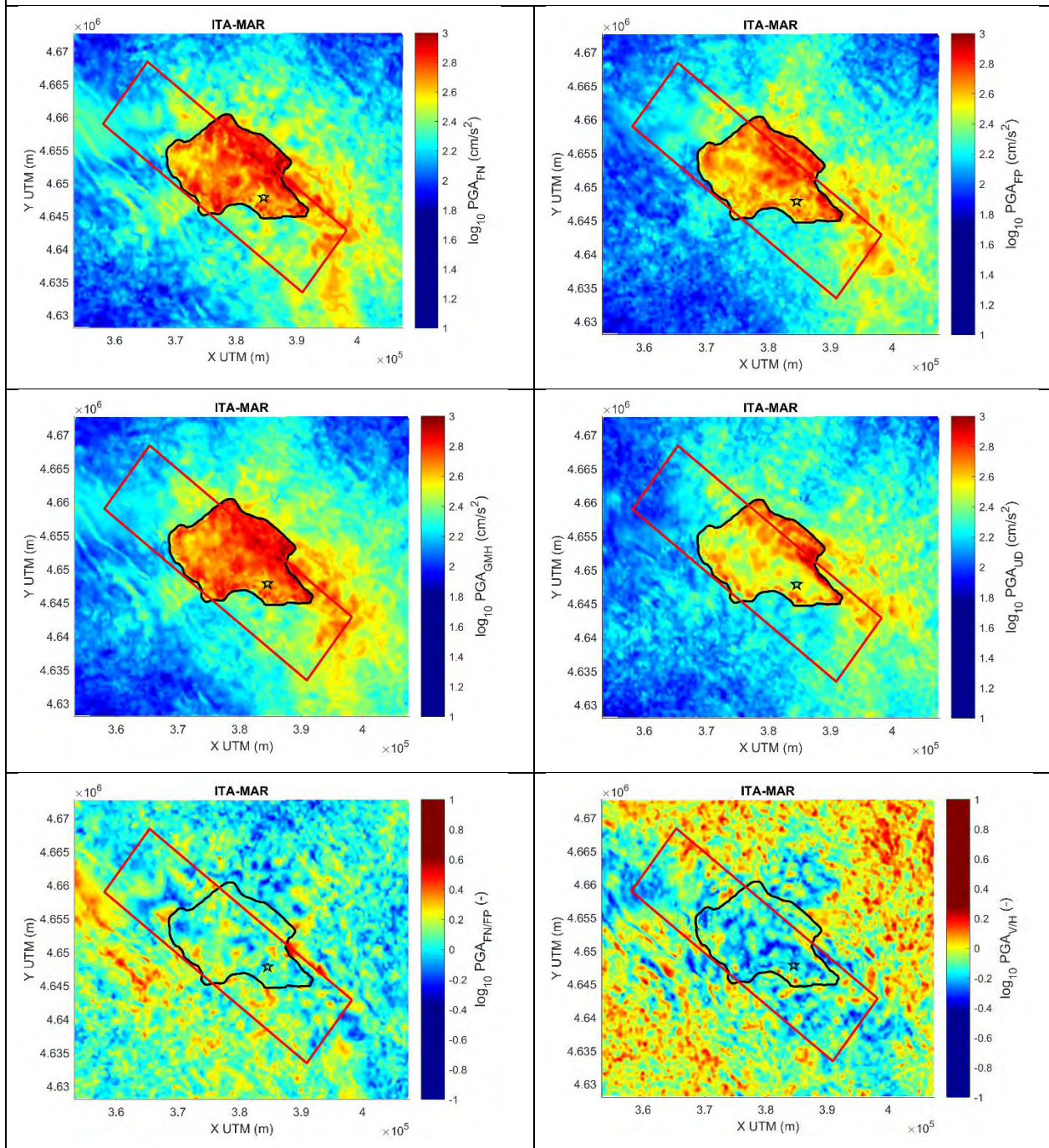


ITA_1915.01.13_06.52It_Mw6.7



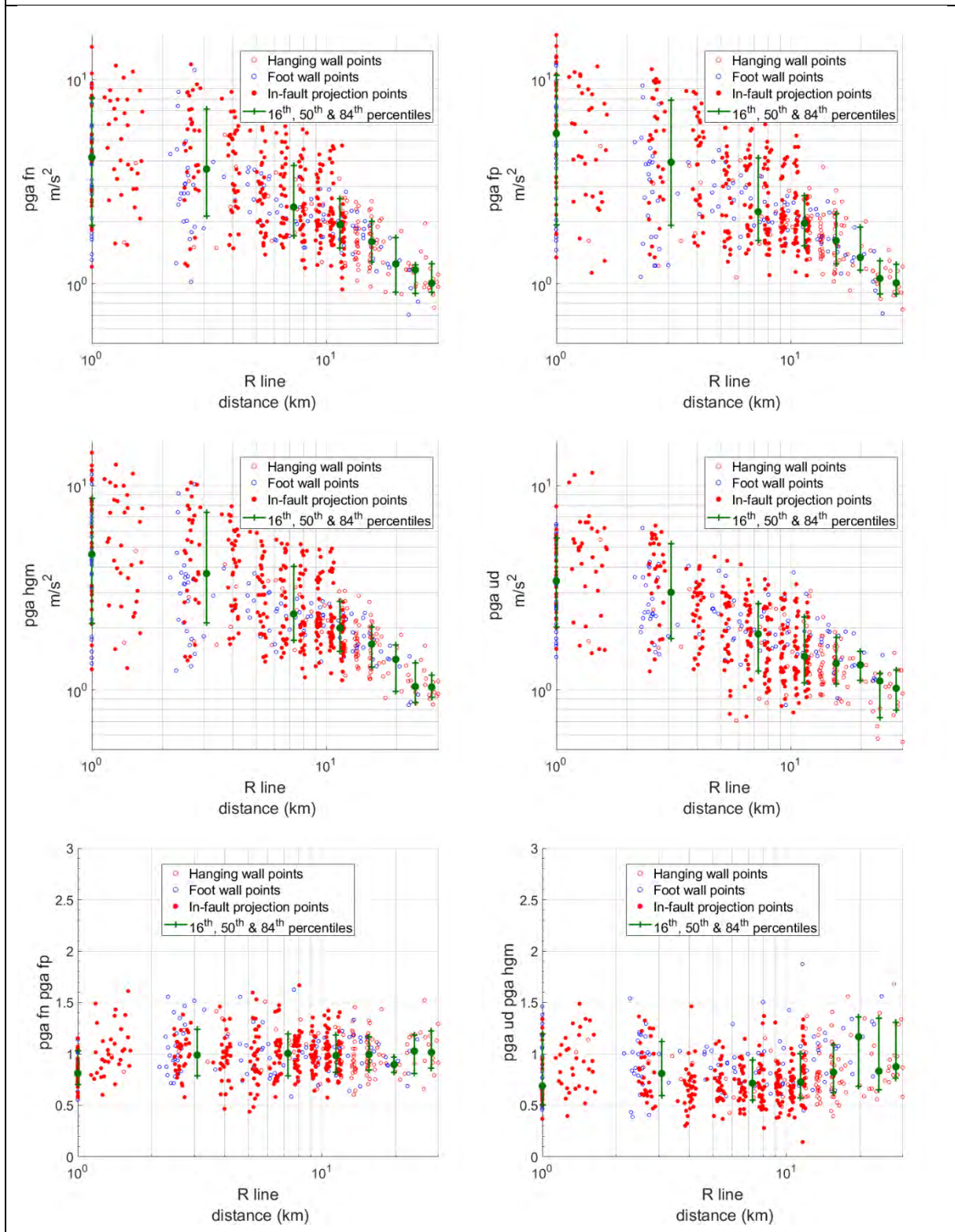
ITA_1915.01.13_06.52It_Mw6.7

MAPS: PGA



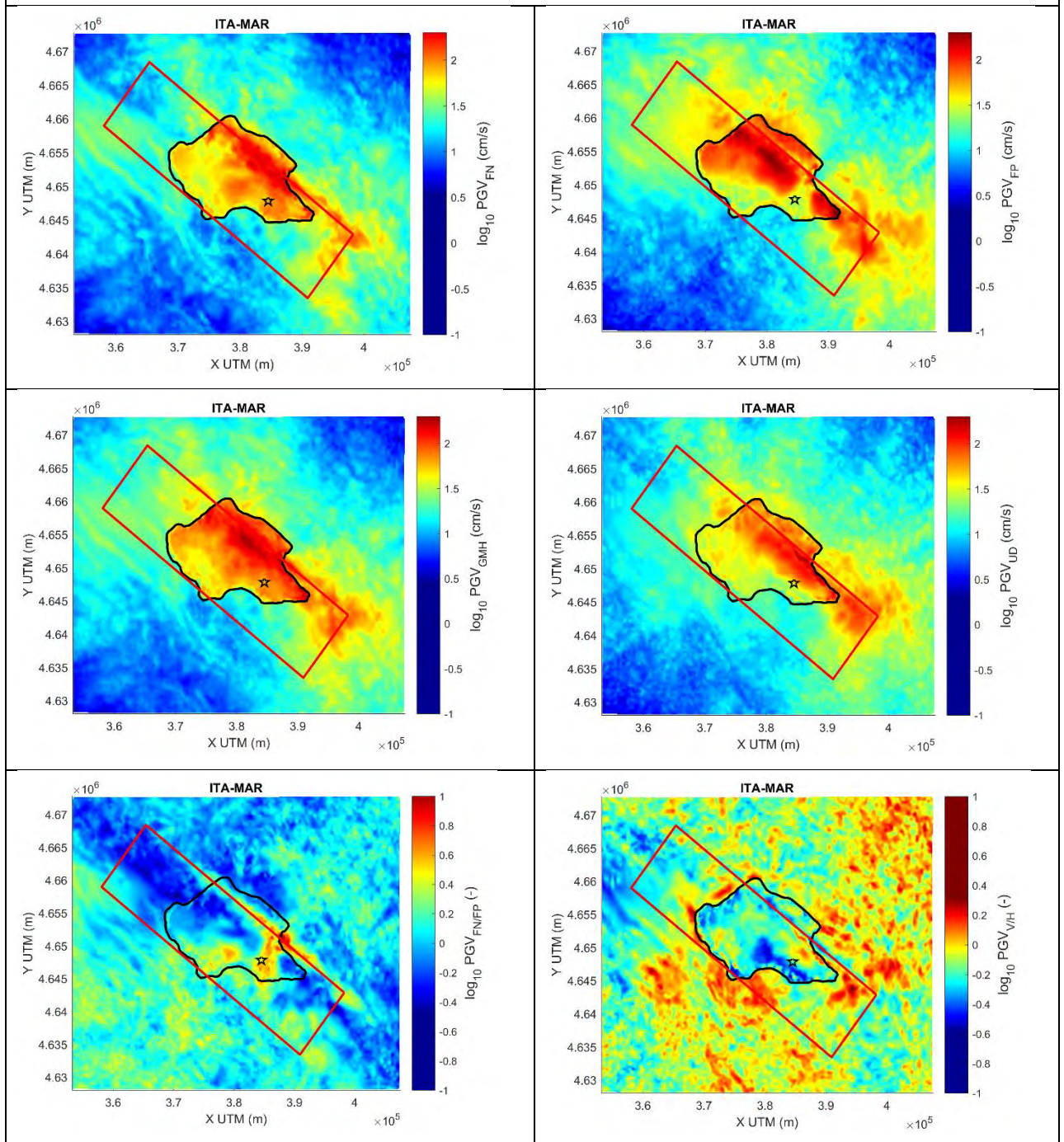
ITA_1915.01.13_06.52It_Mw6.7

Attenuation with distance: PGA



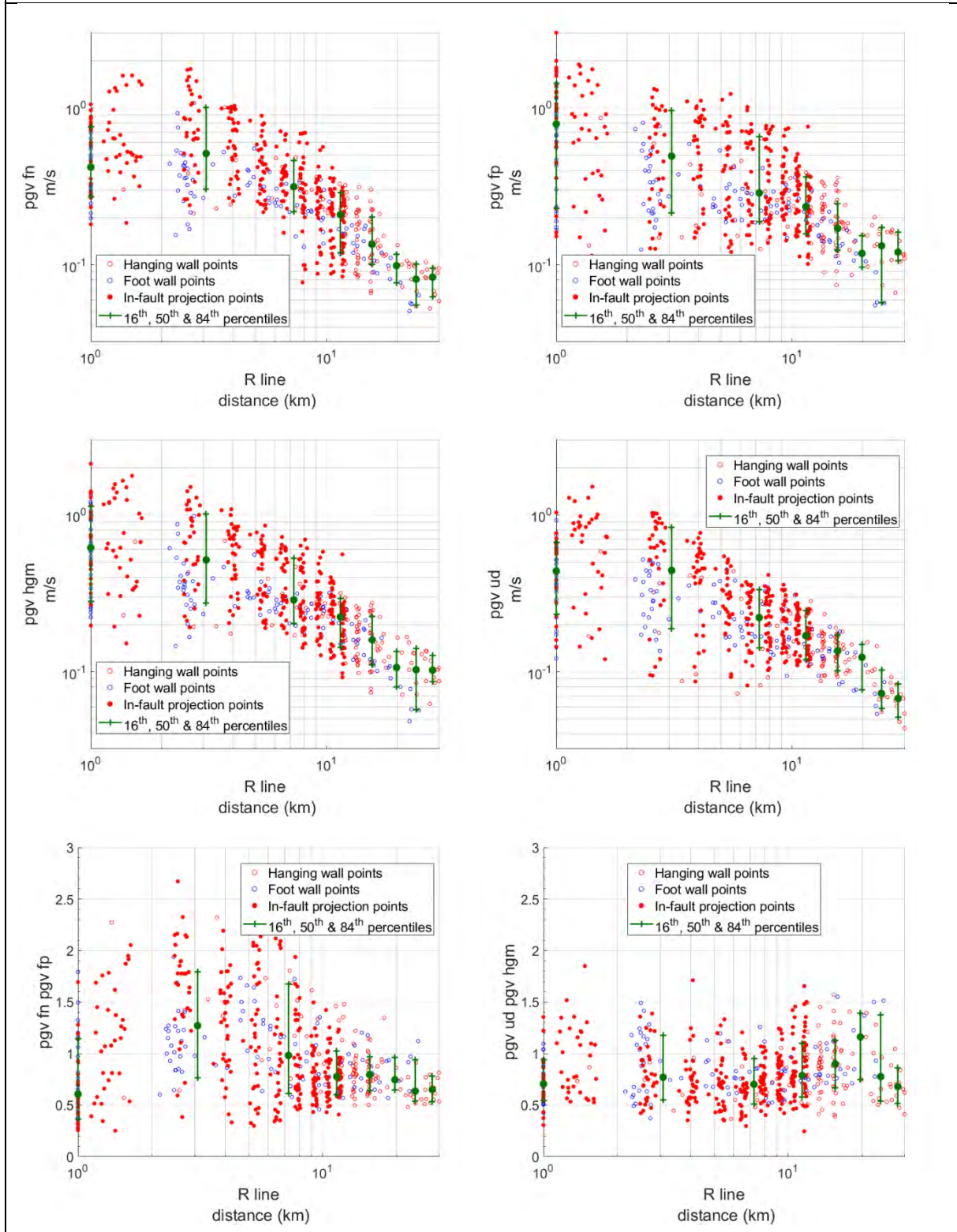
ITA_1915.01.13_06.52It_Mw6.7

MAPS: PGV



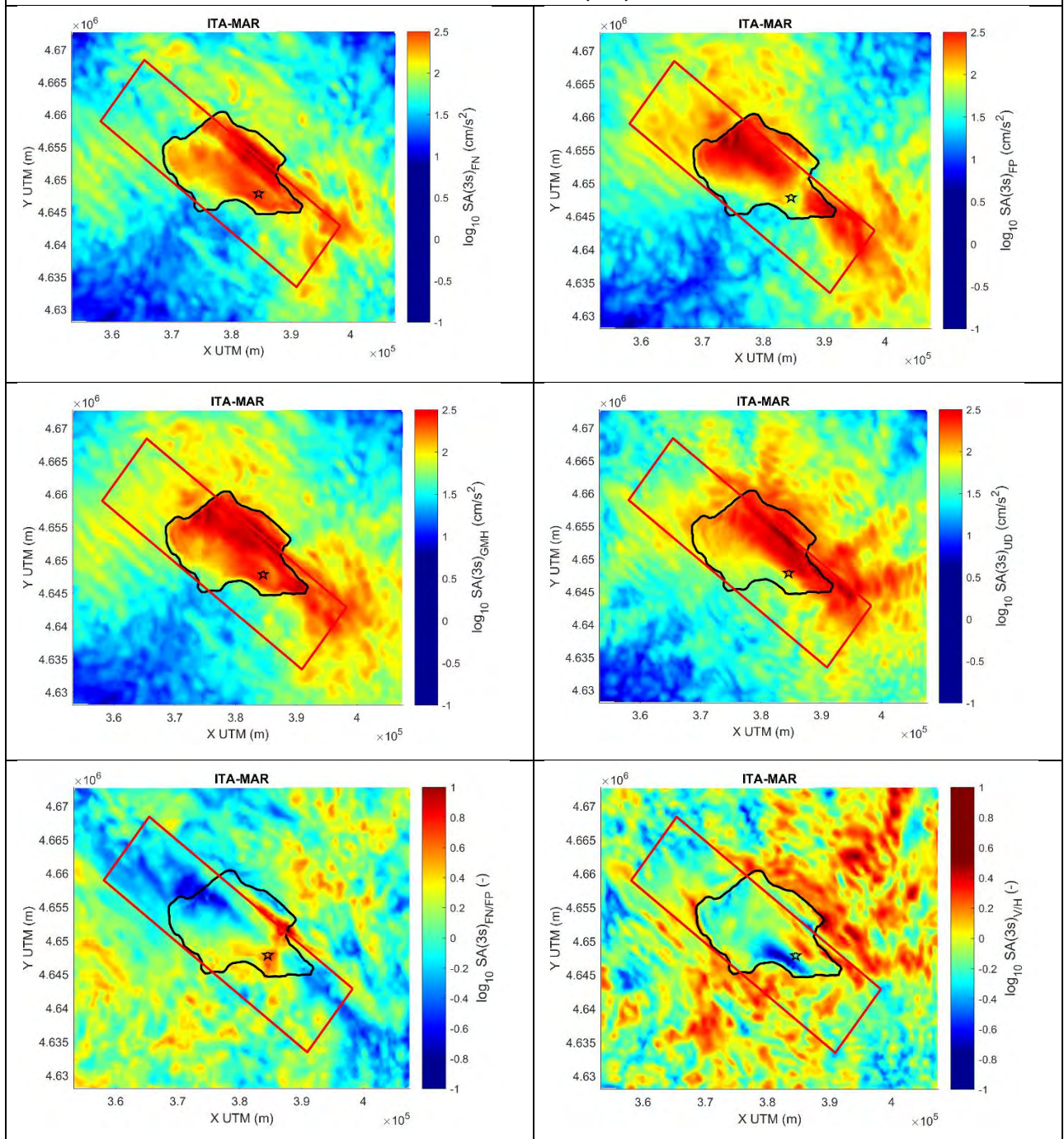
ITA_1915.01.13_06.52It_Mw6.7

Attenuation with distance: PGV



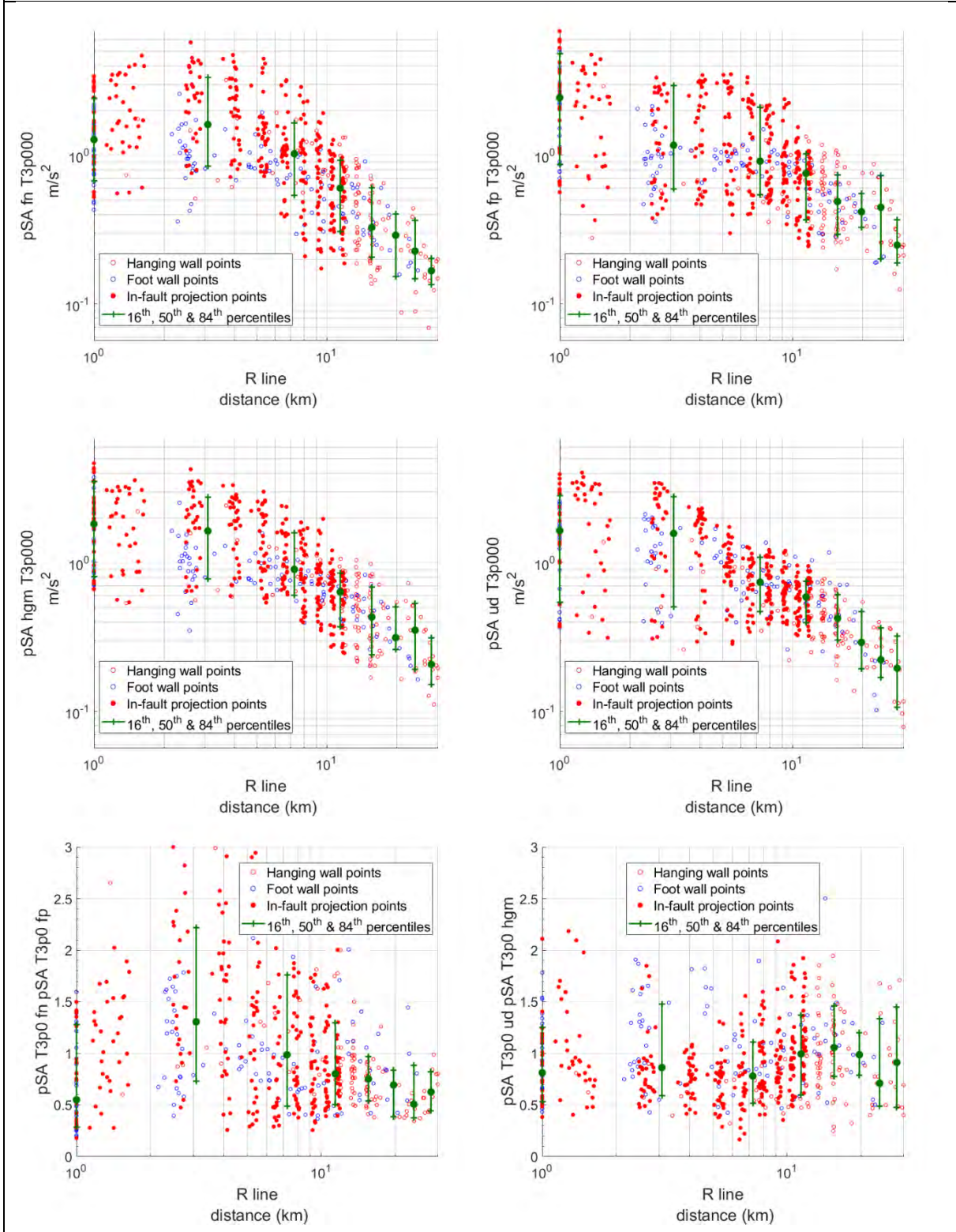
ITA_1915.01.13_06.52It_Mw6.7

MAPS: SA(3s)

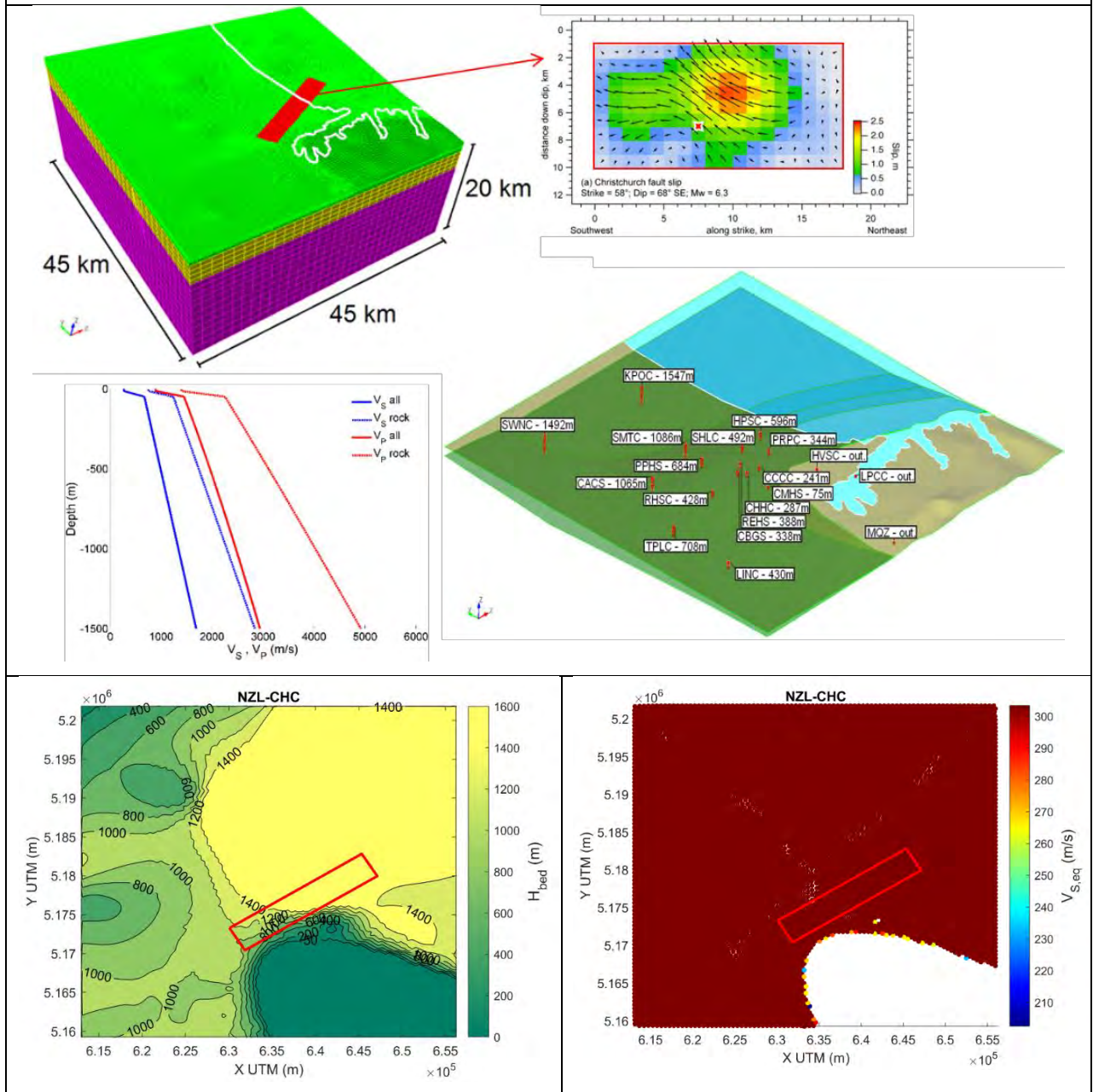


ITA_1915.01.13_06.52It_Mw6.7

Attenuation with distance: SA(3s)

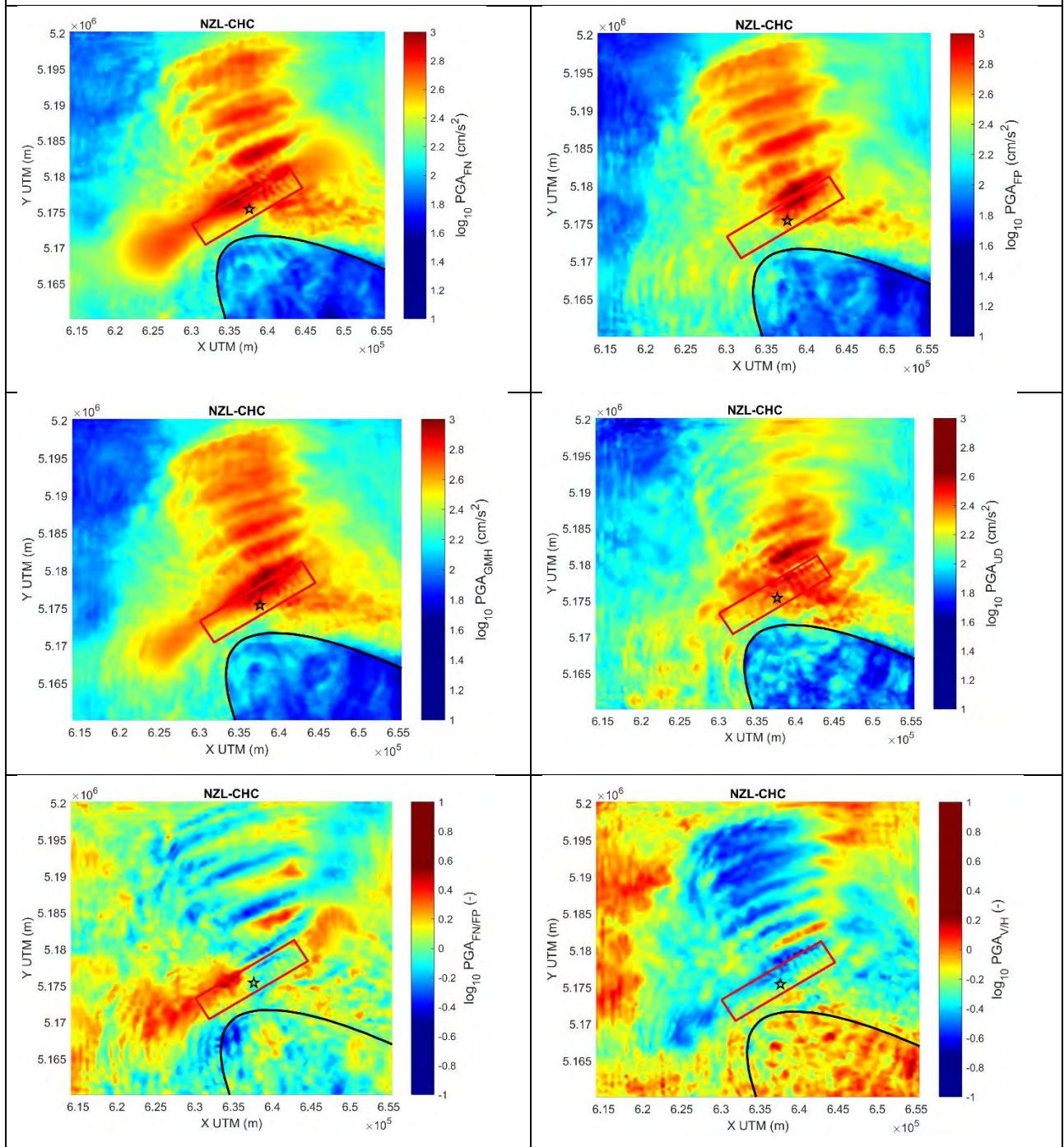


NZL_2011.02.22_12.51It_Mw6.3



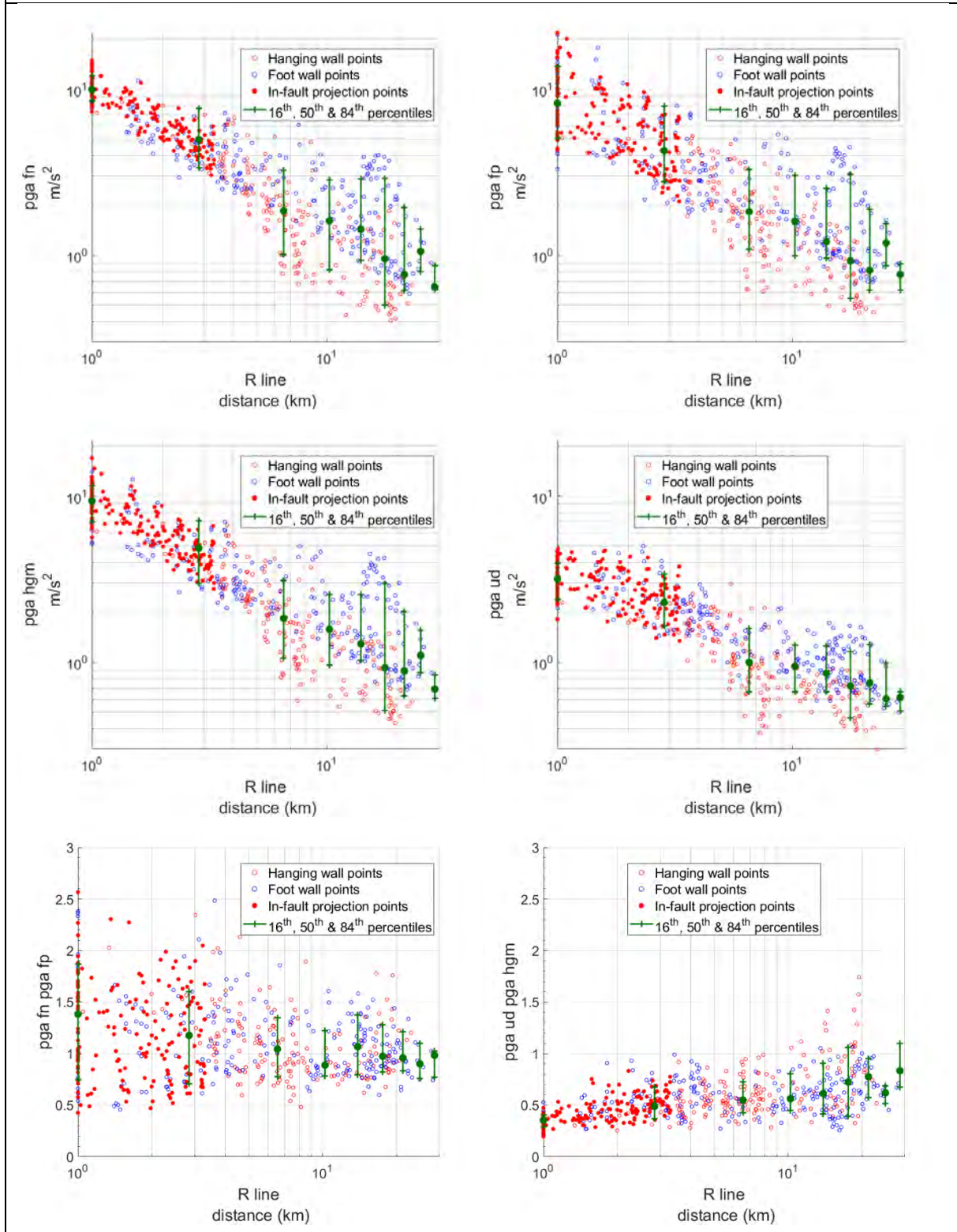
NZL_2011.02.22_12.51It_Mw6.3

MAPS: PGA



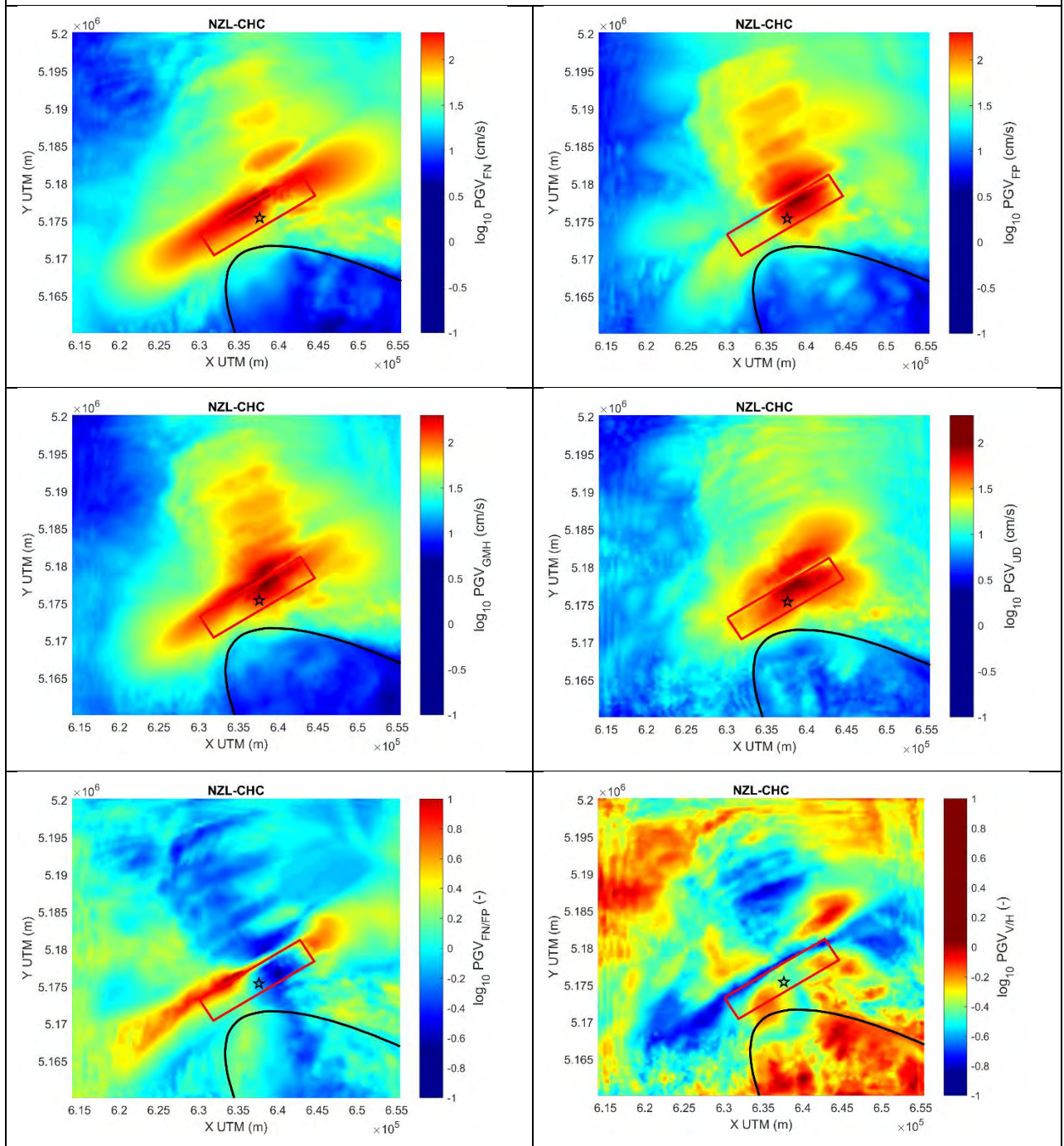
NZL_2011.02.22_12.51lt_Mw6.3

Attenuation with distance: PGA



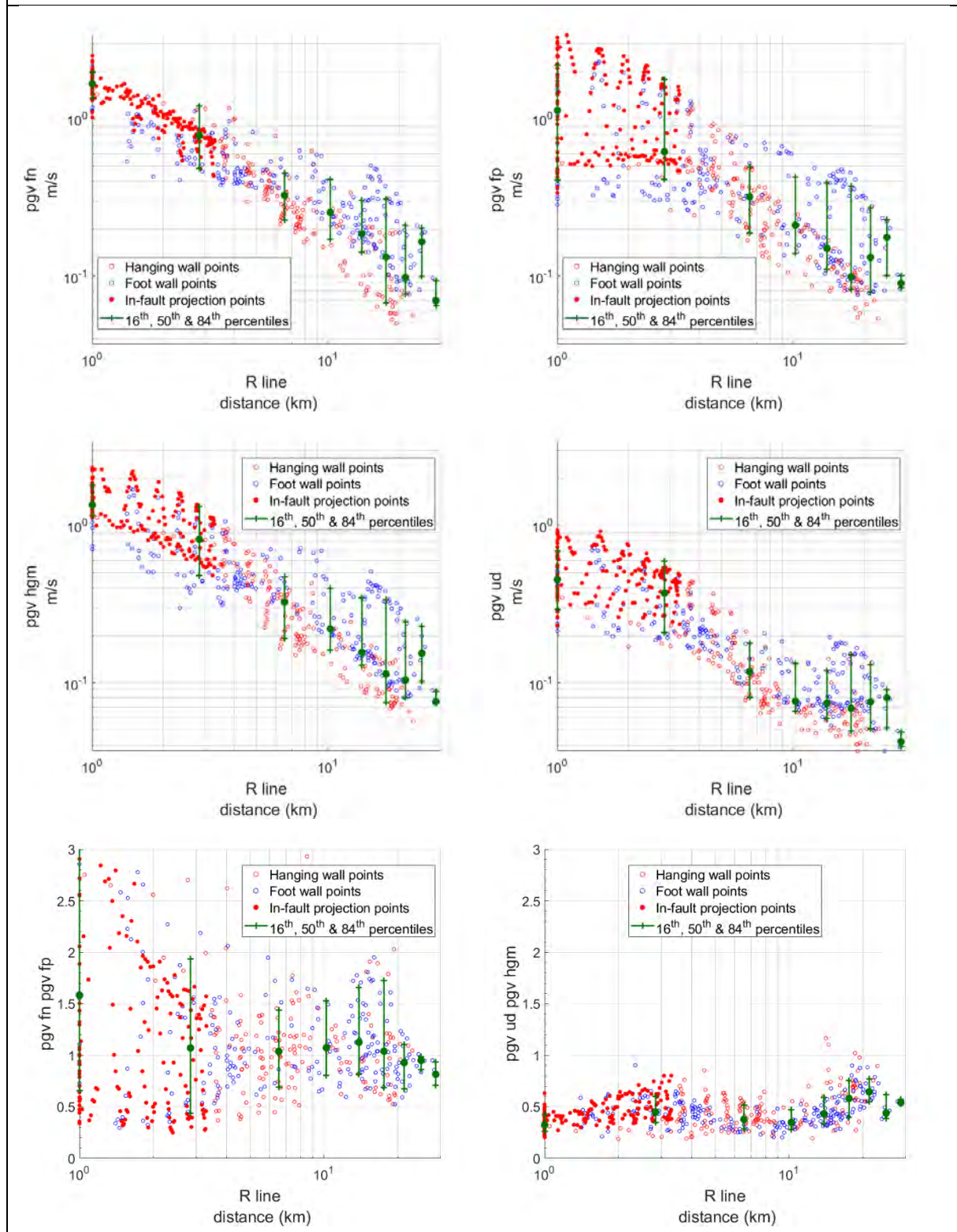
NZL_2011.02.22_12.51lt_Mw6.3

MAPS: PGV



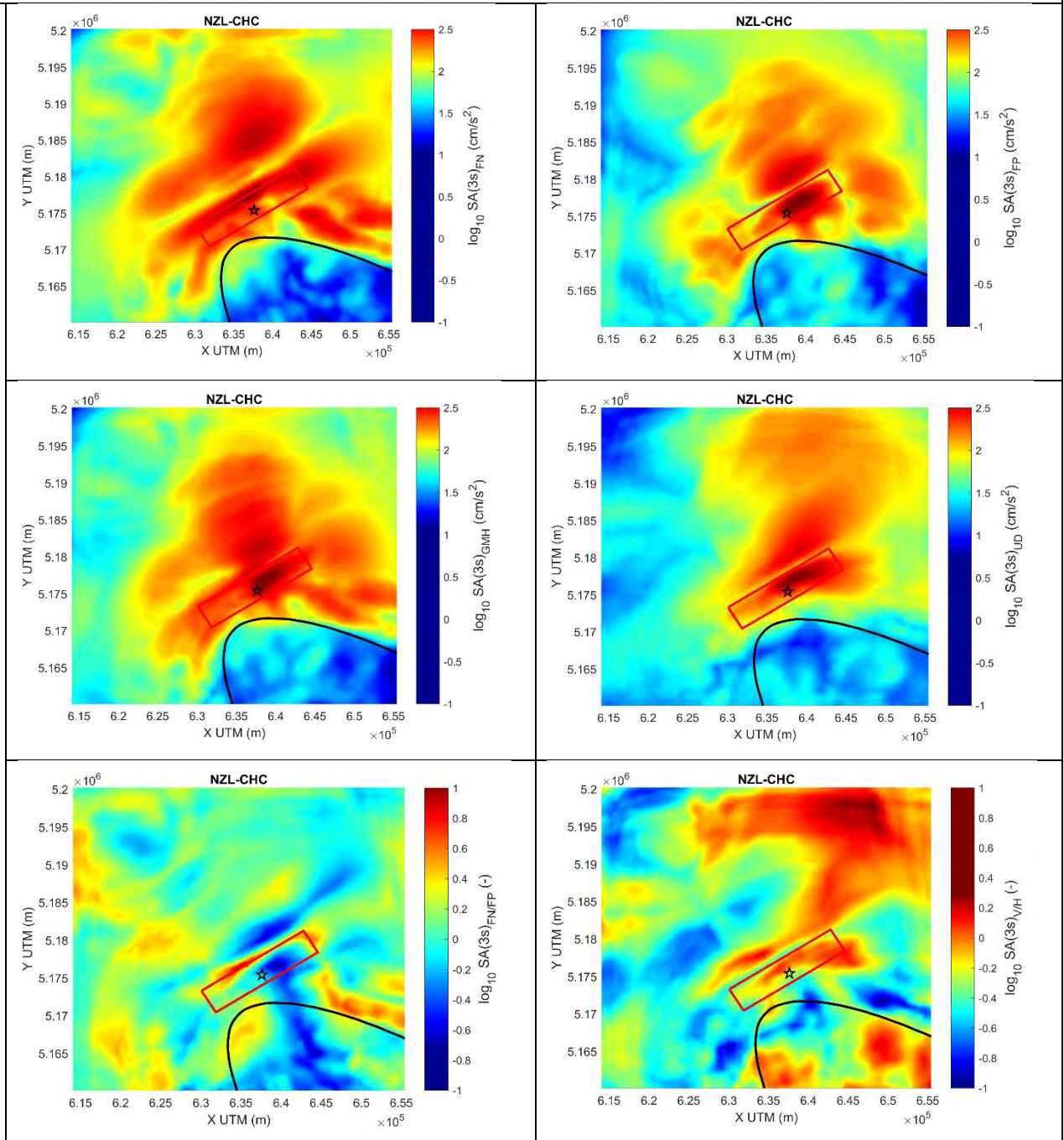
NZL_2011.02.22_12.51lt_Mw6.3

Attenuation with distance: PGV



NZL_2011.02.22_12.51t_Mw6.3

MAPS: SA(3s)



NZL_2011.02.22_12.51lt_Mw6.3

Attenuation with distance: SA(3s)

